Deciphering Petrogenetic Histories of Polymict Regolith Breccias from the Moon, Mars, and 4 Vesta

by

Radhika Saini

A thesis submitted in partial fulfillment of the requirements for the degree of

Master of Science

Department of Earth and Atmospheric Sciences
University of Alberta

Abstract

The geological histories of planetary bodies in our solar system can be understood by unraveling the petrogenetic histories and evolution of regolith breccias derived from their planetary surfaces. This study investigates three meteoritic breccias, Northwest Africa (NWA) 14340, Sariçiçek, and NWA 10922, originating from the Moon, 4 Vesta, and Mars, respectively. The breccias' formation processes and evolutions are unraveled through comprehensive petrological analyses, coupled with literature synthesis. This study reveals distinct stages in the petrogenetic histories of the breccias, with impact cratering processes playing an important role at each stage:

Stage 1: Clast excavation and regolith mixing, showcasing the dominance of impact cratering and gardening processes across the Moon, 4 Vesta, and Mars.

Stage 2: Lithification processes, which varied among the breccias: NWA 14340 possibly underwent shock or temperature-induced processes; Sariçiçek was shock-lithified; and NWA 10922 underwent thermal annealing, recrystallizing its matrix around clasts. The location of each breccia's lithification relative to the locus of impact cratering emerged as a critical factor influencing lithification under different pressure or temperature regimes.

Stage 3: Post-lithification processes, NWA 14340 and Sariçiçek exhibit no evidence of post-lithification modification, such as thermal metamorphism or hydrothermal activity. In contrast, NWA 10922 shows evidence of secondary mineral formation due to hydrothermal activity (Lorand et al. 2015), suggesting a dynamic geological history with near-surface water involvement.

Stage 4: Excavation processes reflect the varying escape velocities and regolith turnover rates of the respective planetary bodies. NWA 14340 experienced shock pressures near the Moon's

surface high enough to melt the matrix and quench to glass with a high-pressure mineral assemblage of tissintite, coesite ± garnet. In contrast, low shock pressures were sufficient for the excavation of lithified Sariçiçek and NWA 10922 from 4 Vesta and Mars, respectively.

Implications of this study offer insights into the geological evolution of the Moon, 4 Vesta, and Mars. The variations in lithification processes, from shock-induced compaction to thermal annealing, highlight the diverse processes operating on these planetary bodies. These findings contribute to our broader understanding of planetary geology and provide valuable constraints for future studies aiming to unravel the complex histories of rocky planetary bodies in our solar system.

Acknowledgments

I have many people to thank for their support in preparing this thesis. Firstly, I want to thank my MSc supervisor, Dr. Chris Herd, for giving me the opportunity to work on meteorite samples. Chris provided invaluable guidance, support, and advice throughout my academic and professional journey, helping me figure out my path and goals as a graduate student. He also offered numerous opportunities for networking and attending conferences, for which I am very grateful. I also want to express my heartfelt thanks to my late co-supervisor, Dr. Erin Walton. I am grateful for Erin taking me on as her student and providing indispensable support and guidance towards this project. She is dearly missed by me and many others. It was an honor to work with both Chris and Erin, and I am thankful for the opportunity to be mentored by them.

I am thankful to Matthew Steele-MacInnis for being on my supervisory committee and providing feedback on the progress of this project. A big thank you to Sophie Benaroya, firstly for being my office mate and always providing much-needed company, and more importantly, for answering my endless mineralogy-related questions.

This research depended on acquiring high-quality data using various instruments at the University of Alberta and MacEwan University. I would specifically like to thank Andrew Locock for help with EPMA analysis, Edison Dong for Raman spectroscopy, Nathan Gerein for FESEM, Mark Labbe for preparing the NWA 10922 tile, and Igor Jakab for assisting with the acquisition of reflected light image of NWA 10922. I would also like to acknowledge Carl Agee and the University of New Mexico Meteorite Collection for providing the sample NWA 10922.

I owe endless gratitude to my family, especially my Mom and Dad, for providing love, support, and comfort. I love you both. Most importantly, thank you to my partner, Alan, for your

endless support, love, and friendship. It only takes one person to believe in you, and I am incredibly grateful for your belief in me.

Table of Contents

List of Tables

List of Figures

List of Abbreviations

BSE	Backscattered Electrons
EDS	Energy Dispersive X-Ray Spectrometry
EPMA	Electron Probe Microanalyzer
FESEM	Field Emission Scanning Microscope
MIL	Miller Range
Mya	Million years ago
NWA	Northwest Africa
PDF	Planar deformation features
PPL	Plane-polarized light
TL	Transmitted light
XPL	Cross-polarized light

Chapter 1: Introduction

1.1 Introduction

Regolith is the unconsolidated, typically heterogeneous, and fragmental, uppermost surface layer of a planet, satellite, or asteroid (Spray 2016). Planetary regolith hosts chemical and physical characteristics of processes that occurred on the surface of planetary bodies. Unlike Earth's regolith, planetary regolith from bodies with minimal to no tectonic activity preserves a record of billions of years of the history of its parent body and the inner solar system (Langevin and Arnold 1977). The regolith can evolve on planetary surfaces to become a part of the regolith breccia, a rock comprising broken mineral and/or unconsolidated lithic fragments within the regolith, cemented by a finer-grained matrix (Fruland 1983). Additionally, in contrast to monomict regolith breccias that consist of fragments and matrix of identical composition and origin, polymict regolith breccias contain rock fragments that are sourced from various localities on the planetary surface and even from other planetary bodies (Kerridge and Matthews 1988). Hence, a polymict regolith breccia can provide information from an extensive region of a parent body.

The mechanisms that lead to the brecciation and secondary alteration of polymict regolith breccias on the Moon, Mars, and the asteroid 4 Vesta, are the subject of this study. Most of our current knowledge about planetary regolith and regolith breccias stem from the Moon, as samples returned from the moon, observations made on the surface or from the lunar orbit, and lunar meteorites have been studied to understand the dynamic properties of the Moon's surface. However, processes leading to the formation and evolution of regolith breccias can vary on different planetary bodies depending on distinct surface conditions and impact cratering processes. Planetary regolith evolution and surficial processes can be understood by unraveling the lithification and evolutionary histories of regolith breccias.

1.2 Planetary regolith breccia formation

Unlike on Earth, where the presence of life and wind/water interaction produces sedimentary rocks, most planetary regolith breccias are a result of impact events and shock processes. In a hypervelocity impact of a planetary projectile (e.g., asteroids and comets) with the surface of a target planetary body, the kinetic energy from the projectile is converted to shock waves that originate from the point of contact and spread through both the projectile and target (Sharp and DeCarli 2006, Ferrière and Osinski 2013). These shock waves compress and heat the material they propagate through, leading to shock metamorphism, which includes plastic deformation, solid-state transformation, or melting and recrystallization to high-pressure mineral polymorphs (Chao 1967, Ferrière and Osinski 2013). As the shock waves dissipate, the previously compressed material becomes decompressed and is modified to form an impact crater (Ferrière and Osinski 2013).

Meteorite impacts can fragment underlying rocks and disperse material across the surface as ejecta. This results in a heterogeneous layer composed of excavated rock fragments, impact-melt related, and impactor material. Subsequent impact processes can coalesce heterogeneous components of the regolith together to form coherent breccia rock. Mechanisms by which regolith can coalesce include thermal processes such as sintering, annealing, and melting and/or pressure induced processes such as shock welding and compaction (Mckay and Morrison 1971, Kieffer 1975, Hoffmann 2011, Spray 2016). Thus, regolith breccias host geological information that is shaped by impact-related processes and shock metamorphism. Observable shock metamorphic effects in the breccias can reveal the pressure-temperature-time history of the regolith breccia during lithification and/or excavation from its parent body.

Spray (2016) presented how planetary regolith binds together to form regolith breccias in four stages (Fig. 1.1). The first two stages involve crushing, grinding, and mixing of heterogeneous regolith layers via multiple impact events. Unconsolidated planetary regolith is produced in the first two stages. In the third stage, compaction leads to lower porosity and increased strength, and can occur via shock waves, burial, vibrations, or cold pressing (Mckay and Morrison 1971, Spray 2016). The final stage is sintering, a thermal process in which the regolith heats up to and below its melting point (German 2014). As the regolith is heated, loose particles form neck growths along their grain boundaries and ultimately amalgamate to form equigranular textures (German 2014). Grain growth and densification happens at the expense of pore space in the sintering stage (German 2014).

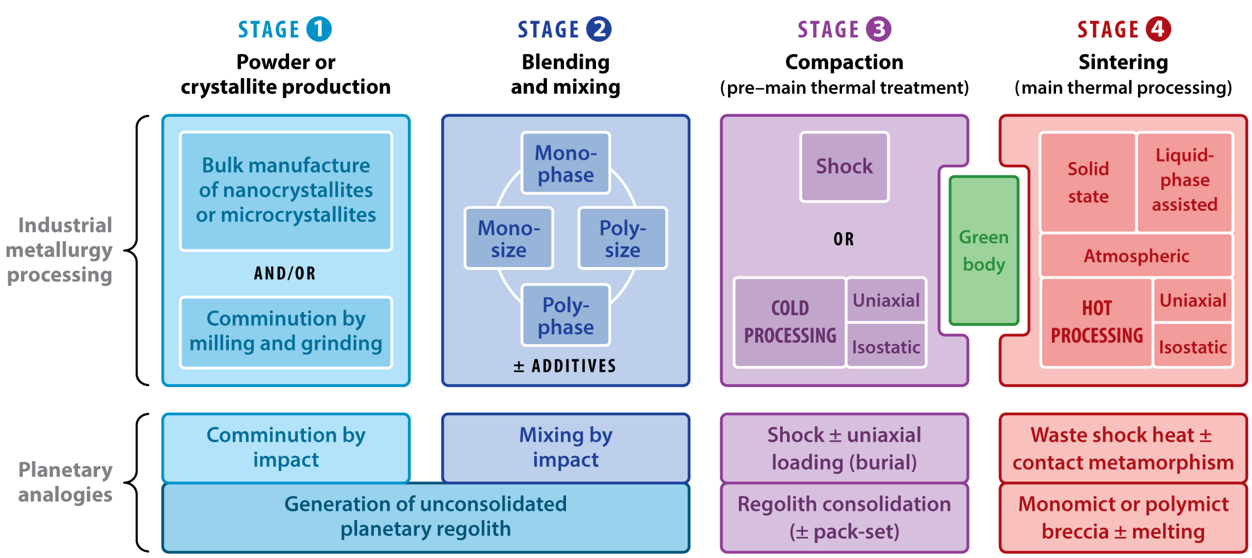

Figure 1.1: Industrial metallurgy processing stages for production of sintered materials, and analogies for planetary regolith generation and breccia formation. Figure adopted from Spray (2016).

1.3 Planetary regolith breccias

Regolith breccias are composed of the components found in the regolith of its parent body and that are bonded together to form a coherent rock. The exact components of a regolith breccia can vary depending on its parent body and the specific location of the breccia's formation. Main components include rock or lithic, mineral, impact-melt fragments, glassy spherules and fragments, and other exogenous fragments like metal grains and organic material that are derived from the impactor to the target body (breccia parent body) in an impact event (Kerridge and Matthews 1988, Hoffmann 2011, Spray 2016). The regolith layer on rocky extraterrestrial bodies has various breccias entrained within or lying on it, that have been transported as ejecta and/or have been excavated from depth by impact. So, at some stage, breccias may also become part of a succeeding regolith breccia (e.g., McCubbin et al. 2016).

Lithic clasts in a polymict regolith breccia can represent diverse crustal lithologies; in planetary regolith breccias these are primarily igneous rocks. Impact melt clasts are generated by melting of the target material (regolith dust, rock clasts, mineral clasts, etc.) during a meteorite impact event on the target body. Impact melt clasts have a compositional makeup and elemental ratios that cannot be achieved by normal igneous processes (e.g., Cohen 2013), because on the surface of the target body, typically a heterogeneous mixture of material is impact melted and crystallize rapidly to form these clasts. Most, not all, impact melt clasts also have characteristic rapidly cooled fine-grained textures that differentiate them endogenous igneous rocks (e.g., Joy et al. 2010).

1.3.1 Lunar regolith breccia samples and meteorites

Regolith breccias from the moon are represented by samples returned from Apollo missions and recovered meteorites. The regolith breccia population from the Apollo missions were all derived from the central nearside of the Moon, from inside the mare basalt regions (relatively young, dark, and low-lying basaltic regions), the highlands, the ridge of the Imbrium Basin, and areas where highland hills meet the mare plains (McKay et al. 1991). The regolith samples and breccias from the mare basalt regions contain abundant mare-derived basaltic rock fragments and mafic minerals like olivine and pyroxene (Simon et al. 1985), and samples from the highlands region contain abundant highland derived lithic fragments (anorthosite rocks) and mineral clasts of plagioclase feldspar (Simon et al. 1983 p. 11, Spudis 1984). The samples acquired from regions between highlands and mare plains are of an intermediate character, and they contain rock and mineral fragments derived from both regions (Simon et al. 1986 p. 15). These are a general description of breccia compositions from different regions on the moon that allow for simple assumptions to be made about the composition of lunar regolith in the mare and highland regions.

Although the Apollo missions evidently sampled a range of geologic terrains on the moon, they represent a limited sample suite focused primarily on the near side of the Moon. In contrast, since lunar meteorites sample arbitrary locations on the moon, they represent a global geologic sampling of the moon, sampling the lunar nearside, polar regions, and far side (Joy and Arai 2013), as noted by the comparison between sample bulk composition and the remote sensing chemical data beyond Apollo sample targets (Mercer et al. 2013, Calzada-Diaz et al. 2015). Additionally, lunar meteorites are always ejected from the lunar surface because of impact events; hence, they allow for a direct study of the shock conditions and processes that lead to their brecciation and/or eventual excavation.

Feldspathic lunar meteorites, most being regolith breccias, are generally linked to the lunar highlands by comparison with the feldspar dominated samples returned from the highland terrane on the lunar nearside. Feldspathic lunar meteorites are rich in aluminum, have low concentrations of incompatible elements, and are comprised of mineral, lithic, breccia, and impact-derived clasts (Korotev et al. 2003). Mineral clasts in these meteorites are dominated by calcic plagioclase and so are other clasts with granular, cataclastic or fine-grained to porphyritic melt breccia textures (Hutchison 2004). Volcanic material from the maria has been found in some studied feldspathic lunar meteorites and impact generated spherules, agglutinates, and breccias are also widely present (Hutchison 2004).

1.3.2 Vestan regolith howardites

Howardite-eucrite-diogenite (HED) are a group of meteorites that are thought to originate from 4 Vesta due to their similar visible and infrared reflectance spectra (Mccord et al. 1970, Binzel et al. 1997). Eucrites are either cumulates, gabbroic rocks that formed from a mafic magma within the crust and contain pigeonite and plagioclase minerals, or basalts that formed as shallow-level sills and dikes, and flows (Mittlefehldt 2015). Diogenites can have diverse lithologies, but they mainly consist of coarse-grained ultramafic rocks dominated by orthopyroxene minerals and harzburgites, that represent an assemblage of olivine and magnesian orthopyroxenes (Beck and McSween Jr. 2010).

Breccia meteorites derived from the surface of asteroid 4 Vesta are called Howardites. Howardites are subdivided into fragmental and regolithic, the latter being lithified remnants of the active regolith of 4 Vesta (Mittlefehldt 2015). Regolithic howardites, referred to as howardites from now on, can also contain either high abundances of trapped solar wind gases or planetary-type noble gases derived from exogenous chondritic material (Cartwright et al. 2013). A polymict breccia with abundant eucrite clasts needs to contain >10% diogenite material to be classified as a howardite, and vice-versa (Delaney et al. 1983). If the breccia has a eucrite:diogenite mixing ratio outside this range, it is classified as either a polymict eucrite or a diogenite breccia.

Howardites contain a mixture of regolithic debris, composed of eucrite and diogenite fragments, glassy and impact-related material, and chondritic or other exogenous clasts derived from impactors, usually carbonaceous chondrite material (Zolensky et al. 1996, Lorenz et al. 2007, Beck et al. 2012). Eucrite clasts are derived from basaltic rocks, gabbroic cumulates and polymict eucrite breccias, and are largely composed of ferroan low-Ca clinopyroxene, high-Ca plagioclase and a silica phase (Delaney et al. 1984, Mayne et al. 2009). Diogenitic clasts are derived from coarse grained orthopyroxenites, harzburgites, and rare dunites, and are composed primarily of orthopyroxene with variable amounts of other minerals including chromite, olivine, exsolved clinopyroxene, plagioclase, and accessory troilite, FeNi metal and phosphates (Mittlefehldt 1994, Bowman et al. 1999). Impact melt clasts are either recrystallized products of impact generated melts or breccia clasts in which impact melt has adhered clasts together (Mittlefehldt 2015). Glass spheres and irregularly shaped particles are also found within howardites, which provides additional evidence that they represent regolith on an airless body (Warren et al. 2009).

1.3.3 Martian regolith breccia meteorite

There is currently only one sample of martian regolith breccia represented by many paired stones. Meteorite regolith breccia NWA 7034 from the surface of Mars has a bulk composition of a basalt on the volcanic rock classification scheme based on the abundance of alkali elements and SiO_2 (Agee et al. 2013). Its mineralogy is dominated by plagioclase (An_{60}–An_{10}), alkali-feldspar, and pyroxenes (mostly pigeonite and augite). Minor minerals include magnetite with a maghemite component and rutile exsolution, pyrite, ilmenite, chromite, zircon, and phosphate minerals (Humayun et al. 2013). The breccia consists of sedimentary (clasts that formed as a result of surficial processes), igneous, impact-melt clasts, and pyroclastic material set in a fine-grained interclast crystalline matrix that has been thermally annealed (Santos et al. 2015). Sedimentary-like lithologies include proto-breccias and siltstones. Pyroclastic-like material includes lapilli. Igneous lithologies have been named and classified inconsistently by various authors; these are summarized in Table 1.1. The breccia is composed of fragmented particles which may have originated as chaotic, atmospherically-deposited material from an impact plume (Goodwin et al. 2022). The impact-plume origin is supported by high Ni and Ir bulk concentrations consistent with differentiation from impact melts (Humayun et al. 2013), presence of amoeboid, glassy interstitial melt, and sintered accretionary lapilli (Nyquist et al. 2016, MacArthur et al. 2019).

The geological history of NWA 7034 and its concomitant stones currently stands as following:

1. Crystallization of igneous components between 4450 – 4200 Ma from alkaline volcanism evidenced from Pb-U and Sm-Nd ages of igneous clasts (Humayun et al. 2013, Nyquist et al. 2016).

2. Excavation and mixing of plutonic igneous, mineral, impact-generated, breccia clasts during impact gardening (a process by which frequent small impacts stir the uppermost regolith) and surface reworking (McCubbin et al. 2016). Proto-breccia clasts indicate sedimentological processes and impact gardening before the clasts were incorporated in NWA 7034 (McCubbin et al. 2016). Apatite grains' secondary alteration is observed before the apatite grains' incorporation in the breccia as well, indicating presence of prior hydrothermal systems near the surface of Mars (Hu et al. 2019, Shang et al. 2022).
3. Lithification of NWA 7034 during an impact event at ~1.5 Ga, indicated by the high Ni and Ir content of the bulk breccia, and impact-related lithologies (Hewins et al. 2017, MacArthur et al. 2019).
4. High temperature oxidizing conditions after the disturbance and lithification event that led to pyroxene breakdown and annealing of the interstitial matrix (Leroux et al. 2016, MacArthur et al. 2019).
5. Postimpact hydrothermal alteration that resulted in pyrite-pyroxene intergrowths and Ni-rich pyrite mineralization throughout the breccia (Lorand et al. 2015).
6. Excavation and ejection at 5 - 15 Mya, during which low shock pressures created mechanical twins in pyroxene (Leroux et al. 2016) and may have caused minor Pb-loss in metamict grains (Tartèse et al. 2014).
7. NWA 7034 has a terrestrial age of ~14 Ka (Lindsay et al. 2021). Signs of terrestrial weathering include Ca-carbonate filled fractures and alteration of pyrite to Fe-oxyhydroxides based on the terrestrial D/H values of the alteration product (Lorand et al. 2015).

Table 1.1: Compilation of types of igneous clasts classified by various authors in NWA 7034 and its paired stones. Based on Humayun et al. (2013), Santos et al. (2015), Wittmann et al. (2015), Hewins et al. (2017), MacArthur et al. (2019).

Clast type	Clast	Description
Igneous	Basalt	Subophitic texture and dominated by plagioclase and pyroxene with minor apatite and oxides. Also known as “gabbroic clast; noritic clasts; granular and subophitic clasts; fine-grained igneous clasts”.
	Trachyandesite	Poikilitic and subophitic texture with irregular grain boundaries and contains abundant K-feldspar. Also known as “monzonitic” or “feldspathic” clasts.
	Basaltic andesite	Granoblastic with pyroxene and plagioclase and minor Fe-Ti oxides. Also known as “noritic clast”.
	Fe Ti and P rich lithologies	Fine-grained texture and relatively large apatite and Fe–Ti oxide grains tending towards euhedral morphologies, and they frequently lack pyroxene. Also known as “basalt clasts (ophitic texture)”.

1.4 Summary and goals

This study has two overarching goals: 1. To identify what components comprise regolith breccias from the Moon, Mars, and 4 Vesta, 2. To identify how these components evolve to become coherent rocks. The geological diversity on the surfaces of the breccias' parent bodies will be elucidated by the systematic analysis of various lithic, mineral, breccia, and impact-melt clasts. The impact-related processes that have imprinted on these regolith breccias will be unraveled by the study of shock effects in a wide range of clasts in these meteorites. Ultimately, the petrogenetic history and evolution of the breccias will be constructed with the aim at decoding the lithification processes embedded in the matrix of the breccias and shock conditions that excavated the meteorite breccias from their parent bodies.

Chapter 2: Samples and Methods

2.1 Samples

2.1.1 Lunar meteorite NWA 14340

Lunar meteorite Northwest Africa (NWA) 14340 was found in Algeria in 2017 as a single 8.26 gram stone and classified as a clast-rich, matrix-supported feldspathic breccia (Gattacceca et al. 2022). NWA 14340 belongs to the NWA 8046 clan of lunar highlands breccias (Korotev 2022). A partially glassy spherule and FeNi metal grains indicates that this meteorite was part of the lunar regolith. Terrestrial alteration includes calcite filling in fractures. One polished thin section of NWA 14340 from MacEwan University was studied here (Fig. 2.1A).

2.1.2 Howardite meteorite Sariçiçek

Sariçiçek is a howardite that fell in Turkey in 2015 and was subsequently investigated by a large consortium study, that provided details about the meteorite's potential source crater, age, fall, mineralogy, petrology, and geochemistry (Unsalan et al. 2019). It has no evidence of terrestrial alteration as it was a recovered fall. The meteorite was classified as a regolithic howardite based on its high siderophile element content and noble gas abundance. One thin section of Sariçiçek from Macewan University was studied here (Fig. 2.1B).

2.1.3 Martian meteorite NWA 10922

Martian NWA 10922 was found in Morocco in 2013 and classified as a basaltic breccia (Bouvier et al. 2017). NWA 10922 is part of the NWA 7034 suite that has 18 other paired stones, based on identical mineralogy, lithologies, major element geochemistry, and oxygen isotopes

(Agee et al. 2013, Humayun et al. 2013, Santos et al. 2015). Terrestrial alteration includes calcite in fractures, and alteration of sulfides to hematite and maghemite. A 2.82g stone of NWA 10922 was provided by the University of New Mexico and cut open to prepare two polished tiles at the University of Alberta; one of these tiles was studied here (Fig. 2.1C).

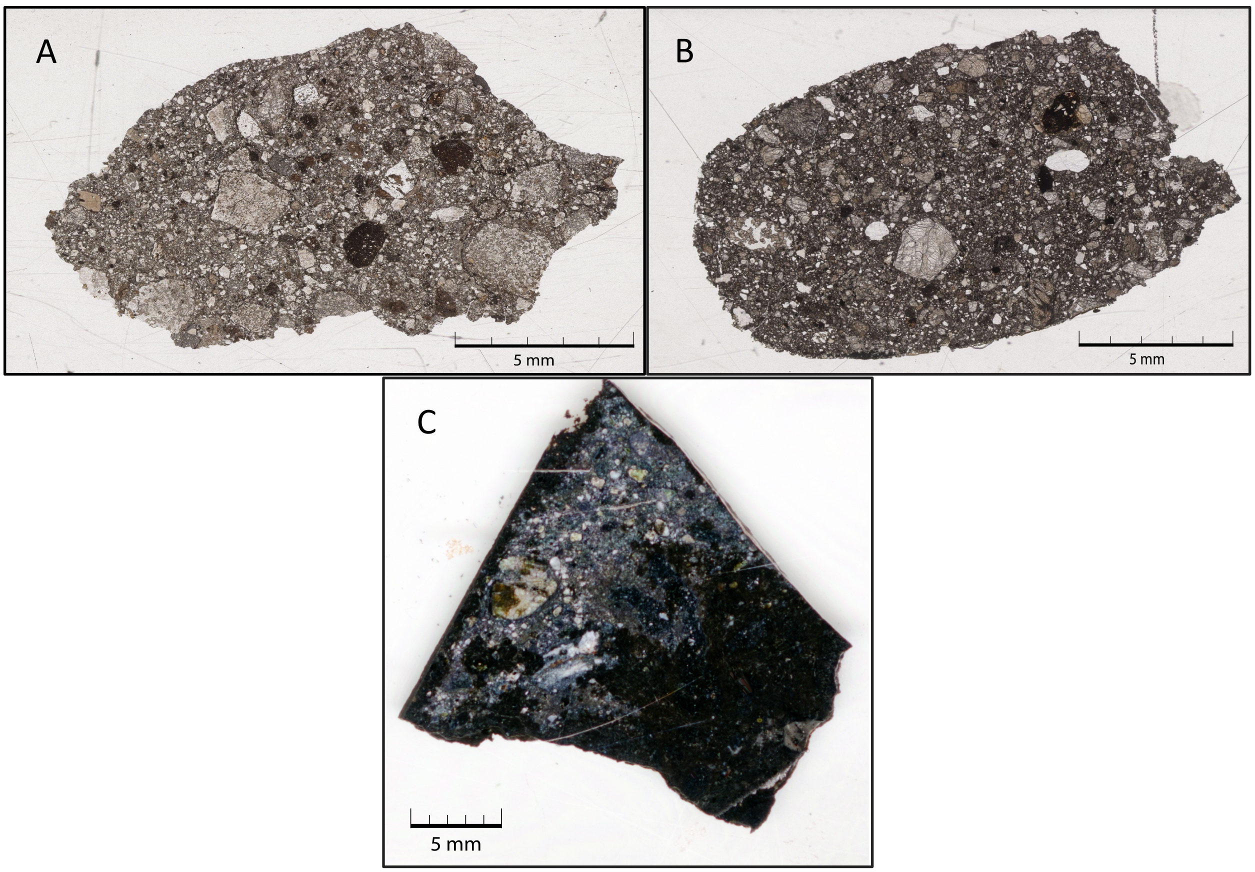

Figure 2.1: Scans of meteorite samples that were investigated in this study: (A)NWA 14340 thin section. (B) Sariçiçek thin section. (C) NWA 10922 tile.

2.2 Methods

2.2.1 Imaging and determining compositional variations

Observations of the samples' mineralogy and textures were made by viewing the samples with the petrographic microscopes equipped with plane polarized and crossed polarized light, within the High Temperature Planetary Petrology Laboratory and Ore Deposits Laboratory at the University of Alberta. Electronic imaging of the samples was performed on a ZEISS Sigma 300 Field Emission Scanning Electron Microscope (FESEM) located within the Department of Earth and Atmospheric Sciences at the University of Alberta. The instrument was operated at 20 kV accelerating voltage and 15 nA in a focused beam mode for Backscattered electron (BSE) imaging and energy dispersive x-ray spectrometry (EDS) analysis. Qualitative spot compositional analysis was acquired using EDS, and additional quantitative analysis was acquired with a JEOL 8900 electron probe microanalyzer (EPMA) also located within the Department of Earth and Atmospheric Sciences at the University of Alberta. Elemental maps of the entire sections of Sariçiçek and NWA 10922 were created using the EPMA. Operating conditions for the microprobe were: Beam energy 20 keV, beam current 30 nA, and a fully focussed beam (diameter <1 μm). Silicates, phosphates, and oxides were analysed, and the standards were Ni metal (Ni $K\alpha$), Cr_2O_3 (Cr $K\alpha$), fayalite (Fe $K\alpha$), rutile (Ti $K\alpha$), diopside (Ca $K\alpha$, Si $K\alpha$, Mg $K\alpha$), albite (Na $K\alpha$), sanidine (Al $K\alpha$, K $K\alpha$), spessartine (Mn $K\alpha$), tugtupite (Cl $K\alpha$), and apatite (P $K\alpha$).

Raman spectroscopic analyses were performed using a Horiba Xplora Plus Raman Spectrometer - Confocal Raman Microscope located within the Department of Physical Sciences at MacEwan University. The Raman spectrometer is equipped with 532 nm laser and 1800 lines/mm diffraction grating. A custom edge filter of 1% was used to adjust the power output of the 100 mW laser and the system was focused with a 100X objective lens that provided a laser spot diameter of ~1 µm (theoretically 800 nm). Peak positions were calibrated using a silicon wafer, and peak fitting was conducted using the Labspec 6 spectroscopy suite software.

2.2.2 Determining clast type, size, and modal mineralogy

Clasts within each meteorite were categorized into lithic, mineral, impact-melt, and breccia types according to the following criteria:

- Lithic clasts: Rock fragments of igneous rocks that contain interlocking and coarse grains of igneous minerals like feldspar, pyroxene, olivine, etc. These clasts most likely crystallized from non-impact igneous processes, and display evidence for fractional crystallization and igneous textures (Santos et al. 2015).
- Mineral clasts: fragments of single mineral crystals.
- Impact-melt clasts: Clasts that formed due to impact melting processes. These clasts are composed of impact melt that has now been quenched or devitrified. Some clasts also contain rock, mineral, and impact-melt clasts in a matrix of glassy or cryptocrystalline impact melt. They may also contain metallic components or projectile contaminant sourced from the impactor. Some clasts may also have textures typical of volcanic rocks like ophitic, porphyritic etc. These clasts have mineral assemblages that are not common in plutonic igneous rocks but could be explained by crystallization from a whole rock melt of one or more than one of the igneous rocks known to exist on the surface of the parent body (Bischoff et al. 2006, Cohen 2013, Osinski et al. 2018).

- Impact-melt spherules: Clasts characterized based on their round shape which is indicative of airborne transport and mineralogy and textures like impact melt clasts (McKay et al. 1991).
- Breccia clasts: These clasts consist of angular mineral and lithic clasts that are set in a fine-grained matrix that has a distinct texture and composition from the bulk matrix of the meteorite. These clasts may contain some glassy or crystalized impact-melt that binds some of the fragments of the breccia together, but unlike an impact-melt clast, the entire clast is not made up of quenched or recrystallized impact melt (McKay et al. 1991, McCubbin et al. 2016).
- Exogenous clasts: Clasts derived from the impactor that are differentiated based on mineral compositions and textures that are common for iron or chondritic materials (Zolensky et al. 1996, Mittlefehldt 2015) .

Only clasts > 0.1 mm in size were analyzed and categorized in this study. This size was used as the minimum limit because most of the lithic clasts were found to be larger than 0.1 mm. While some clasts, mostly mineral and impact-melt, can measure smaller than 0.1 mm, this minimum size threshold was adopted for the characterization of each meteorite that would be satisfactory in creating a clast inventory while aligning with the time constraints of the study. Additionally, as most clasts are angular to subrounded, the size of each clast was measured along its longest axis.

Modal mineralogy was determined for lithic clasts in the program ImageJ (Schneider et al. 2012). BSE images of lithic clasts were imported, and their scales were set using the “set scale” tool. Images were cropped to exclude surrounding areas of the clast from the measurement. The “threshold” tool was used to differentiate minerals based on their greyscale values. The area covered by each mineral phase was measured as a percentage of the total clast area. To ensure accuracy, the measured areas were normalized to 100%, eliminating any background from the measurement.

Chapter 3: Results – Characterization of Clasts in NWA 14340, Sariçiçek, and NWA 10922

3.1 NWA 14340

NWA 14340 is a breccia composed of lithic, mineral, and impact-melt clasts, and spherules (Fig. 3.1A). Clasts range in colour from light (plagioclase rich) to dark (glassy and fine-grained impact melt clasts), set in a fine-grained to glassy matrix. The average size of lithic clasts is 1.4 ± 0.4 mm (n=26), impact melt clasts is 1.1 ± 0.6 mm (n=12), and one spherule is 0.4 mm. All the clasts have sub-angular shapes and irregular edges. The major minerals are plagioclase ($An_{92.0-98.1}$), pyroxene ($En_{41.0-80.7}Wo_{2.6-42.8}$), and olivine ($Fo_{63.6-79.1}$). Clasts identified in NWA 14340 make up 26% of the total surface area of the sample. Among these are lithic clasts (20%) and impact-melt clasts and spherules (6%). The inventory of clasts studied in NWA 14340 is summarized in Table 3.1.

Table 3.1: Characteristics of clast types analyzed in NWA 14340 in this study: size range, mineralogy, textures, approximate modal mineralogy, and shock effects.

	Number of Clasts	Approximate Size Range (mm)	Mineralogy and Textures	Range of Approximate Modal Mineralogy	Range of Shock Effects
Lithic Clasts	26				
Anorthosite	5	1.2 – 2.3	- Ca-rich plagioclase crystals, some crystals occasionally enclose small anhedral pyroxene grains	- 90-99% plagioclase - 0-5% Fe-rich olivine or pyroxene, - <1% opaques	- Fractured minerals - Plagioclase exhibits patchy undulose extinction and PDFs - One clast exhibits grain boundary melting between orthopyroxene and plagioclase.
Anorthositic Norite	3	0.8 – 1.2	- Subhedral orthopyroxene and Ca-rich plagioclase grains. - One clast has a granoblastic texture	- 83-88% plagioclase - 7-13% orthopyroxene - 0-9% olivine - <1% opaques	- Fractured minerals - Plagioclase exhibits patchy undulose extinction and PDFs - Two clasts contain plagioclase grains exhibit melting and recrystallization. One of these clasts has pyroxene that displays mechanical twinning.
Anorthositic Gabbro	1	2.1	- Small subhedral grains of clinopyroxene and large grains of Ca-rich plagioclase - Granoblastic texture	- 84% plagioclase - 15% clinopyroxene - <1% opaques	- Fractured minerals - Plagioclase is partially isotropic and exhibits mosaicism. - Pyroxene exhibits mosaicism
Troctolite	6	1.1 – 1.9	- Subhedral to anhedral rounded Mg-rich olivine grains, occasionally mantled by Mg-rich	- 61-71% plagioclase - 22-37% olivine - 0-10% orthopyroxene	- Fractured minerals - Plagioclase exhibits patchy undulose extinction and some have PDFs - A portion of one clast has melted and recrystallized

			orthopyroxene, with Ca-rich plagioclase - Granular textures	- <1% opaques	
Norite	4	0.7 – 2.0	- Orthopyroxene grains enclosing rounded olivine and Ca- rich plagioclase grains - Subhedral orthopyroxene grains associated with anhedral Ca-rich plagioclase grains - Poikilitic textures	- 61-78% plagioclase - 15-30% orthopyroxene - 0-8% olivine - <1% opaques	- Fractured minerals - Plagioclase is partially isotropic, exhibits patchy undulose extinction and some have PDFs - Some clasts have olivine grains that exhibit undulose extinction. - Plagioclase in one clast experienced fine-grained recrystallization.
Olivine Norite	2	1.5	- Rounded and anhedral Mg-rich or Fe-rich olivine grains rimmed by orthopyroxene and set in Ca-plagioclase groundmass	- 47-71% plagioclase - 20-34% orthopyroxene - 20% olivine - <1% opaques	- Fractured minerals - Plagioclase exhibits patchy undulose extinction and some have PDFs
Gabbronorite	3	1.3 – 2.1	- Subhedral large clinopyroxene grains in contact with and occasionally rimmed by Fe-rich orthopyroxene grains and set in Ca-rich plagioclase groundmass - Poikilitic and granoblastic textures	- 47-65% plagioclase - 15-32% clinopyroxene - 16-20% orthopyroxene - <1% opaques	- Fractured minerals - Some plagioclase is partially isotropic, others exhibit patchy undulose extinction and PDFs -
Gabbro	2	1.2 – 1.6	- Subhedral clinopyroxene and olivine grains set in	- 70-76% plagioclase	- Fractured minerals - Plagioclase exhibits patchy undulose extinction and some have PDFs

			Ca-rich plagioclase groundmass. - Granoblastic and nesophitic texture	- 22-24% clinopyroxene - <1-8% olivine - <1% opaques	- Plagioclase and pyroxene in a clast experienced melting.
<u>Impact-Melt Clasts</u>	12	0.4 – 2.0	- Variety of crystalline, clast bearing, and glassy clasts. - Two clasts have a porphyritic texture with plagioclase phenocrysts set in a fine-grained groundmass of orthopyroxene, clinopyroxene, olivine, and plagioclase - One unique clast consists of plagioclase laths surrounded by altered Fe-rich olivine and Mg-rich olivine and plagioclase in symplectic texture		
<u>Spherules</u>	2	0.3 – 0.5	- Spherical devitrified impact-melt clasts. - One clast has rounded plagioclase, pyroxene, and olivine clasts embedded within the matrix.		

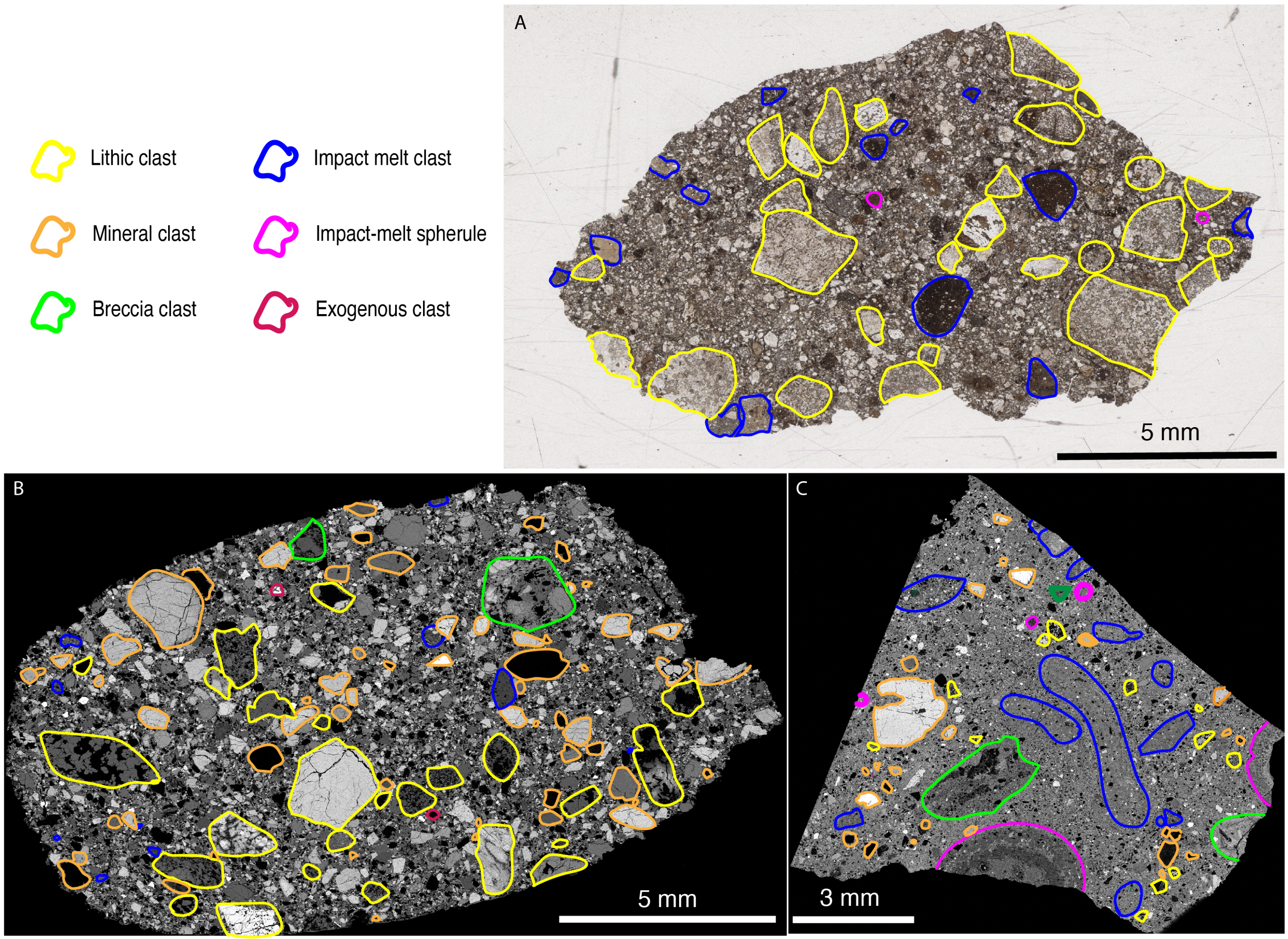

Figure 3.1: Meteorite scan and elemental maps. (A) Transmitted light (TL) scan of NWA 14340. (B) Mg elemental map of Sariçiçek. (C) Mg elemental map of NWA 10922 with groups of clasts outlined in their representative colours.

Lithic clasts in Table 3.1 are named after igneous rocks, following the IUGS recommended classification scheme (Le Maitre et al. 2005), only to provide a description and not imply petrogenetic history. Anorthositic clasts are the most abundant lithic clasts in this sample, followed by norites, troctolites, gabbronorites, and gabbro (Fig. 3.2A-F). Anorthosites have >90% plagioclase, whereas the plagioclase content in anorthositic norites and gabbros is between 80 and 90%. The smallest studied impact melt clast has a size of ~ 0.37 mm, although there are glassy particles and impact melt materials that are much smaller, ~30 µm, in the matrix. The studied impact-melt clasts range from dark to light brown in colour. Impact melt clasts include quenched mafic composition glass with or without mineral clasts, basaltic composition microcrystalline glass, and fine plagioclase laths in a much finer mafic to ultramafic composition cryptocrystalline matrix (Fig. 3.3A-C). Most impact melt clasts also contain disseminated Fe metal specks or globules throughout the clast, indicative of melt mixing before quenching or crystallizing (Fig. 3.3A-B). Two impact-melt spherules were identified in NWA 14340: one of the spherules has a uniform quenched texture that has a composition consistent with a mixture of olivine and plagioclase. The second spherule includes sub-rounded clasts of plagioclase, pyroxene, and olivine set in a fine-grained and quenched matrix of basaltic composition (Fig. 3.3C). Two impact melt clasts have porphyritic textures, where plagioclase mineral grains with fine-grained texture are embedded in a matrix composed of small, irregularly shaped pyroxene and olivine with interstitial plagioclase (Fig. 3.3D).

Mono-minerallic clasts range in size from <10 µm – 500 µm and have irregular edges that are embayed. Mineral clasts are dominated by Ca-rich plagioclase as large as 1.24 mm. Other large mineral clasts include ferroan pyroxene with high-Ca pyroxene exsolution lamellae and orthopyroxene. Large pyroxene clasts range in size from 150 µm to 500 µm. No large olivine clasts that were > 100 μm were identified; they are all present within the matrix with average size of ~ 30 μm and range in composition from Mg to Fe rich.

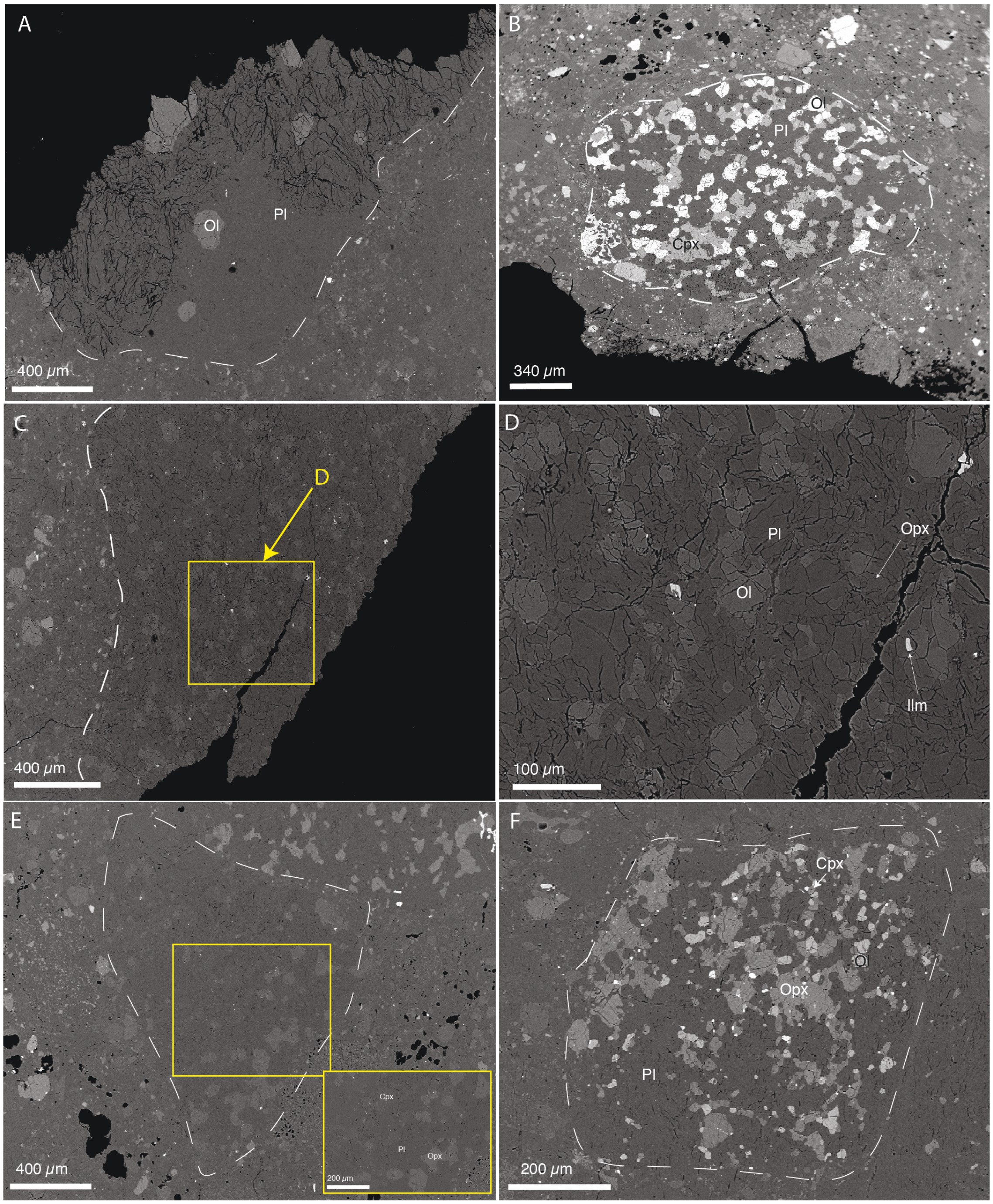

Figure 3.2: BSE images of distinct lithic clasts in NWA 14340. Clast boundaries are delineated with thin white dashed lines, and certain images include zoomed-in inset images in yellow boxes. (A) Anorthosite (B) Gabbro (C-D) Troctolite (E) Gabbronorite (F) Norite. Cpx – Clinopyroxene, Fe – Fe metal, Ilm – Ilmenite, Ol – Olivine, Opx – Orthopyroxene, and Pl – Plagioclase.

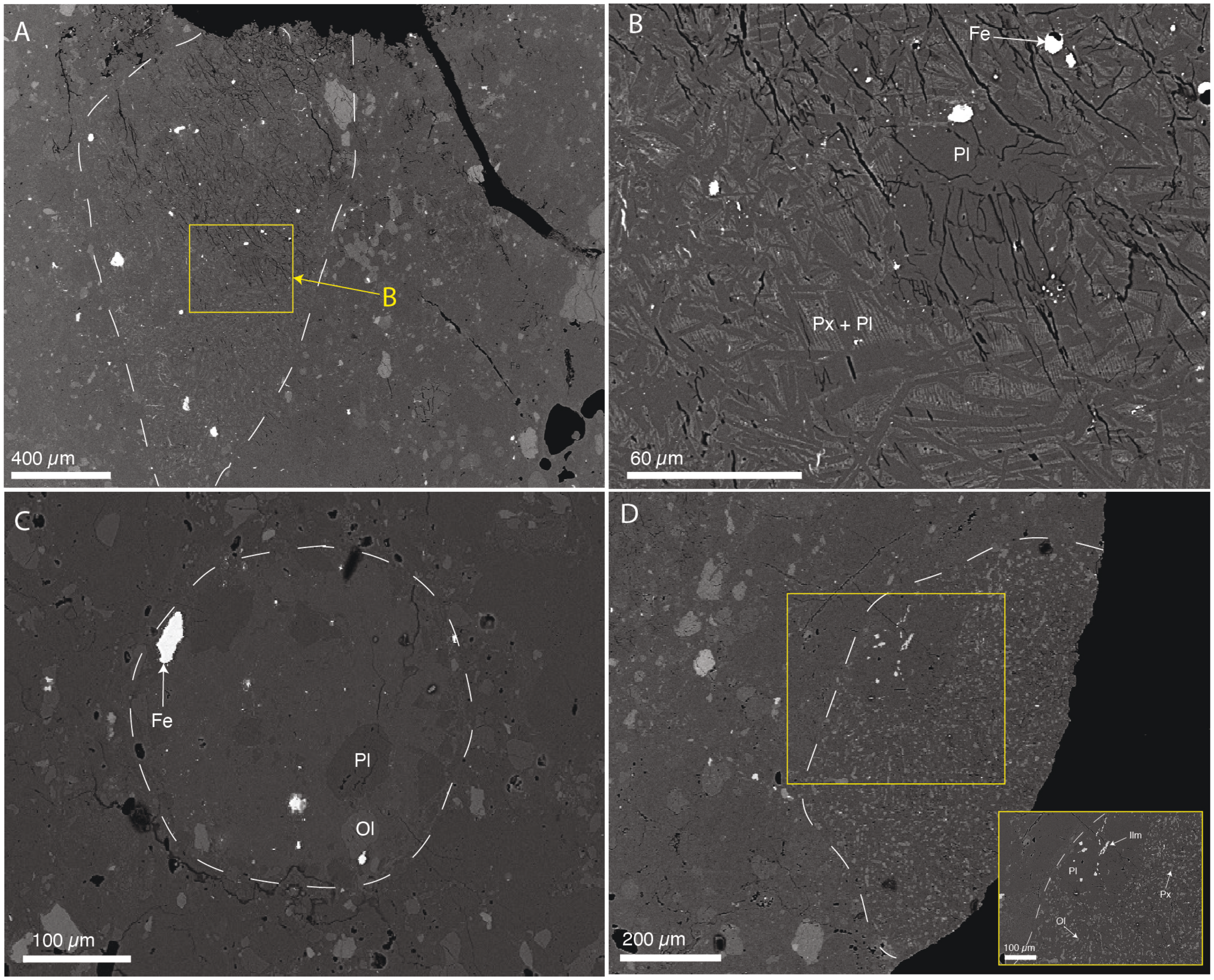

Figure 3.3: BSE images of impact melt clasts and impact-melt spherules in NWA 14340. (A-B) Impact melt clast with plagioclase surrounded by fine-grained pyroxene and plagioclase (C) Impact melt spherule (D) Impact melt clast with porphyritic texture. Px – Pyroxene.

3.1.1 Shock effects

Fractures are pervasive in every lithic clast. Other developed shock effects common in lithic and mineral clasts include patchy undulose extinction (Fig. 3.4A-D) and planar deformation features (PDFs; Fig. 3.4E-G) in plagioclase and undulose extinction to weak mosaicism in pyroxenes. In some lithic clasts, plagioclase has transformed to diaplectic glass, maskelynite. This is accompanied by PDFs in pyroxene in a few clasts (Fig. 3.5A-C). Three lithic clasts with abundant plagioclase (68% - 86% modal mineralogy) have some plagioclase grains with vesicles (Figs. 3.5D-F and I-K). The plagioclase in these clasts is compositionally uniform in BSE images (Fig. 3.5I) and appears in a fine-grained recrystallized texture under cross-polarized light, where plagioclase crystals appear to have nucleated radially from common centers (Figs. 3.5Fand K). This texture is very faint in plane polarized light (Fig. 3.5J). The Raman spectrum acquired from the fine-grained exture area has sharp peaks in ~506 cm-1 region (Fig. 3.5G). The Raman spectrum has sharp peaks and agrees with crystalline plagioclase phase. In all these clasts, orthopyroxene displays mosaicism, and its Raman spectrum has broad and low intensity bands (Fig. 3.5H).

A troctolite clast with an overall granoblastic texture contains an area with plagioclase surrounded by fine-grained matrix composed of olivine and plagioclase (Fig. 3.6A-B). The matrix of this portion has Fe metal globules throughout (Fig. 3.6B). The texture of this portion of the clast is consistent with recrystallization, most likely because of impact heating. Notably, the contact between the recrystallized portion and the matrix of NWA 14340 is sharp (Fig. 3.6A). Thus, the history of this clast involved impact heating and melting prior to being incorporated in NWA 14340. In the intact region of the clast, olivine and orthopyroxene are mosaiced and plagioclase has PDFs and has partially transformed to maskelynite.

A coarse-grained clast has an area near its boundary that is composed of plagioclase, olivine, and pyroxene set in a fine-grained matrix of pyroxene and plagioclase (Fig. 3.6C-D). This portion has a diffuse boundary with the matrix of NWA 14340 (Fig. 3.6D). In the interior of this clast, there are large vesicles, and the pyroxene is anhedral and composed of microlites (Fig. 3.6C). These textures are consistent with recrystallization likely caused by impact heating. The observations suggest that the clast experienced in-situ impact heating, leading to the recrystallized portion interacting with the surrounding matrix, and the recrystallization of pyroxene.

One anorthositic clast has irregular grain boundaries between plagioclase and Mg-rich orthopyroxene (Fig. 3.6E-F). The plagioclase contains small vesicles near its grain boundary and has a smooth appearance in the BSE images, while orthopyroxene is fractured (Fig. 3.6F). This suggests that the two phases experienced melting along their grain boundaries, and plagioclase experienced transformation to maskelynite. The remaining clast is composed of plagioclase grains with PDFs and one olivine grain that has weak planar fractures (Fig. 3.6E).

One impact melt clast is composed of a cryptocrystalline intergrowth of plagioclase and olivine (Fig. 3.6G-I). Fe-Ni metal specks are distributed throughout the clast, and there is one large Fe-Ni globule near which there is a vesicle (Fig. 3G). Under crossed-polarized light, this clast displays a spherulitic texture in which fine-grained crystals radiate outwards from common centers (Figs. 3.6H). The spherulitic texture is consistent with devitrification. Fine-grained plagioclase, pyroxene, and olivine fine-grained assemblage is present along the edges of this clast, overprinting the devitrification textures (Figs. 3.6G). The pyroxene, plagioclase, and olivine textures are consistent with recrystallization.

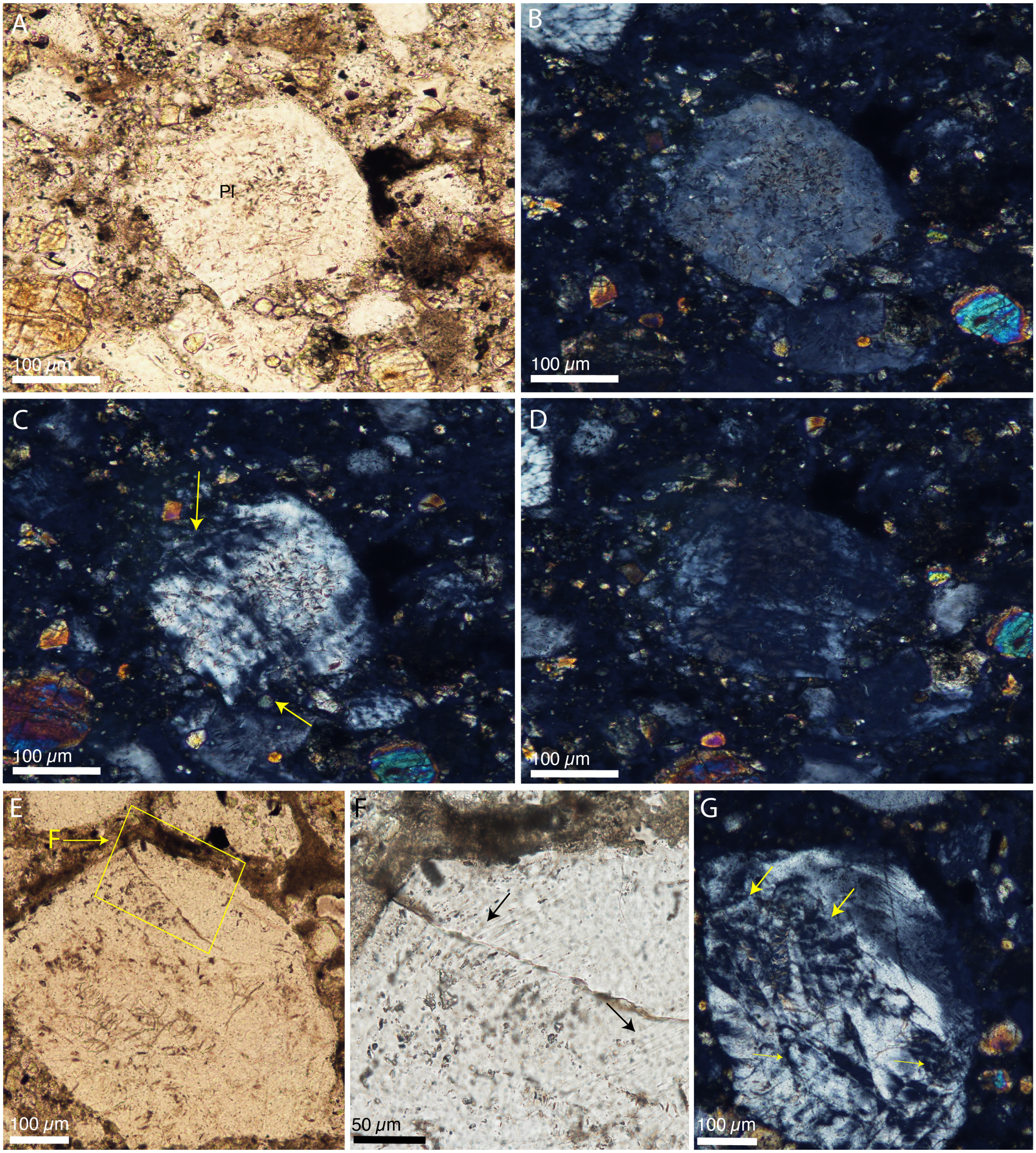

Figure 3.4: Optical microscopy images of plagioclase clasts in NWA 14340 exhibiting undulose extinction in plane-polarized light (PPL; A.E-F) and cross-polarized light (XPL; B-D and G). Yellow arrows indicate patchy extinction texture of plagioclase crystal in C and G. Black arrows indicate PDFs in F.

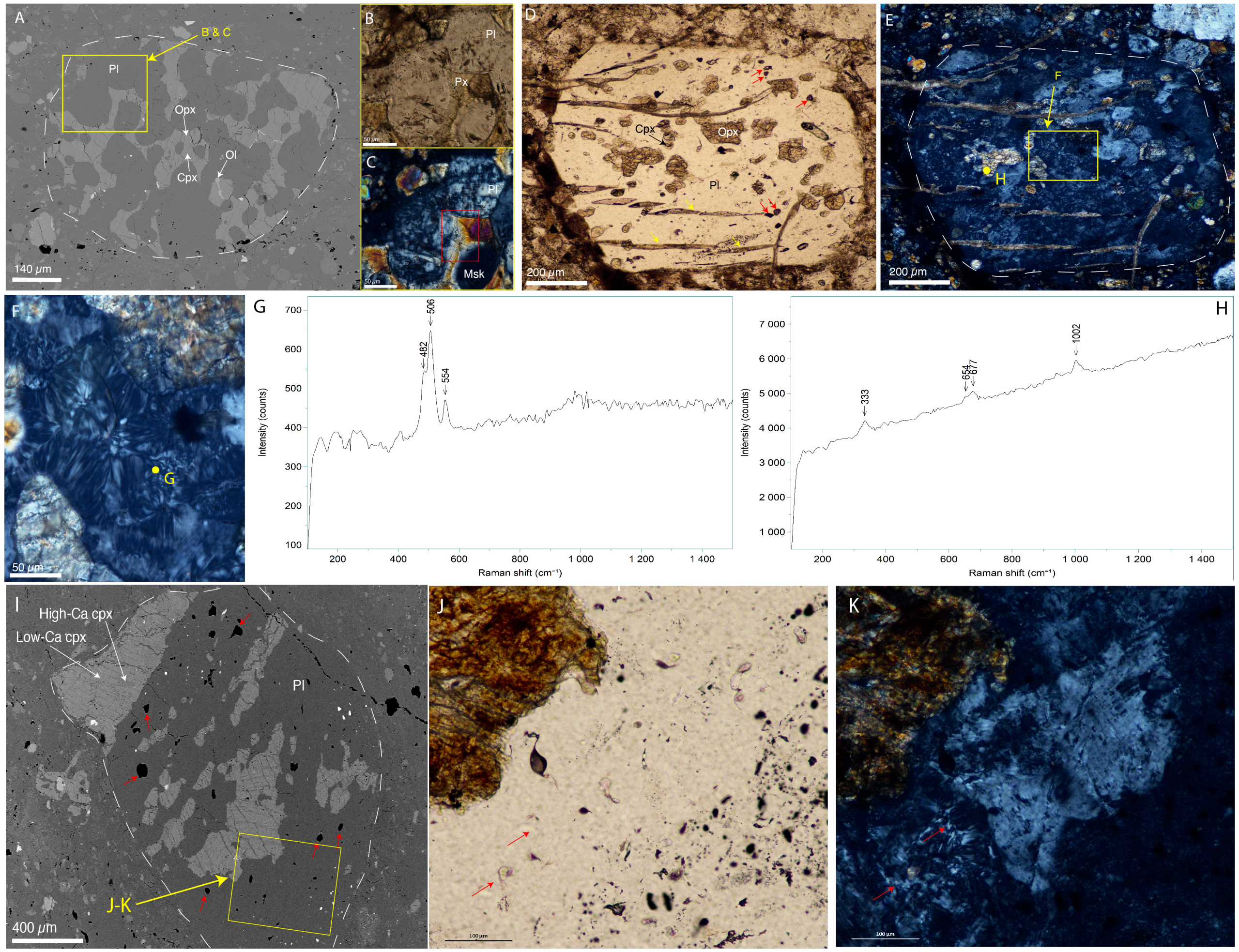

Figure 3.5: Images of clasts with maskelynite and fine-grained textures in NWA 14340, and their respective Raman spectra. (A-C) Noritic clast in BSE image in A, with plagioclase grains that have partially transformed to maskelynite in PPL in B and XPL in C. PDFs are present within the pyroxene in the red box in C. (D-F) Red arrows indicate vesicles and yellow arrows indicate calcite filled fractures in D. Fine-grained plagioclase in PPL in D and XPL in E-F. (G-H) Raman spectrum of fine-grained plagioclase in G and shocked pyroxene in F from clast in D. (I-K) Red arrows indicate vesicles in I. Fine-grained plagioclase in BSE image in I, PPL in J, and XPL in K. Red arrows indicate the fine-grained plagioclase crystals in J-K.

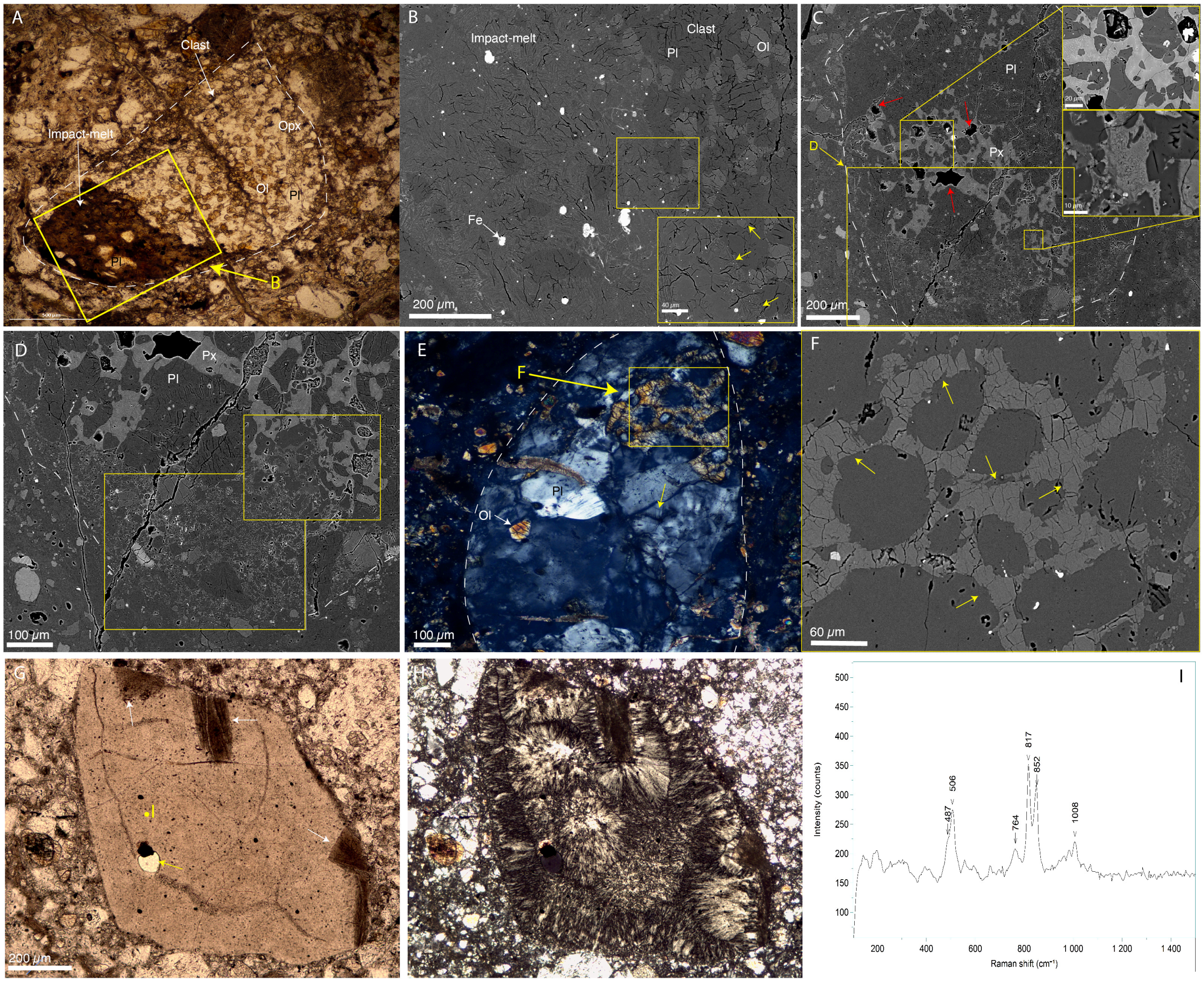

Figure 3.6: Images of clasts in NWA 14340 with recrystallization and devitrification textures. (A-B) A troctolite clast that recrystallized along the left edge, labeled "impact melt", in PPL and BSE image. The zoomed in inset image displays the interface between the recrystallized area on the left and clast on the right in B, with the yellow arrows indicating digested plagioclase and orthopyroxene grains. (C) A gabbroic clast with recrystallized plagioclase and pyroxene. The red arrows indicate vesicles. The zoomed in inset images display pyroxene crystallites set in pyroxene glass. (D) The areas within yellow boxes show in-situ melting and recrystallization textures. (E-F) An anorthosite clast in XPL image in E and BSE image in F. Yellow arrows point towards PDFs in plagioclase in E and towards the irregular grain boundary between orthopyroxene and plagioclase, and small vesicles in F. (G-H) Impact melt clast with spherulitic texture in PPL and in XPL. White arrows point towards recrystallized edges in G. (I) Raman spectrum from yellow spot in G.

3.2 Sariçiçek

Sariçiçek has abundant mineral, lithic, and impact-melt clasts set in a clastic matrix (Fig. 3.1B). The major minerals are pyroxene ($En_{28.7-75.3}Wo_{1.4-44.4}$) and plagioclase ($An_{86.7-91.9}$). The average clast sizes are as follows: lithic clasts 0.9 ± 0.5 mm (n=17), impact melt clasts 0.3 ± 0.2 (n=6) mm, mineral clasts 0.4 ± 0.4 mm (n=21), breccia clasts 1.5 ± 0.8 mm (n=2), and exogenous clasts 0.2 ± 0.1 mm (n=2). Clasts range in colour from white (plagioclase mono-mineral clasts) to dark (impact melt clasts) and opaque (FeNi metal). Clasts identified in Sariçiçek make up 27% of the total surface area of the sample, comprised of lithic clasts (10%), mineral clasts (11%), impact-melt clasts (2%), breccia clasts (3%) and exogenous clasts (< 1%). The inventory of clasts studied in Sariçiçek is summarized in Table 3.2.

Table 3.2: Characteristics of clast types analyzed in Sariçiçek in this study: size range, mineralogy, textures, approximate modal mineralogy, and shock effects.

	Number of Clasts	Range of Size (mm)	Mineralogy and Textures	Range of Approximate Modal Mineralogy	Range of Shock Effects
Eucritic Lithic Clasts	13				
Fine-to-medium grained basalt	10	0.4 – 2.0	- Coarse to fine grained ferroan pyroxene with high-Ca exsolution lamellae and Ca-rich plagioclase - Three clasts have zoned pyroxenes with Mg rich cores and Fe rich rims. - Ophitic to sub-ophitic, poikilitic, granoblastic textures - Some clasts are overprinted with thermal annealing textures	- 13-55% plagioclase - 37-85% pyroxene - <1 – 2% opaques - 0-13% tridymite - 0-3% olivine	- Fractured minerals - Some clasts have pyroxene grains that exhibit undulose extinction and plagioclase with mosaicism. - In one clast, plagioclase has recrystalized and displays grain boundary migration in pyroxene grains - In another clast, plagioclase has PDFs and pyroxene and plagioclase have recrystallization textures.
Eucrite Cumulate	1	0.7	- Cumulate pyroxene grains set in basaltic composition groundmass composed of silica glass, smaller	- 20% plagioclase - 34% Mg-orthopyroxene - 34% ferroan pyroxene	- Fractured minerals - Silica has transformed to diaplectic glass - Groundmass contains shock melt that was mobilized interstitial coarser pyroxene grains.

			plagioclase and pyroxene grains, the later displaying Fe-Ti-Cr oxide exsolution and bent clinopyroxene exsolution lamellae	- 8% tridymite - < 1% opaques	
Diogenitic Lithic Clasts	4			-	-
Olivine Orthopyroxenite	2	1.3 – 1.5	- Laths of orthopyroxene and olivine in a groundmass composed of fin-grained clinopyroxene and plagioclase intergrowth. - Large zoned and rounded orthopyroxene grains, occasionally mantled by olivine, embedded in a cryptocrystalline to glassy groundmass	- 70% Mg-rich orthopyroxene - 15-20% olivine - 8-10% matrix (plagioclase + clinopyroxene ± opaques) - 0-3% chromite and/or ilmenite inclusions	- Fractured minerals - One clast has orthopyroxene laths that exhibits PDFs and mosaicism.
Orthopyroxenite	1	1.8	- Large clast composed of orthopyroxene grains with chromite inclusion and filling in fractures	- 99% Mg-rich orthopyroxene - <1% opaques	- Orthopyroxene grains exhibit strong mosaicism and pervasive fractures
Dunite	1	1.0	- Anhedral and subrounded olivine grains with anhedral	- 93% olivine - 7% FeS and chromite	- Fractured olivine

			iron-sulfide grains throughout	
Breccia Clast	2	0.7-2.1	- One clast is composed of eucritic lithologies that are set in a fine-grained basaltic composition matrix - One large clast has numerous smaller clasts within shock melt pocket that is mantled by Fe-Ni metal and thermally annealed material.	- Fractured minerals - One breccia clast contains a shock melt pocket, plagioclase and silica grains that were transformed to diaplectic glass, PDFs in silica, and mosaicism in pyroxenes
Impact Melt Clasts	6	0.2 – 0.8	- Partially digested clasts in cryptocrystalline to fine-grained basaltic composition matrix	
Exogenous clast	2	0.1-0.2	- Mg-rich orthopyroxene and forsterite-rich olivine set in an extremely fine-grained matrix of likely phyllosilicate material - Kamacite globule with taenite rods and silicate phases mixed in from the matrix	
Mineral Clasts			-	
Olivine	5	0.1 – 0.2	- Anhedral clasts	- Fractured minerals

			- Three of the studied Fe-rich olivine clasts have vermicular intergrowths of breakdown products	
Pyroxene	15	0.1 – 1.7	- Orthopyroxene - Ferroan pyroxene with high-Ca lamellae	- Fractured minerals - Pyroxene mineral clasts display undulose extinction to mosaicism. - Four orthopyroxene clasts contain iron-sulfide beads throughout - One orthopyroxene clast has shock vein cutting through it. The shock vein contains pyroxene globules and exsolved sulfide spherules set in glass of pyroxene composition.
Plagioclase	5	0.1 – 1.3	- Albite twinning - Pyroxene inclusions	- Fractured minerals - Undulose extinction to mosaicism - One large clast was fragmented, likely along a slip plane, and exhibits twin offset, mosaicism, and pervasive fracturing
Silica	5	0.1 – 0.3	- Tridymite and quartz clasts - Some clasts have blebs of troilite.	- Fractured minerals

Sariçiçek's lithic clast inventory is dominated by eucritic lithologies (Table 3.2). The most abundant type of clast is fine-to-medium grained basalt with ophitic to sub-ophitic and coarse-grained textures (Figs. 3.7A-B). Most of the basalt clasts include high Ca-clinopyroxene exsolution lamellae in orthopyroxene host. Some basalt clasts also include pyroxene inclusions in plagioclase, and Fe-Cr-Ti-rich exsolution in pyroxenes. Five of the basalt clasts have additional secondary alteration that includes sulfidization of pyroxene that led to alteration products of troilite, Fe-rich olivine, and silica; Fe-enrichment along, and fayalitic olivine within, cracks and fractures (Fig. 3.7A); and plagioclase in current and healed fractures within pyroxene grains. The secondary textures do not extend beyond the clasts into the matrix. Only one cumulate eucrite was identified with coarse cumulate pyroxene crystals with the composition $En_{67.9}Wo_{2.8}$, n = 3 (Fig. 3.9H). Four diogenite lithic clasts were identified in Sariçiçek, the most abundant being olivine orthopyroxenite (Figs. 3.7C and E). One olivine orthopyroxenite clast has a thermally annealed fine-grained matrix and Fe metal lining along the boundary between olivine and plagioclase (Fig. 3.7C-D). A dunite clast is composed of anhedral and rounded olivine grains, with anhedral grains of iron-sulfide filling in pore space or fractures in the clast (Fig. 3.7F). The fracture-filling sulfide is because of heating during atmospheric entry, as indicated by the veinlets being located adjacent to the fusion crust.

Two breccia clasts were identified in Sariçiçek. One breccia clast has a large clast of high-Ca clinopyroxene, fayalitic olivine, and ilmenite (Fig. 3.7G). The matrix of the breccia is composed of fragmented plagioclase and pyroxene, and minor quartz, in a clastic texture (Fig. 3.7G). The second breccia clast is a large clast that has a dark shock melt pocket, surrounded by Fe-Ni metal, and further mantled by thermally annealed matrix, due to contact with hot Fe-Ni metal (Fig 3.8). Impact melt clasts in Sariçiçek display two types of textures: 1. clasts of pyroxene, plagioclase, quartz, and olivine, with irregular edges, in cryptocrystalline to glassy matrix or fine-grained matrix of the recrystallized material from the melt that likely originated from the digested clasts (Fig. 3.7H); 2. coarser grained intergrowth of plagioclase and pyroxene with partially digested grains of pyroxene. Some impact-melt clasts have Fe-Ni globules dispersed throughout the clasts.

Two exogenous clasts were identified in Sariçiçek. One of these clasts was identifiable in PPL as the matrix around this clast is shock darkened, indicative of in-situ emplacement (Fig. 3.7B). The clast consists of kamacite with rods of taenite, and silicate phases from the matrix within the rim of the globule (Fig. 3.7B). There are other clasts of Fe-metal aggregates with orthopyroxene and/or olivine within Sariçiçek, but they have a sharp contact with the matrix, indicating that they are remnants of previous impactors or micrometeorites. The second exogenous clast is composed of orthopyroxene and olivine, surrounded by a fine-grained matrix (Fig. 3.7I). The olivine and orthopyroxene in this clast are extremely Mg rich (Mg# of olivine ≈ 0.97, based on EDS compositions) which is unlike any other eucrite or diogenite clast identified in Sariçiçek. Such Mg-rich composition is consistent with carbonaceous chondrite clasts identified in other howardites (Lorenz et al. 2007).

Mineral clasts are made up of pyroxene, plagioclase, tridymite and quartz, and minor olivine, ilmenite, chromite, phosphates and FeS. Mono-minerallic clasts have a size range from ~100 µm to < 10 µm. Pyroxene occurs as clasts of orthopyroxene or ferroan pyroxene. Some orthopyroxene ($En_{48.7}Wo_{3.7}$) clasts contain exsolution lamellae of augite ($En_{39.0}Wo_{39.2}$). Some orthopyroxene clasts are clouded with opaque phases. Most of the ferroan pyroxene ($En_{34.4}Wo_{7.0}$) clasts have augite ($En_{28.9}Wo_{42.4}$) exsolution lamellae. Four pyroxene mineral clasts have fractures filled with plagioclase and one with quartz, additionally a few clasts have Fe-enrichment along cracks. Plagioclase clasts have a Ca-rich composition and most contain albite twins. Some clasts have abundant clouding. Olivine clasts have varying Fe and Mg content and out of the five clasts studied, three of the Fe-rich olivine clasts have vermicular breakdown products of troilite + Mg-orthopyroxene or troilite + clinopyroxene + silica.

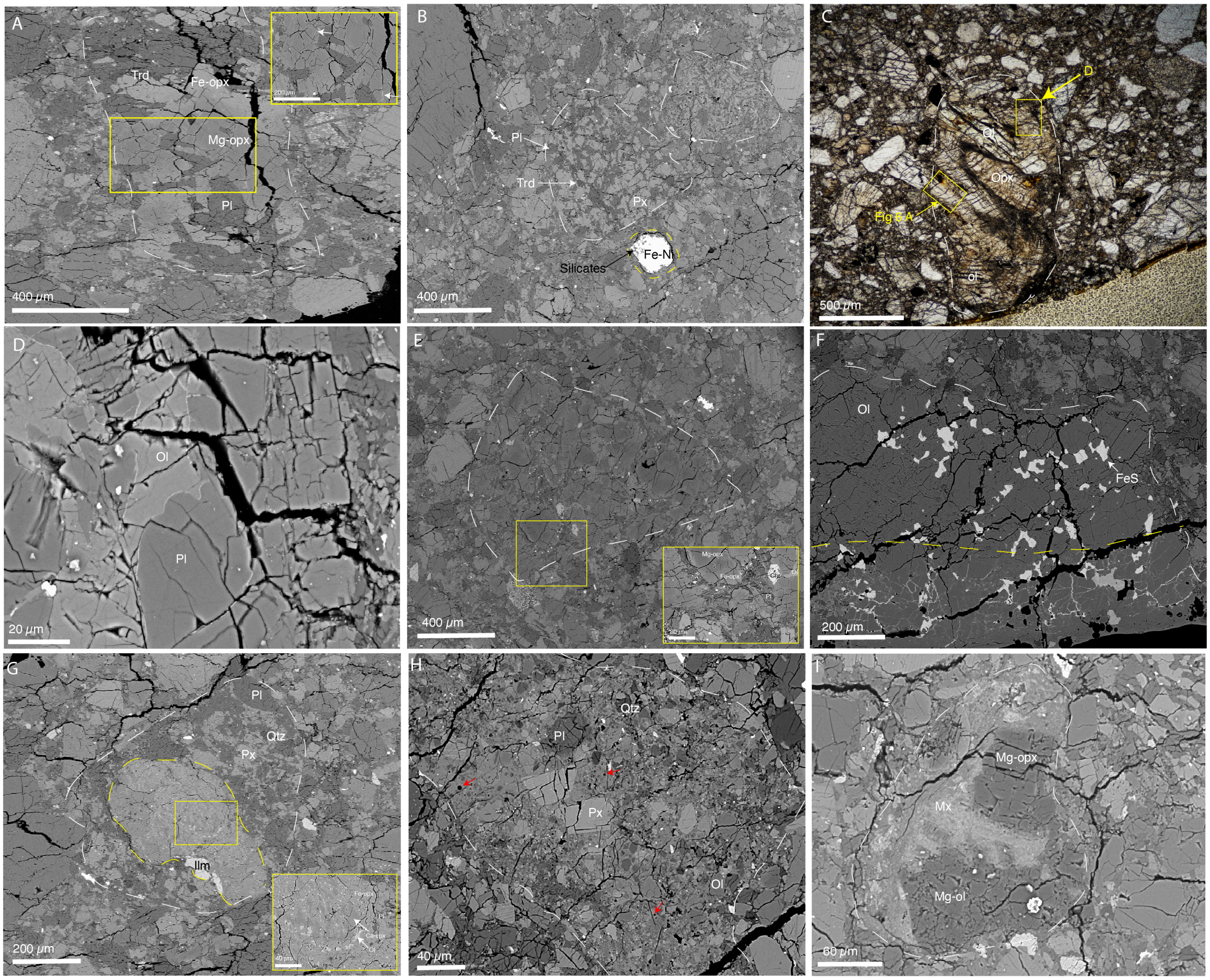

Figure 3.7: Images of distinct lithic clasts, breccia, impact-melt, and exogenous clasts in Sariçiçek. (A) BSE image of a basalt clast with ophitic texture. White arrows indicate Fe-enrichment and fayalitic olivine in healed fractures in the inset. (B) BSE image of two basaltic clasts of ophitic to sub-ophitic textures, outlined in white dashed lines. A Fe-Ni metal globule is outlined in a yellow dashed line. (C-D) PPL and BSE images of an olivine-orthopyroxenite clast with shock darkened matrix and Fe enrichment along olivine and plagioclase boundaries. (E) BSE image of an orthopyroxenite clast, with details in the inset (F) BSE image of a dunite clast. The yellow dashed line approximates the portion of the clast that shows evidence of melting and recrystallization due to its proximity to the fusion crust. (G) BSE image of a breccia clast. The yellow dashed line outlines the clast within it that has been modified; inset shows texture in more detail. (H) Impact melt clast with mineral clasts and glassy matrix. The red arrows indicate small vesicles. (I) BSE image of an exogenous clast with Mg-rich orthopyroxene (Mg-opx) and Mg-rich olivine (Mg-ol). Chr – Chromite, FeS – Iron sulfide, Mx – Matrix, Qtz – Quartz, Trd – Tridymite.

3.2.1 Shock effects

Many pyroxene mineral clasts are unmodified, as they display regular extinction and have no indication of any shock effects. Plagioclase clasts range from undulatory extinction to mosaicism. Shock effects include fracturing, mosaicism, and recrystallization amongst studied clasts. Thus, shock effects are variable amongst clasts. The large breccia clast has a melt pocket that contains plagioclase, pyroxene, olivine, and quartz mineral clasts (Fig.3.8A-B). All the plagioclase and silica grains have either completely or partially converted to diaplectic glass. One silica glass clast also has decorated PDFs (Fig. 3.8C) and a pyroxene clast within the melt pocket displays mosaicism. There are two olivine clasts that have been modified due to sulfidization, although there are nearby small olivine grains that did not experience any secondary alteration (Fig. 3.8D). The matrix of the melt pocket is composed of fine-grained pyroxene and plagioclase crystals, set in a basaltic composition cryptocrystalline assemblage (Fig. 3.8E), consistent with recrystallization via shock melting. Small blebs of FeNi and FeS are set within the matrix (Fig. 3.8E). The immediate matrix in contact with Fe-Ni metal surrounding the melt pocket has anhedral plagioclase and pyroxene grains (Fig. 3.8F). Plagioclase in this case has a texture consistent with in-situ melting and mobilization (Fig. 3.8F). Two large exsolved orthopyroxene clasts on either side of the melt pocket exhibit mosaicism and a plagioclase clast near the edge of the melt pocket contains pyroxene inclusions and has been converted to diaplectic glass (Fig. 3.8B).

One of the olivine orthopyroxene clasts with thermally annealed matrix has elongated pyroxene grains that exhibit PDFs and mosaicism (Fig. 3.9A). One large basalt clast has plagioclase that seems to be composed of coarse plagioclase grains in BSE images and under plane-polarized light (Figs. 3.9B-C). However, under cross-polarized light the plagioclase in this clast forms polygonal sub-grain mosaics with distinct boundaries and with twinning in some of the sub-grains (Figs. 3.9D). There are no vesicles or flow lines present within this plagioclase clasts. This clast also displays grain boundary migration between pyroxene and plagioclase (Figs. 3.9B). Another basalt clast also has plagioclase that is composed of coarse plagioclase grain in BSE image and under plane polarized light (Fig. 3.9 E-F). However, under crossed polarized light, majority of the plagioclase is fine-grained. The plagioclase in this clast has PDFs and its boundary with pyroxene is irregular (Fig. 3.9G). The texture in this clast is indicative of grain boundary melting between plagioclase and pyroxene, and recrystallization of plagioclase (Fig. 3.9G). The cumulate eucrite clast contains silica glass that has fractures radiating outwards (Fig. 3.9H). The radiating fractures result from the transformation of silica to diaplectic glass. The clast's groundmass contains incipient pyroxene melt (Fig. 3.9I).

One orthopyroxene clast has exsolution lamellae of high-Ca clinopyroxene and a vein cutting across it that truncates at the clast boundary (Fig. 3.10A). The vein has a width of 10 μm and consists of poorly crystalline pyroxene grading into a zone of glass + granular crystals of pyroxene in the center, with iron-sulfide globules in the glass as well (Fig. 3.10A). Four orthopyroxene mineral clasts have iron-sulfide disseminated throughout the clasts' healed fractures (e.g. Fig. 3.10B). Two ferroan pyroxene mineral clasts have exsolution lamellae of Ca-pyroxene (Fig. 3.10C). These clasts have areas where the exsolution lamellae have been erased by the overprinted pyroxene (Fig. 3.10C-D). This texture is suggestive of recrystallization and likely occurred during shock heating. Single plagioclase and pyroxene clasts were fragmented and contain offset twinning and lamellae pattern (Figs. 3.10E-F). The pattern is suggestive of fragmentation along a dislocation slip during shear deformation of the crystals.

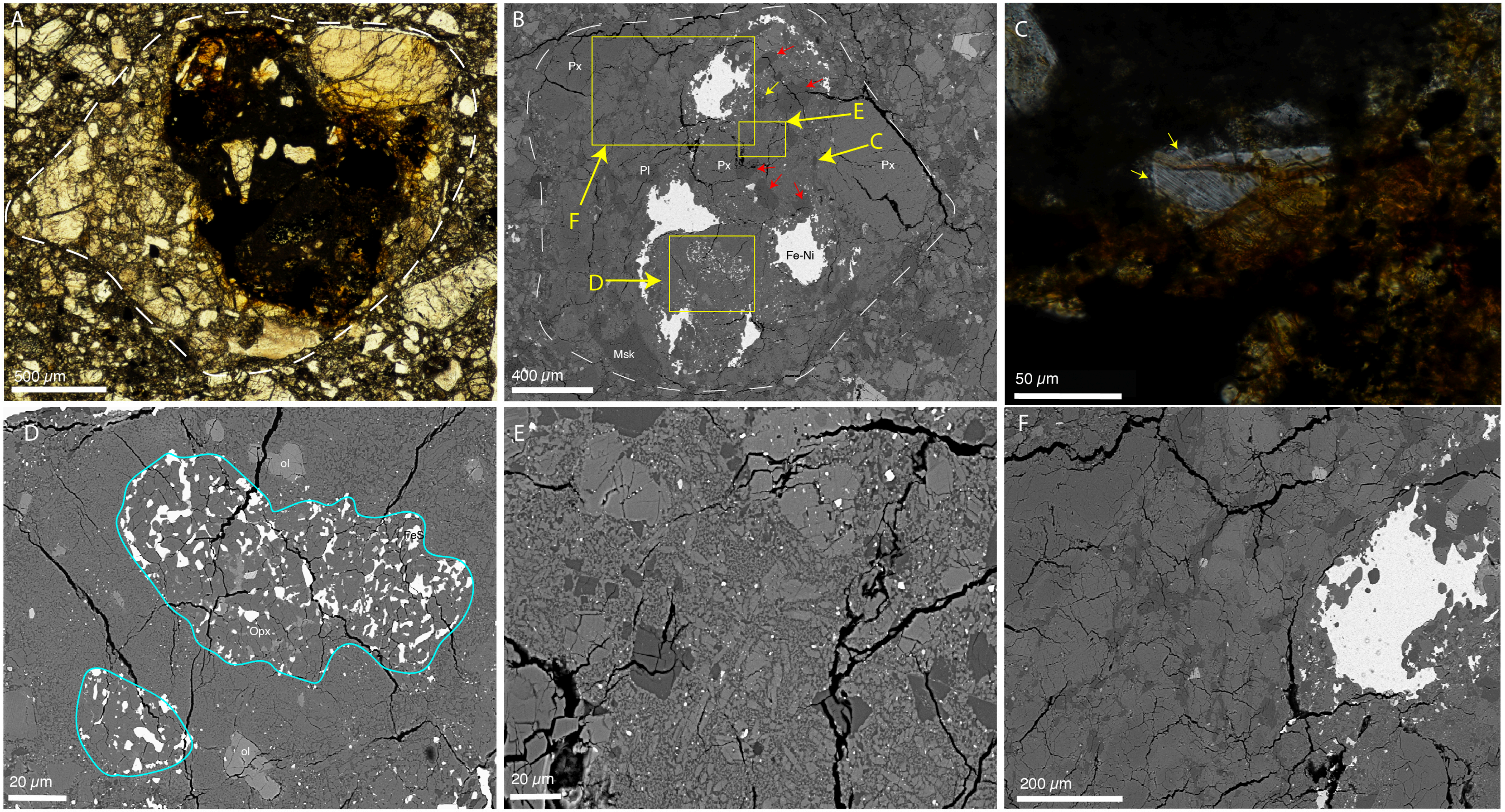

Figure 3.8: Images of a breccia clast in Sariçiçek. (A-B) PPL and BSE images. The yellow and red arrows indicate diaplectic plagioclase and silica glass, respectively, in B. (C) PPL image of the diaplectic silica glass found on the edge of the melt pocket in B, with decorated PDFs indicated by yellow arrows. (D) BSE image of the two olivine clasts that show evidence for conversion to orthopyroxene and iron-sulfide are outlined in cyan. (E) BSE image showing the fine-grained recrystallized matrix of the melt pocket. (F) BSE image of the material surrounding the melt pocket.

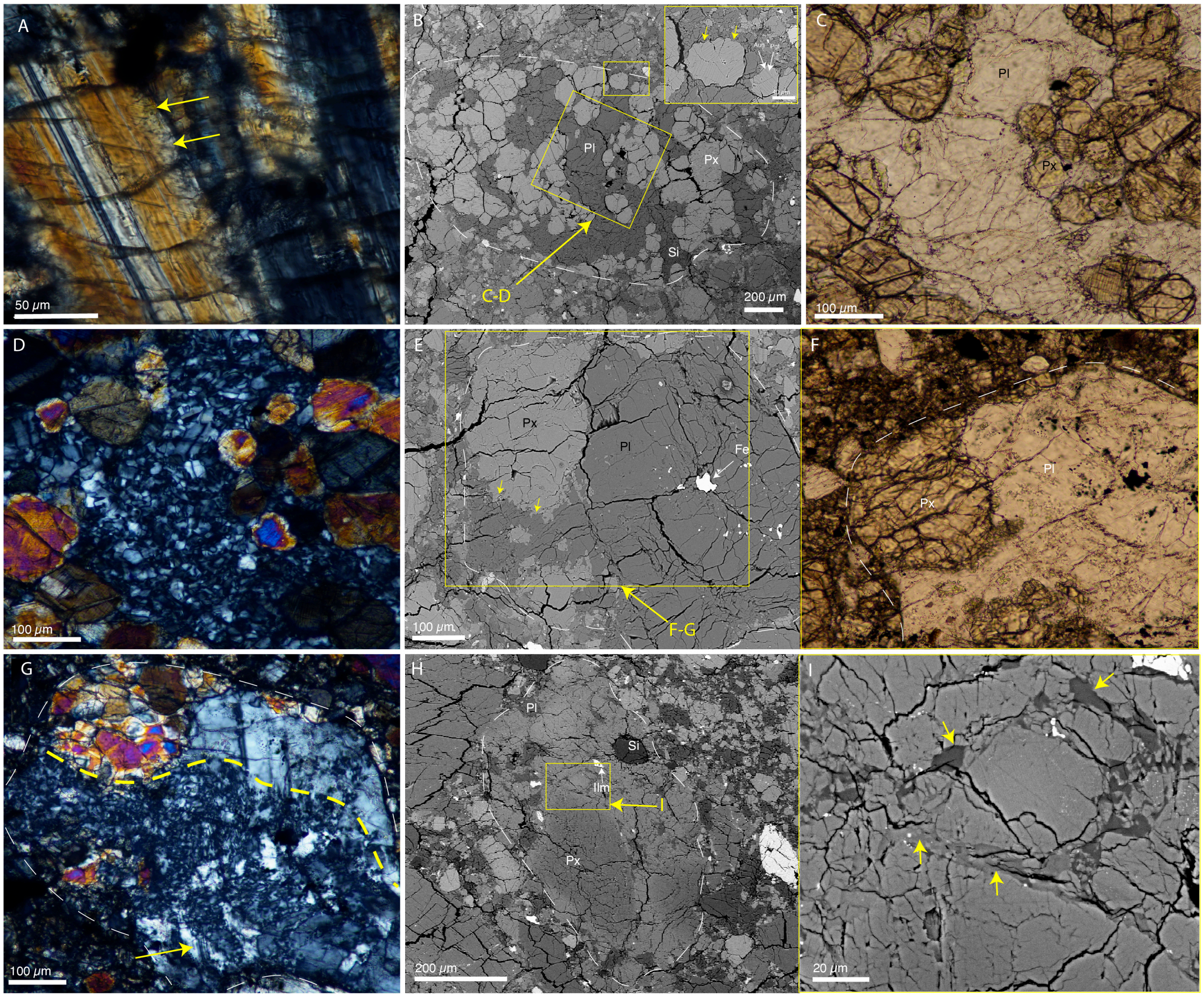

Figure 3.9: Images of shock and thermal metamorphism effects in distinct lithic clasts in Sariçiçek. (A) XPL image of the area in yellow box in Figure 3.7C. The yellow arrows point towards PDFs on the edge of a twinned pyroxene crystal. (B) BSE image of a basalt clast with recrystallized plagioclase. The inset displays grain boundary migration between pyroxene and plagioclase (yellow arrows). (C-D) PPL and XPL images, that show the interstitial plagioclase with sub-grain boundaries is visible in D. (E) BSE image of another basaltic clast with recrystallized plagioclase. (F-G) PPL and XPL images of the basaltic clast in E. The dashed yellow line in G outlines the portion of the plagioclase crystal that has a recrystallized texture, visible in XPL light. (H) BSE image of a cumulate clast. (I) The yellow arrows point towards evidence for incipient pyroxene and plagioclase melting.

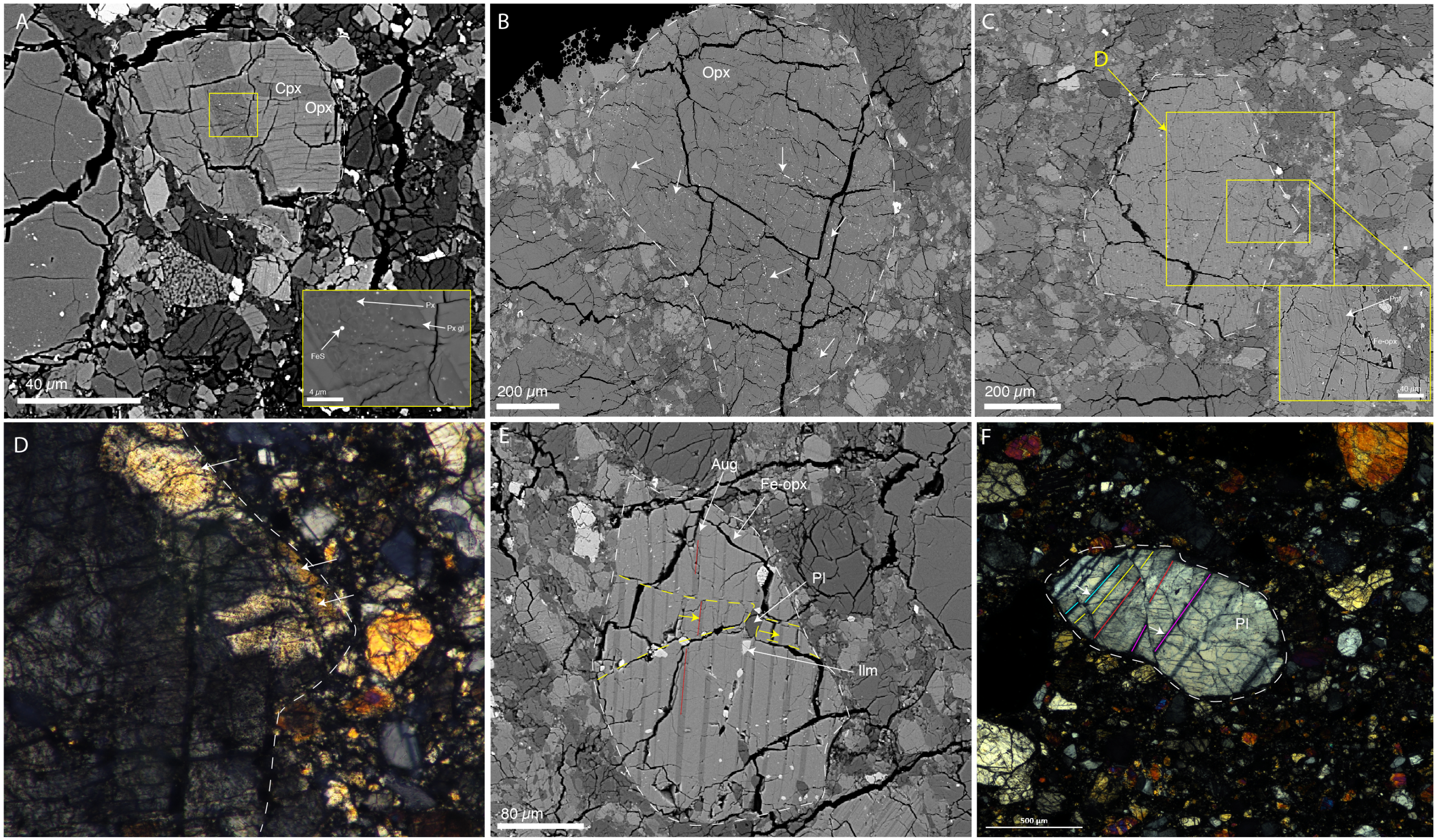

Figure 3.10: Images of individual clasts with distinct shock effects in Sariçiçek. (A) BSE image of an orthopyroxene clast with clinopyroxene lamellae that is crosscut by a shock melt vein. The inset image shows details of the shock melt vein, including pyroxene globules set in pyroxene glass. (B) BSE image of a large orthopyroxene clast decorated by iron-sulfide beads, indicated by the white arrows. (C-D) BSE and XPL image of a ferroan orthopyroxene clast with pigeonite exsolution lamellae. The edge of the clast shows evidence for recrystallization; details are provided in the inset image in C. White arrows point towards recrystallized pyroxene in D. (E-F) BSE image of a pyroxene clast and XPL image of a plagioclase clast. Both clasts in E and F display lamellae and twin offsets.

3.3 NWA 10922

NWA 10922 has abundant mineral, lithic, breccia, and impact-melt clasts, and impact-melt spherules set in fine-grained matrix (Fig. 3.1C). The major minerals are pyroxene ($En_{19.6-67.6}Wo_{2.4-43.2}$) and plagioclase ($An_{3.8-52.9}$). The average size of mineral clasts studied is 0.4 ± 0.5 mm (n=22), lithic clasts is 0.4 ± 0.2 mm (n=13), breccia clasts is 2.1 ± 0.6 mm (n=2), impact-melt clast is 1.6 ± 1.4 mm (n=10), and impact-melt spherules is 2.5 ± 1.5 mm (n=6). Clasts identified in NWA 10922 make up 40% of the total surface area of the sample. Among these are breccia clasts (18%), impact-melt spherule (9%), lithic clasts (8%), and mineral clasts (5%) The inventory of clasts studied in NWA 10922 is summarized in Table 3.3.

Table 3.3: Characteristics of clast types analyzed in NWA 10922 in this study: size range, mineralogy, textures, approximate modal mineralogy, and shock effects.

	Number of Clasts	Range of Size (mm)	Mineralogy and Textures	Range of Approximate Modal Mineralogy	Range of Shock Effects
Lithic Clasts	13				
Norite	3	0.3-0.7	- Subhedral orthopyroxene and plagioclase. One clast has orthopyroxene with augite exsolution lamellae - Poikilitic and granoblastic textures	- 35-59% plagioclase - 30-62% pyroxene - 2-6% Fe-Ti oxides and sulfides - 0-5% phosphates	- Fractured minerals
Basalt	7	0.1-0.6	- Anhedral pyroxene and plagioclase grains - Fine-grained, poikilitic and granoblastic textures	- 29-63% plagioclase - 29-49% pyroxene - 2-13% phosphates - 3-11% Fe-Ti oxides and sulfides	- Fractured minerals
Monzonite	1	0.5	- Alkali feldspar mantled by plagioclase. - Orthopyroxene present only within fractures that are associated with altered iron-sulfides	- 84% plagioclase and alkali feldspar - 4% pyroxene - 4% phosphates - 8% sulfides	- Fractured minerals
Orthopyroxenite	1	0.4	- Subhedral coarse orthopyroxene grains associated with opaque minerals and some plagioclase. - Granoblastic texture	- 5% plagioclase - 84% orthopyroxene - 13% magnetite	- Fractured minerals
Impact-melt clasts	10	0.5-4.5	- Clast shape varies in angular, rounded, oval, and irregular. - Pyroxene, plagioclase, disseminated oxides ± phosphates. - Most clasts contain pyroxene clumps.		

			- Some clasts have a crystalline basaltic composition matrix with subophitic texture. - Some clasts have matrix composed of likely amorphous material that has partially recrystallized in pyroxene and plagioclase.	
Breccia clasts	2	1.3-3.0	- One clast is composed of alkali feldspar brecciated with pyroxene and phosphate clast. The clast's matrix is like the bulk breccia matrix but coarser. This clast also displays layering of grains. - The second breccia clast is composed of plagioclase and pyroxene grains set in porous and fine-grained pyroxene matrix	- Fractured minerals - One clast has sintered and recrystallized grain boundaries
Impact-melt spherules	6	0.2-1.7	- Pyroxene, plagioclase, oxides, ± phosphates - Quenched, devitrified, and fine-grained textures. - Most spherules contain pyroxene clumps	
Mon-mineral clasts			-	
Feldspar	6	0.3-0.8	- Ca-Na rich plagioclase clasts. - Antiperthitic clasts (Na-plagioclase host with K-feldspar exsolution lamellae)	- Fractured minerals
Pyroxene	8	0.3-2.4	- Clasts with Fe-rich host with Mg-rich exsolution lamellae - Clinopyroxene clasts	- Fractured minerals

	- Orthopyroxene clast with high-Ca pyroxene exsolution lamellae - One large orthopyroxene clast has Fe-oxide and plagioclase filling fractures	- One clast has a sintered and recrystallized edge.

Lithic clasts in NWA 10922 are dominated by basalt, followed by norite, orthopyroxenite, and monzonite (Fig. 3.11A-C). Opaque minerals in all lithic clasts consist of Fe-Ti-Cr oxides, and sulfides that have been altered to Fe-oxyhydroxides. Basalt clasts vary the most in textures that include fine-grained pyroxene and plagioclase assemblages with pyroxene and plagioclase xenoliths, granoblastic with triple junctions between silicate grains, and ophitic to sub-ophitic texture (Fig. 3.11A). Only one monzonite clast and one orthopyroxenite clast was identified in this sample (Fig. 3.11C and 3.12A, respectively). The monzonite clast has pervasive fractures that are filled with a fine-grained phase (Fig. 3.12). Plagioclase was modified to the same phase along the fractures. The EDS composition in wt% of the modification product is 20.98 MgO, 3.64 Al_2O_3, 49.29 SiO_2, 7.92 CaO, 0.45 TiO_2, 0.64 MnO, and 16.85 FeO. The Raman spectrum of the modification product has low intensity and broad shifts confirming that it's a fine-grained aggregate material. The spectra have a consistent Raman peak that ranges from 663 to 678 cm^{-1} (Fig. 3.12B). Less intense and broad shifts are present at 314 cm^{-1}, 333 cm^{-1}, 509 cm^{-1}, and 1013 cm^{-1} (Fig. 3.12B).

Impact melt clasts in NWA 10922 resemble fine-grained clast-laden melt particles described by Hewins et al. (2017) and impact-melt rocks described by Wittmann et al. (2015). In NWA 10922, the impact-melt clasts are Ca-rich, vary in shape and size, and contain pyroxene, plagioclase, disseminated oxides ± phosphates (Fig. 3.13A-B). Two clasts are elongated and irregularly shaped (Fig. 3.13B-C). Some clasts also contain aggregates of pyroxene mantled by a plagioclase aureole (Fig. 3.13D). The matrix of some of the clasts is composed of crystalline basaltic composition matrix (Fig. 3.13E). Other impact melt clasts have matrix that is composed of likely amorphous material with irregularly distributed iron-oxides throughout the clast.

Breccia clasts are called protobreccias by McCubbin et al. (2016) and Santos et al. (2017) and they define these clasts as having similar textures and mineralogy as the bulk breccia, except the matrix of protobreccia clasts that have coarser grains and variable amounts of Fe-Ti oxides. To remain consistent with the characterization of clasts in NWA 14340 and Sariçiçek, all protobreccia clasts are referred to as breccia clasts for NWA 10922. Two breccia clasts were identified; one of them is a large clast composed of subhedral to anhedral grains of plagioclase feldspar, clinopyroxene, and apatite, surrounded by a fine-grained matrix that is poorly sorted (Fig. 3.13F). Fe-oxides are present in fractures throughout every mineral phase and in the matrix of the clasts (Figs. 3.13F-G). Additionally, the pyroxene grains were locally decomposed to magnetite and silica. Pyroxene grains are broken along fractures and grain boundaries. Half of the pyroxene in the clast apparently has been modified to a fine-grained aggregate of pyroxene, Fe-oxides, and plagioclase (Fig. 3.13G). The plagioclase grains have fractures filled with Mg-Fe rich silicate material that is similar to the modification product present in the monzonitic clast (Fig. 3.13G and Fig. 3.12, respectively). The clast displays horizontal layering, and the center is composed of a layer of Fe-Ti oxides and sulfides that have been altered to Fe-oxyhydroxides (Fig. 3.13F). The outline of the clast is easily distinguished in the Mg elemental map, as the entire clast is depleted in Mg relative to the bulk breccia (Fig. 3.13F).

Another breccia clast identified in this study is similar to a porous clast identified by MacArthur et al. (2019) and is composed of an elongated crystal of plagioclase feldspar, clinopyroxene and orthopyroxene clasts, a euhedral Fe-sulfide grain, ilmenite, and a cluster of Fe-oxides set in a porous matrix of clinopyroxene and Fe-oxide grains (Figs. 3.13H-I). Pyroxene clasts within the breccia have a texture consistent with local decomposition to magnetite and silica (Fig. 3.13H). The matrix of this clast also contains small grains of Mn-oxides consisting of fibrous and massive forms (Fig. 3.13I), similar to grains of Mn-oxides identified by Liu et al. (2021) in various lithological contexts. The two breccia clasts identified in NWA 10922 are surrounded by fine-grained rims.

In NWA 10922, impact-melt spherules are distinguished by their higher Ca and Fe in elemental maps, with one of the largest impact-melt spherules showing concentric chemical zoning (Fig. 3.13A). This spherule has a Mg-rich core, surrounded by an Fe-rich layer, and then a Ca-rich outer layer. The spherule is composed of crystallites of pyroxene and plagioclase (Fig. 3.13J). The spherule contains abundant iron oxide veins that truncate before the clast boundary, rounded plagioclase masses, pyroxene clumps, pyroxene clasts that have locally decomposed to form magnetite and silica, and sulfide grains (Fig. 3.13J). The outermost layer of this spherule has a diffuse interface with the matrix of NWA 10922 (Fig. 3.13J). The second largest spherule also has a concentric chemical zoning. This spherule contains plagioclase and iron-oxide veins in a fine variolitic pyroxene and iron-oxide matrix. Other smaller impact-melt spherules include 1. sulfide cores, now modified to Fe-oxyhydroxides, surrounded by a fine-grained intergrowth of oxides, pyroxene, and plagioclase 2. Clasts with plagioclase, pyroxene and iron-oxides in a devitrified or radial cryptocrystalline texture.

Mono-minerallic clasts are made up of pyroxene, feldspar, phosphates, Fe-Ti-Cr oxide clasts, and sulfides. Pyroxene clasts are present as orthopyroxene (some have exsolution lamellae of augite), ferroan pyroxene, and high-Ca clinopyroxene (some have exsolution lamellae of orthopyroxene). Few pyroxene mineral clasts in the matrix have locally decomposed to magnetite and silica, that decorate the clast like a trail of fluid inclusions (Fig. 3.14A). Two pyroxene clasts have irregular shapes and are composed of an assemblage of pyroxene and magnetite (e.g., Fig. 3.14B). One of these clasts is angular in shape and has a euhedral FeS crystal in the core. Both clasts have fractures intruding in the clast from edges that are filled with plagioclase feldspar ± Fe-oxide (Fig. 3.14B). One large orthopyroxene clast has corroded edges and a euhedral chromite inclusion. The clast has fractures filled with plagioclase that are cross-cut by Fe-oxides, which are further cross-cut by calcite.

Feldspar mineral clasts include antiperthitic clasts with micropores and plagioclase feldspar clasts. One plagioclase clast is enriched in Ca near the rim and rich in Na and K near the core. The clast has a sulfide vein that has been altered to Fe oxyhydroxides (Fig. 3.14C). Phosphate mono-mineral clasts are not as large as pyroxene or feldspar, and they are all composed of chlorapatite (Fig. 3.14D). Fe-Ti-Cr oxide clasts all have reaction rims, some of them are also zoned with a Mg rich core (Fig. 3.14E).

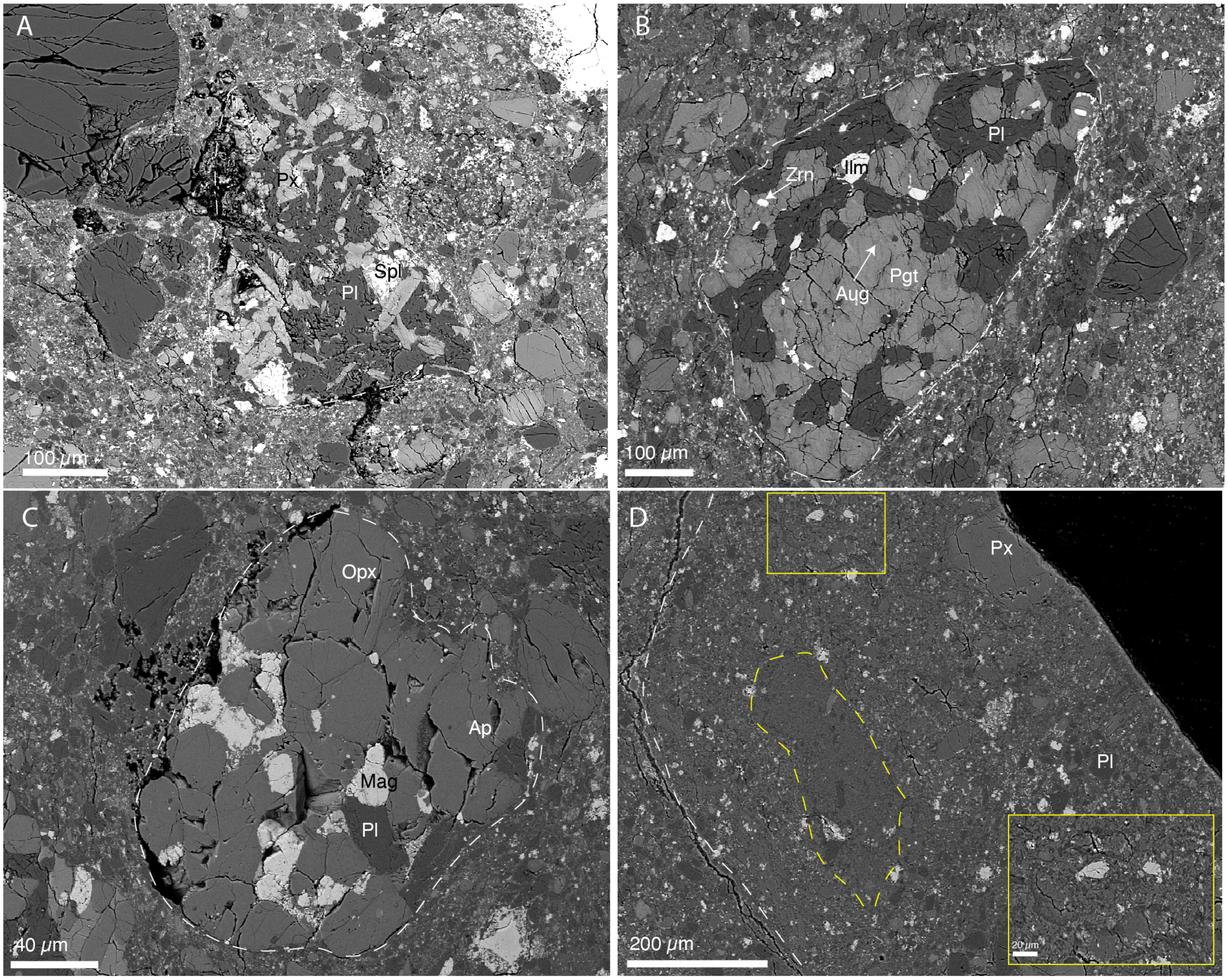

Figure 3.11: BSE mages of lithic clasts and impact melt clasts in NWA 10922. (A) A basalt clast. (B) A norite clast. (C) An orthopyroxenite clast. (D) An impact melt clast. An impact melt clast within this clast is outlined in yellow dashed line. The zoomed in inset image displays the crystalline matrix of the impact melt clast and an irregularly shaped pyroxene clump surrounded by plagioclase aureole. Ap – Apatite, Aug – Augite, Mag – Magnetite, Pgt – Pigeonite, Spl – Spinel, and Zrn – Zircon

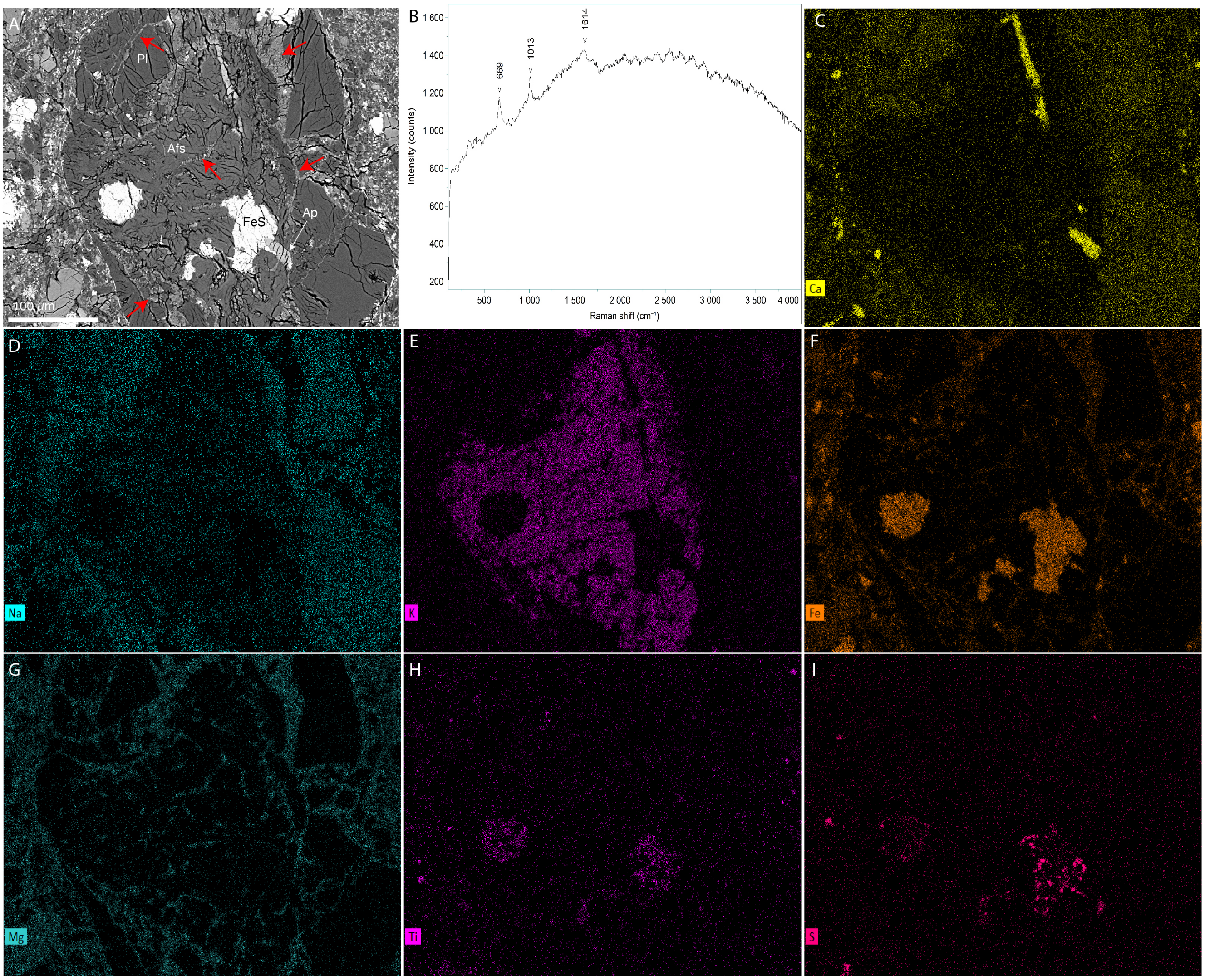

Figure 3.12: Details of a monzonite clast in NWA 10922. (A) BSE image of the monzonite clast. The red arrows point towards fracture filling Mg-Fe silicate material (B) Raman spectrum of the fracture filled material (C-I) EDS maps of the clast.

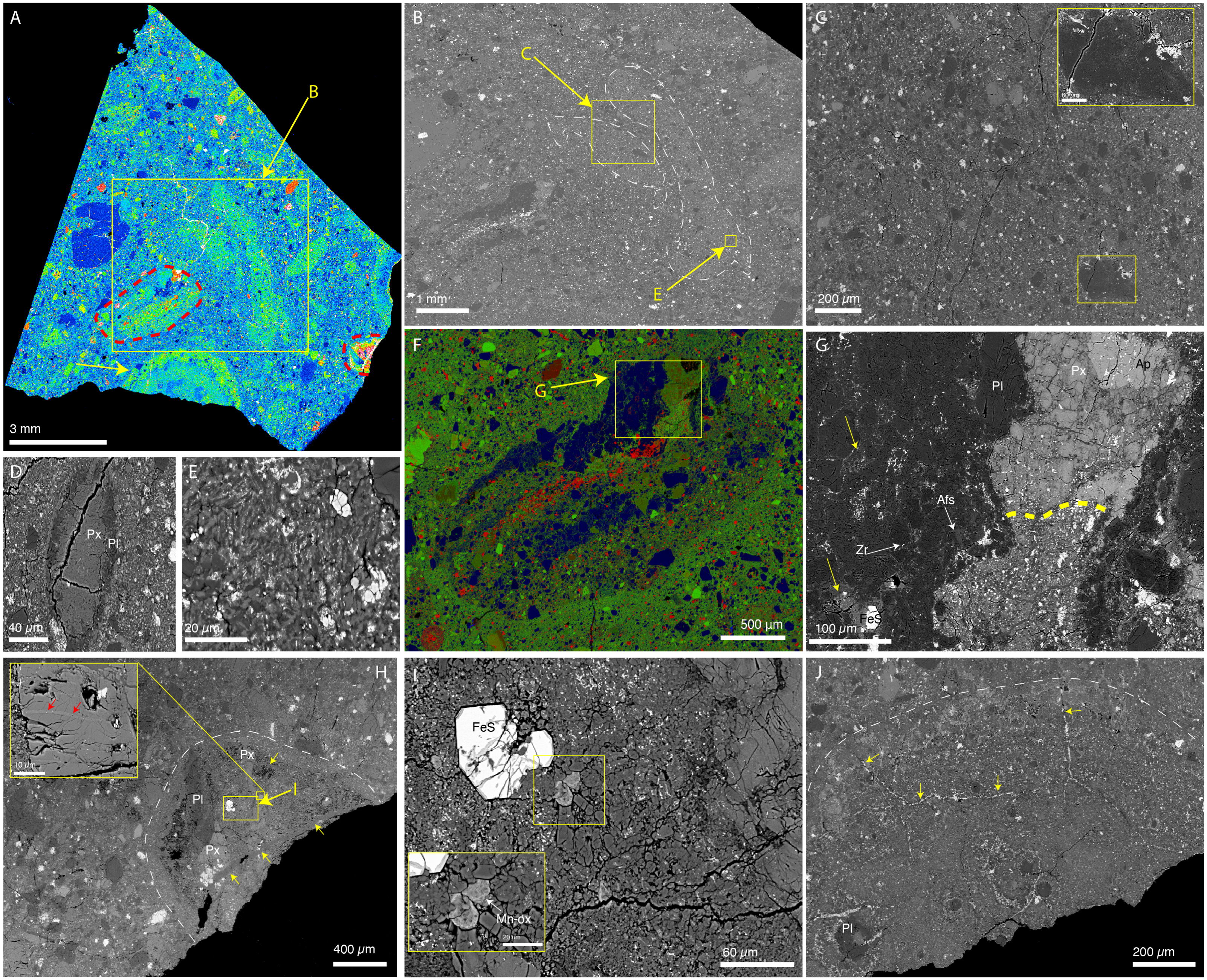
A
B
3 mm
C
E
1 mm
200 μm
D
Px
Pl
40 μm
20 μm
F
G
500 μm
Pl
Px
Ap
Afs
Zr
FeS
100 μm
H
I
10 μm
400 μm
FeS
Mn-ox
60 μm
J
200 μm

Figure 3.13: Details of impact-melt and breccia clasts in NWA 10922. (A) Ca elemental map of NWA 10922. Ca-enriched areas are impact-melt and breccia clasts. The two large breccia clasts are outlined in red dashed lines. (B) BSE image of two irregularly shaped impact melt clasts are outlined in white dashed lines. (C) BSE image of the area in the yellow box in B. D) BSE image of the pyroxene clump from the larger impact melt clast in B, composed of a pyroxene core with variable amounts of Fe-oxides and surrounded by plagioclase. (E) Crystalline matrix of the impact melt clast in B, composed of pyroxene, plagioclase, and Fe-oxides. (F) RGB elemental map of one of the breccia clasts outlined in red in A, where R-G-B = Fe-Mg-Al. (G) BSE image of the area in the yellow box in F, showing plagioclase and pyroxene breakdown textures and the zig-zag interface between the two minerals. The dashed yellow line separates the pyroxene still intact from completely broken-down pyroxene. Around iron-sulfide and within plagioclase cracks and fractures are pyroxene and magnetite assemblages. (H) BSE image of the second large breccia clast outlined in the yellow dashed line in A. The zoomed in inset shows small magnetite and silica decomposition product in pyroxene (I) BSE image of the yellow box in H, showing the matrix of the clast composed of pyroxene and Fe-oxide grains, and the high pore space between grains. Inset image shows an iron-sulfide mineral clast that has been altered near fractures. Small Mn-oxide grains are also found within the matrix (inset image). (J) BSE image of a large spherule (indicated by the yellow arrow in A) that has devitrified to a crystalline texture. It contains pyroxene clumps but also masses of rounded plagioclase throughout the clast. The yellow arrows indicate Fe-oxide veins that truncate before clast boundary.

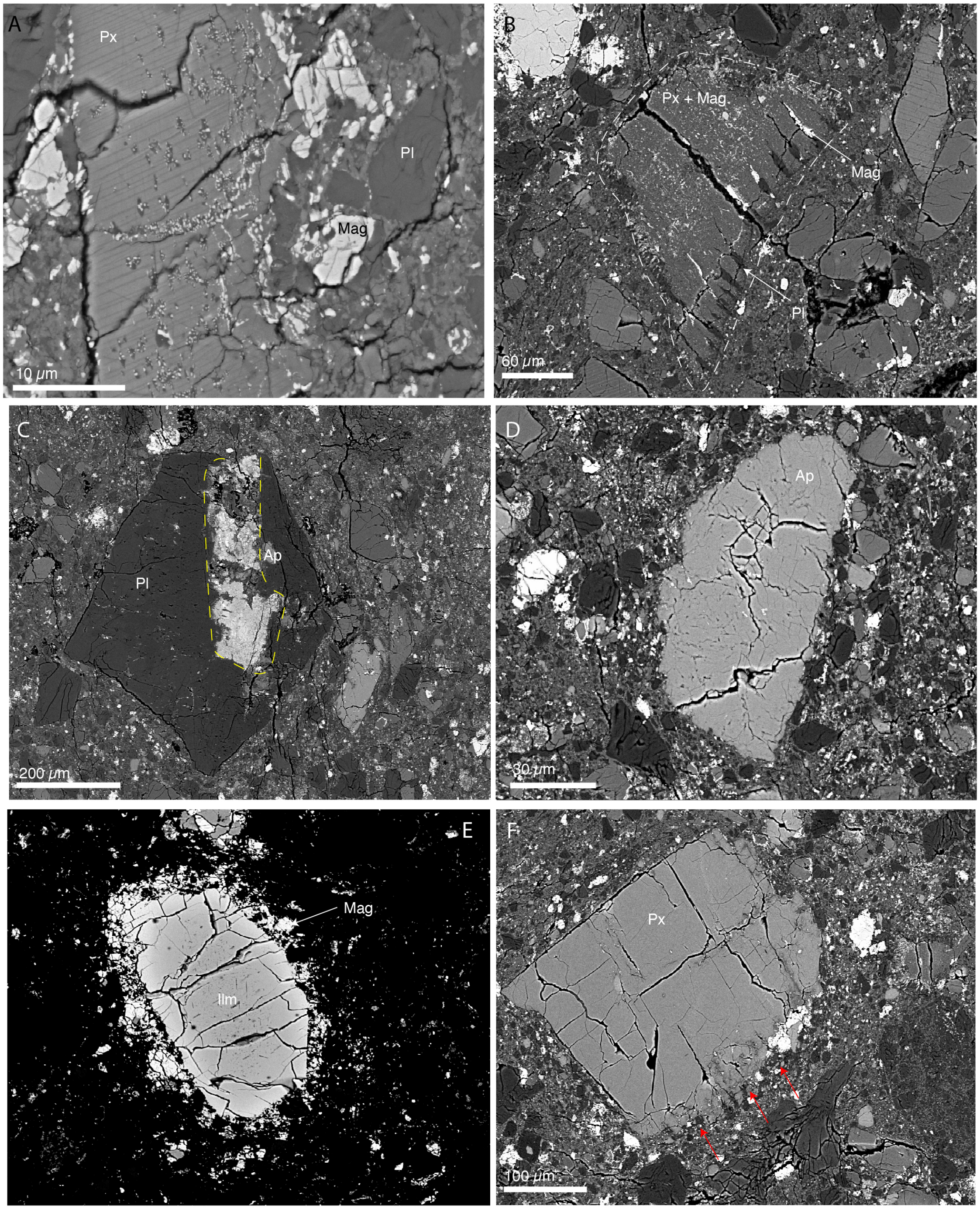

Figure 3.14 BSE images of mineral clasts in clasts in NWA 10922. (A) A pyroxene clast that has locally decomposed to magnetite and silica (B) A clast composed of pyroxene and Fe-oxides, with fractures along its lower margin; fractures are filled with plagioclase and Fe-oxides. (B) A plagioclase clast with micropores, crosscut by a sulfide vein (outlined in yellow dashed line) that has been altered to Fe-oxyhydroxides. (C) An apatite mineral clast. (D) A zoned ilmenite mineral clast surrounded by magnetite, interpreted to be a reaction product of the ilmenite with the matrix. (E) A pyroxene clast with a sintered and recrystallized edge (red arrows) composed of plagioclase, Fe-oxides and pyroxene.

3.3.1 Shock effects

Shock effects in all lithic clasts are limited to fracturing only. The large protobreccia clast has zig-zag interface between feldspar and pyroxene that has likely resulted from sintering and recrystallization (Fig. 3.13G). Similarly, one pyroxene mineral clast has a sintered edge that has recrystallized to pyroxene, Fe-oxide, and plagioclase (Fig 3.14F).

Chapter 4: Results – Characterization of the Matrix in NWA 14340, Sariçiçek, and NWA 10922

4.1 NWA 14340

The matrix in NWA 14340 is composed of plagioclase, pyroxene and olivine, and minor silica (quartz, tridymite, and moganite), ilmenite, troilite, FeNi metal and accessory zircon, all set in a fine-grained to glassy material (Fig. 4.2A). Minerals in the matrix are subrounded to subangular and range in size from < 10 μm to up to 250 μm, with embayed and corroded edges (Figs. 4.1A-C). Plagioclase mineral clasts are Ca-rich and vary in size from 50-250 μm. Pyroxene and olivine mineral clasts are typically smaller. Most orthopyroxene mineral clasts contain augite exsolution lamellae. Olivine mineral clasts vary in Mg and Fe content based on their EDS compositions and Raman spectra. Few olivine clasts in the matrix appear to have decomposed to amorphous material. The nature of the amorphous material could not be determined via Raman spectroscopy or FESEM. Additionally, abundant glass and impact melt particles are found within the matrix (Fig. 4.1C). The boundary between matrix and lithic clasts is ambiguous as both lithic clasts and matrix materials are rich in calcic plagioclase. Many lithic and mineral clasts exhibit small vesicles along their edges. These clasts are also heavily fractured but are relatively smoother with fewer fractures near their rims. (Fig. 4.1D). This texture suggests that the edges of the clasts underwent either partial melting or thermal annealing, and recrystallized with the matrix, resulting in a diffuse or irregular matrix-clast boundary.

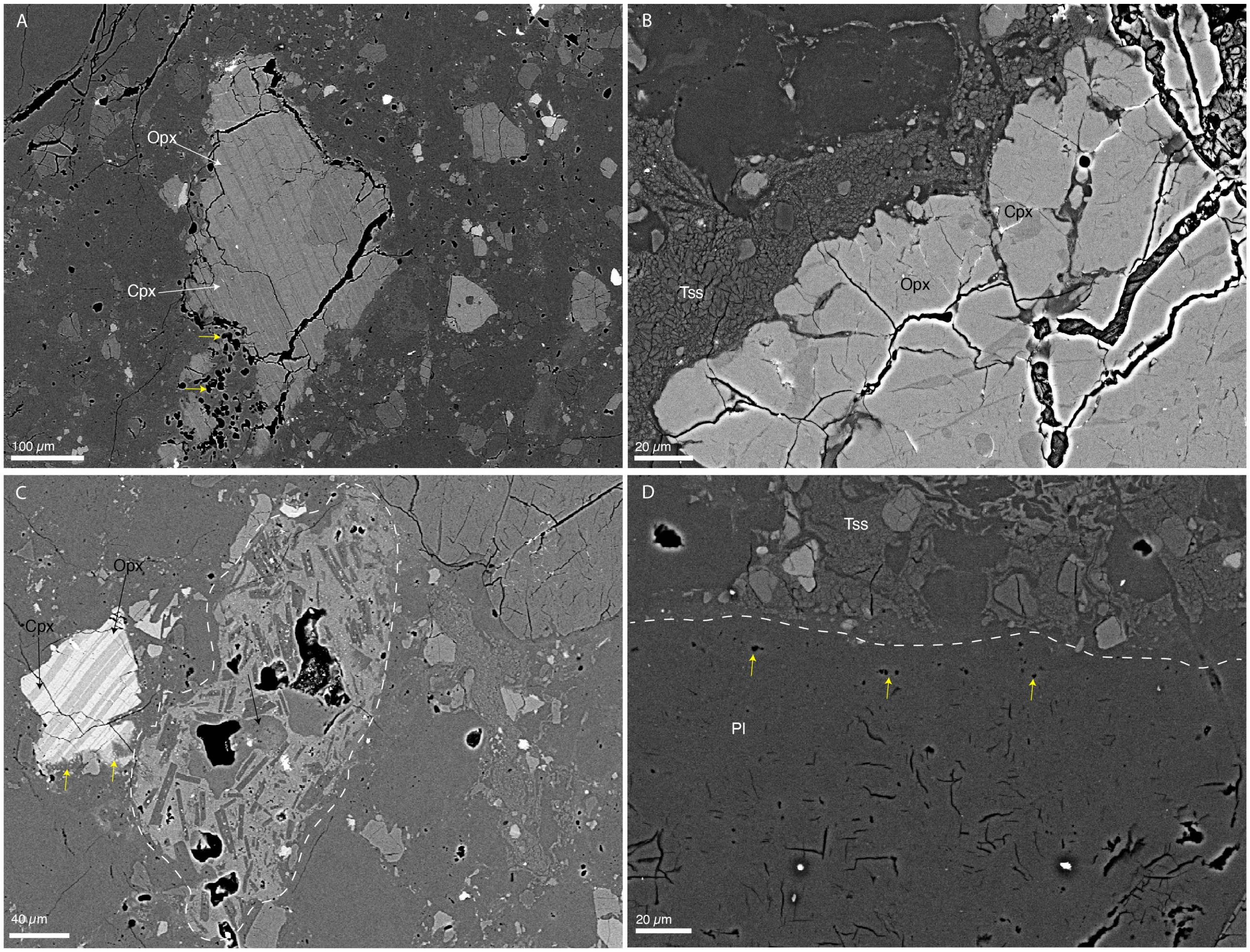

Figure 4.1: Backscatter Electron (BSE) images of minerals and textures in the matrix of NWA 14340. (A) Orthopyroxene (Opx) mineral clast with exsolution lamellae of clinopyroxene (Cpx). The clast appears to have had bits broken off from its bottom edge. Several vesicles in this area are indicated by the yellow arrows. (B) An orthopyroxene clast with embayed edge, along which a cluster of tissintite (Tss) is present. (C) An impact melt clast and another orthopyroxene clast with bent clinopyroxene exsolution lamellae in the matrix. Yellow arrows point towards the pyroxene clast's fragmented bottom edge. (D) Yellow arrows point towards small vesicles found within a plagioclase clast along its boundary.

4.1.1 *Shock effects*

Plagioclase mineral clasts in the matrix display patchy undulose extinction and PDFs like plagioclase in all the lithic clasts (Fig. 3.3). Some plagioclase mineral clasts in the matrix have transformed to maskelynite. Pyroxene mineral clasts display undulose extinction to weak mosaicism. No shock effects were observed in olivine clasts. The matrix has mineral clasts set in fine-grained to glassy material. The Raman spectra indicate glass of either plagioclase or plagioclase + olivine composition (Figs. 4.2B-D).

There are large glassy areas within the matrix and throughout the sample that are characterised by flow lines, large vesicles, and clasts with intensely embayed and corroded edges (Figs. 4.3A-F). Pyroxene mineral clasts in glassy areas exhibit mosaicism and have been plastically deformed as evidenced by lamellae that are typically bent and offset along a dislocation slip (Fig. 4.3B-C). Mineral clasts composed of variable amounts of quartz, tridymite ± moganite in the interior regions of the glassy regions have transformed to silica glass and coesite (Fig. 4.3F). Clusters of elongated and fine-grained crystals (average size of ~ 2 μm) are widespread in the matrix of NWA 14340 (Fig. 4.4A-B and D-F). These clusters are present along the boundaries of large glassy regions, along mineral clast boundaries within the glassy regions, and in the glass at the boundaries between lithic clasts and matrix (Fig. 4.4A-B and D-F). The EDS compositions of these fine-grained crystals are like plagioclase with an additional 5 wt% MgO and 4 wt% FeO. The Raman spectrum of these crystals (Fig. 4.4C), coupled with their EDS compositions, confirms their identity as the high-pressure polymorph of plagioclase feldspar known as tissintite (Ma et al. 2015). Tissintite clusters are often present in a flow-shaped form, confirming that the clusters crystallized from melt that was mobilized within the sample (Figs. 4.4D). The high MgO and FeO composition, along with their crystallization from melt rather than solid-state transformation from maskelynite, which has been observed in martian meteorites

(Walton et al. 2014, Ma et al. 2015) characterize these crystals as tissintite-II (Zhang et al. 2021). For simplicity, it will just be referred to as tissinttie from here on.

Within some of the tissintite clusters, along lithic clast boundaries and in large glassy regions, there are aggregates of even smaller and finer-grained microlites (average size of ~ 1 µm) that are stubby to elongated (Figs. 4.5A-B and D). These crystals are not as widespread as tissintite in the matrix of NWA 14340 (Fig. 4.5F) and are too fine-grained for meaningful EPMA or EDS analysis. The EDS maps display no difference between these crystals and tissintite, although their compositional differences are evident from different grayscale in BSE images. These crystals likely contain higher MgO and FeO than tissintite. The Raman spectrum acquired from these crystals confirms their identification as garnet (Fig. 4.5C; Mingsheng et al. 1994). Raman spectrum acquired from garnet and tissintite bearing glass is consistent with glass composition of plagioclase and tissintite (Fig. 4.5D). In some regions, garnet is accompanied with small olivine rounded mineral clasts in the tissintite cluster, sometimes with a reaction rim (Fig. 4.5E).

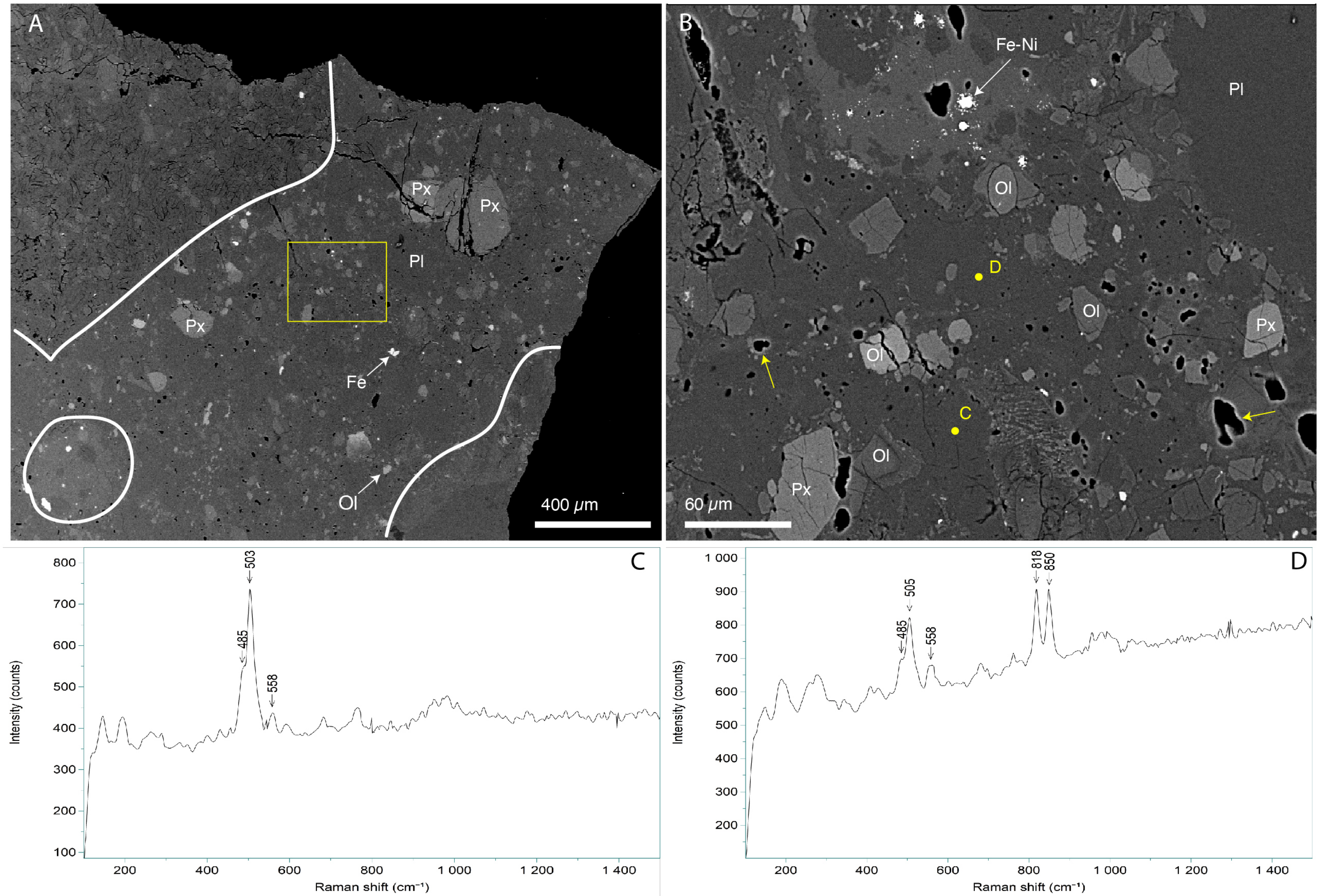

Figure 4.2: Images of the matrix of NWA 14340 and Raman spectra acquired from the matrix (A-B) BSE images showing matrix between lithic clasts and a spherule. Yellow arrows indicate vesicles within the matrix in B. (C-D) Raman spectra acquired from yellow spots within glassy regions in B.

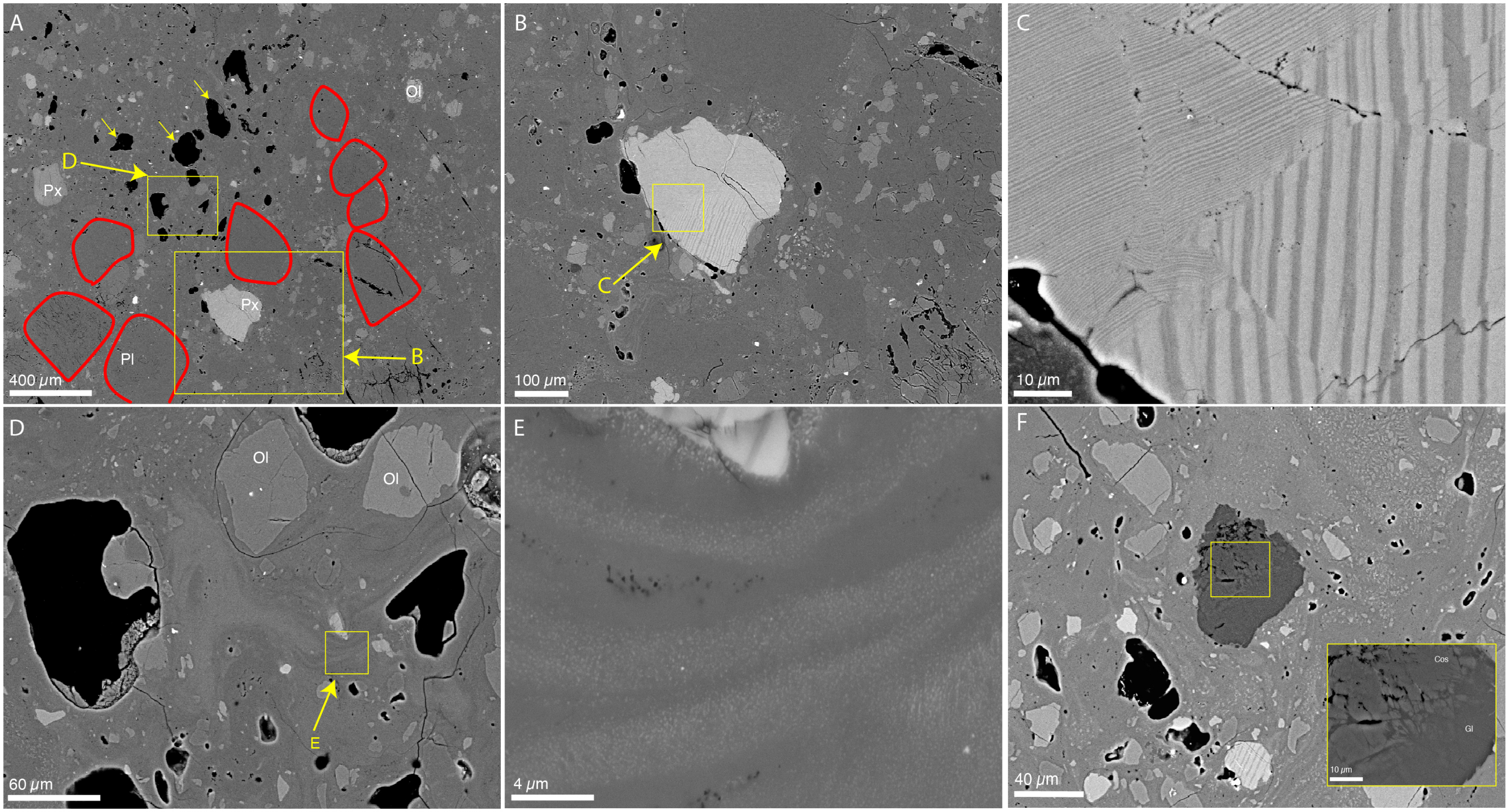

Figure 4.3: BSE images of a glassy area in the matrix of NWA 14340, interpreted as a shock melt pocket. (A) Plagioclase mineral clasts are outlined in red. Yellow arrows indicate large vesicles in the melt pocket. (B) A large orthopyroxene clast with vesicles along its embayed edges and contains thin exsolution lamellae. (C) Two sets of lamellae along different orientations are bent and offset. (D-E) Mineral clasts that are subangular and large vesicles along with flow lines. Inset image show flow lines marked by submicron microlites in E. (F) A clast with silica glass and coesite entrained within a glassy region.

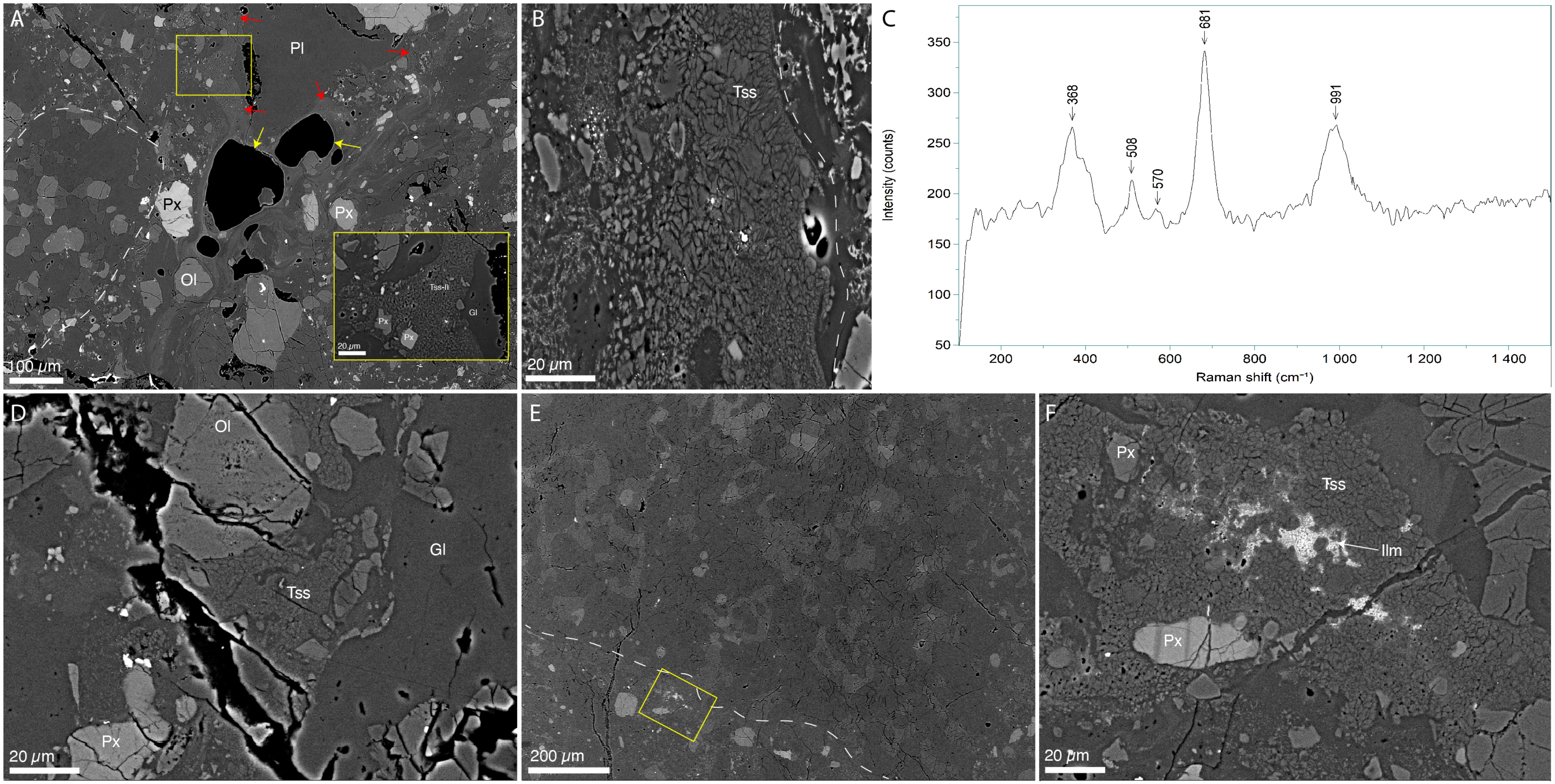

Figure 4.4: BSE images and Raman spectrum of tissintite within the matrix of NWA 14340. (A) A melt pocket that contains clusters of tissintite crystals along its edges. Tissintite clusters include pyroxene clasts entrained within. (B) A tissintite cluster along the edge of the lithic clast in Fig. 3.6C, outlined by the white dashed line. (C) Raman spectrum of tissintite. (D) Tissintite cluster in a flow-shaped form. (E) Tissintite cluster along the edge of a lithic clast (outlined in yellow dashed line). (F) The cluster contains small crystals of ilmenite near the center, interpreted to have crystallized during formation of the melt pocket. Gl – Glass and Tss – Tissintite.

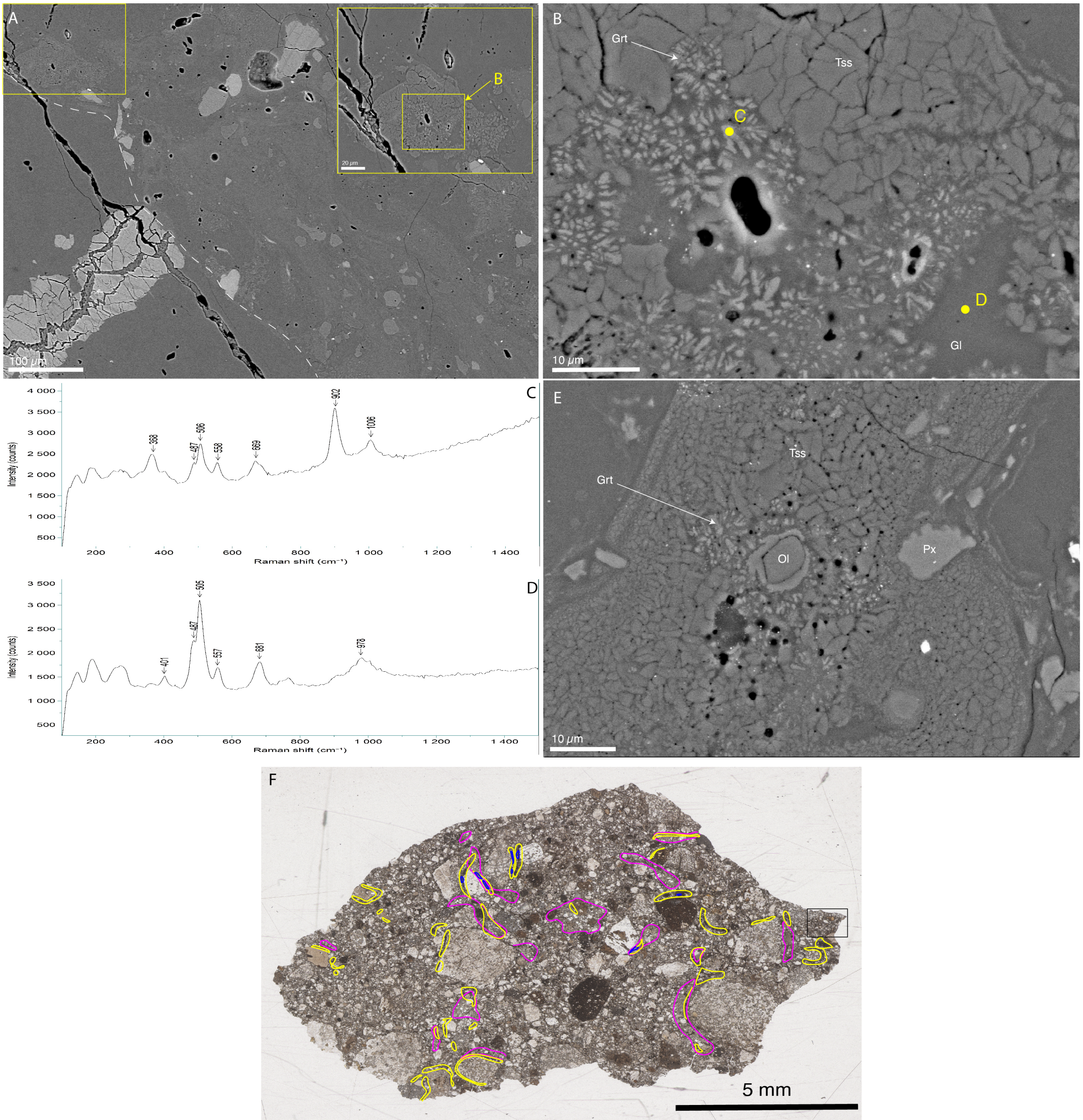

Figure 4.5: BSE images and Raman spectrum of garnet within the matrix of NWA 14340. (A) Tissintite cluster along a lithic clast's edge, outlined in the white dashed line. (B) Garnet (Grt) microlites embedded in plagioclase glass and in the center of the tissintite assemblage. (C-D) Raman spectra acquired from the small garnet crystals and glass. Garnet has characteristic Raman peaks at 364.52 cm^{-1} and 902.54 cm^{-1} in C. (E) Image of garnet crystals in the tissintite cluster, surrounding an olivine clast with a reaction rim. (F) Areas outlined in yellow contain tissintite, pink contain melt with large vesicles and flow lines, and blue contain garnet in the TL scan of NWA 14340. Grt - Garnet

4.2 Sariçiçek

Matrix in Sariçiçek is composed largely of fragments of plagioclase and pyroxene mineral clasts, with some tridymite and quartz, and minor minerals that include olivine, chromite, ilmenite, iron-sulfides, and Fe-Ni metal. Mineral clasts in the matrix range in size from ~10 μm to 50 μm and are angular to subangular in shape (Figs. 4.6A-B). Pyroxene clasts in the matrix are composed of ferroan orthopyroxene with augite exsolution lamellae (Fig. 4.6D), and orthopyroxene. Many pyroxene mineral clasts contain chromite rods that cut across the host crystal and lamellae (Fig. 4.6D). Plagioclase clasts in the matrix are calcium rich, and some contain albite twins.

The matrix exhibits a size distribution typical of a seriate texture, with certain portions so fine-grained that they appear opaque in the optical microscope under PPL. The sub-micron sized material is composed of pyroxene and plagioclase and conforms to the grooves along the edges of clasts (Fig. 4.6C). This submicron material likely has a history of thermal annealing and recrystallization. Abundant glassy particles and impact melt particles that range in size from < 10 μm to ~ 50 μm, with devitrified and fine-grained recrystallized textures are also found throughout the matrix (Figs. 4.6D-F). Numerous mineral clasts in the matrix are fused together, establishing direct points of contact along their edges (Figs. 4.7A-F). Numerous mineral clasts also have rough edges, and/or conform to the surrounding material (Fig. 4.7A and 4.8A-B).

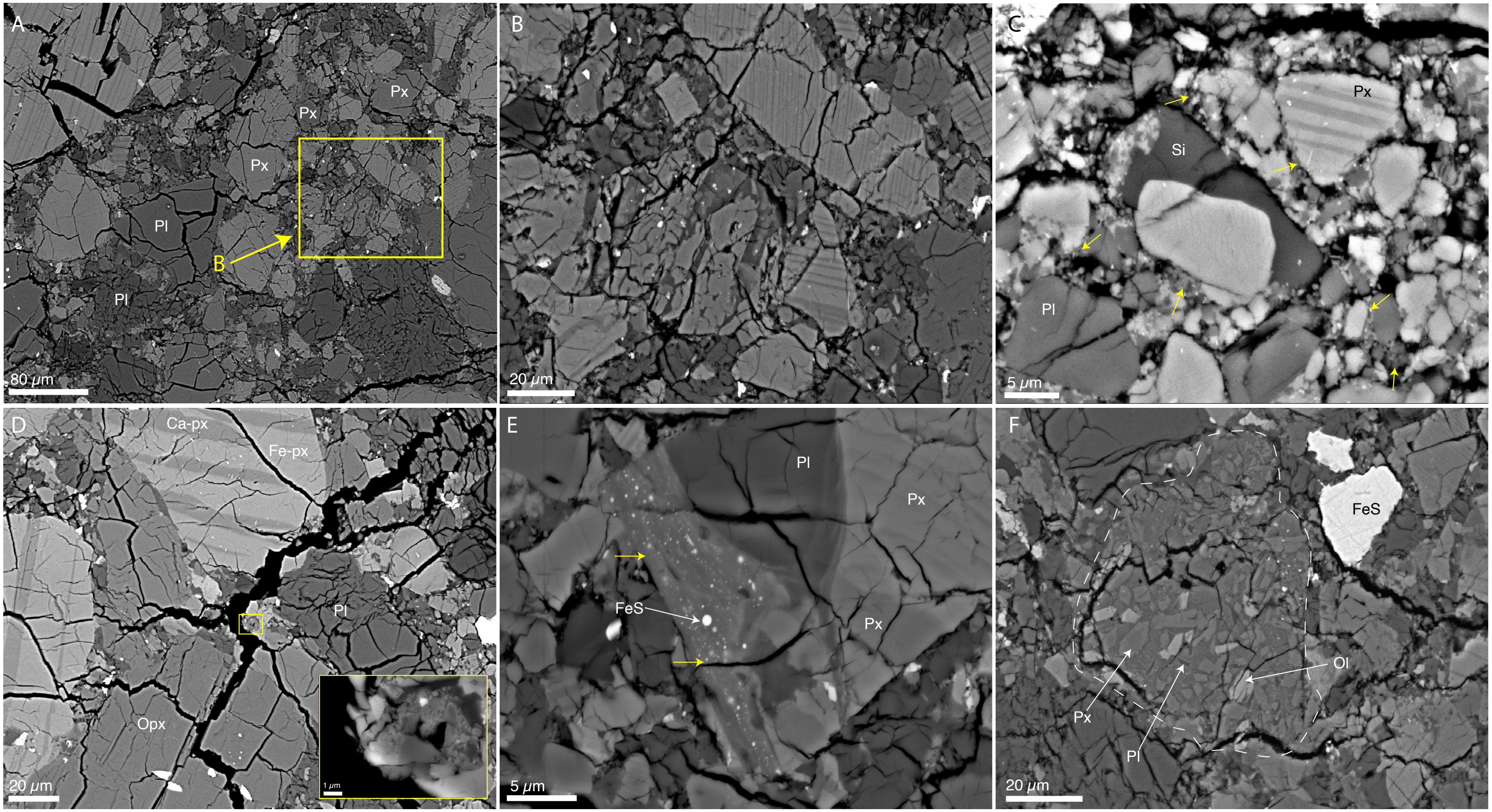

Figure 4.6: BSE images of the matrix of Sariçiçek. (A) An area of the matrix with angular to subangular mineral clasts. (B) Matrix has a finer-grained component that surrounds larger angular to subangular mineral clasts. (C) Extremely fine-grained and submicron matrix material indicated by the yellow arrows. This material was likely annealed and recrystallized. (D-E) Glassy or recrystallized particles found in the matrix.

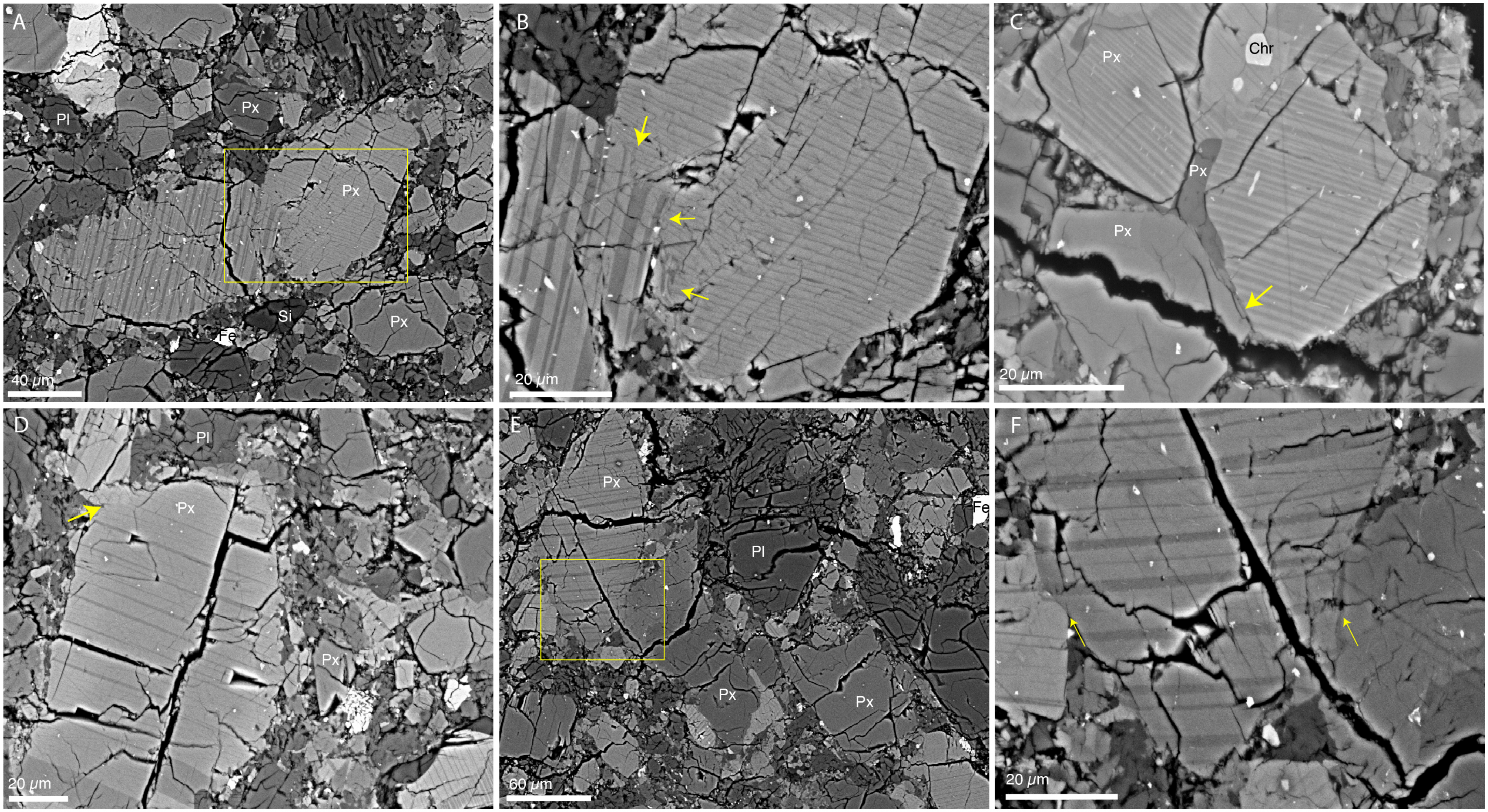

Figure 4.7: BSE images of mineral clasts coalesced together. (A-B) Two pyroxene clasts fused together. Yellow arrows indicate the contact between two clasts where exsolution lamellae bent in B. (C) Two pyroxene clasts fused together, possible thin melt film in between the clasts (yellow arrows). (D) Amalgamation of two clasts along their point of contact (yellow arrow). (E) Various mineral clasts that are fused together (F) Zoomed-in inset of E showcases two areas (yellow arrows) where a larger pyroxene clast is fused with other clasts on either side

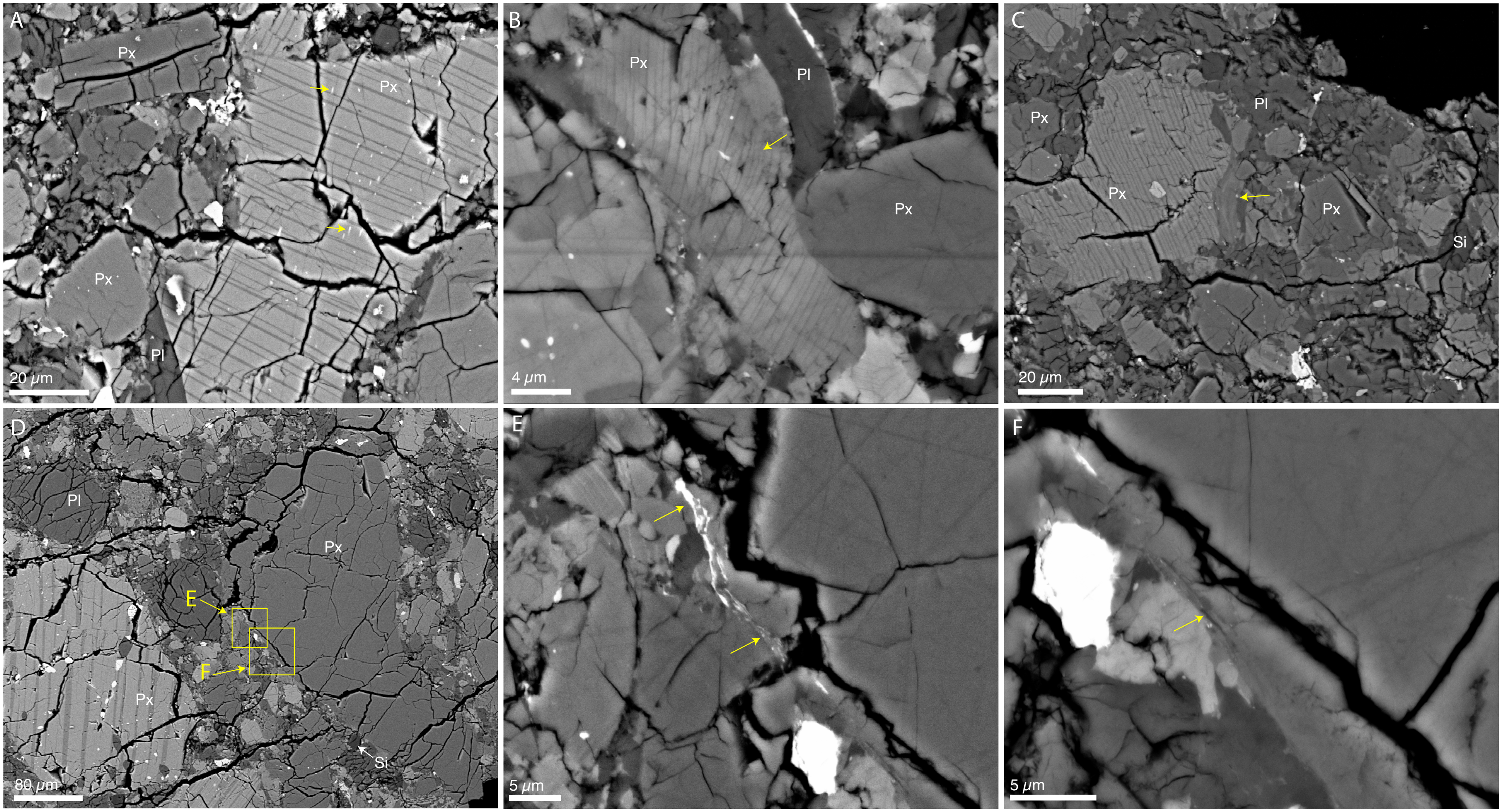

Figure 4.8: BSE images of the mineral clasts in the matrix. (A) Pyroxene clasts with chromite rods indicated by yellow arrows (B) Bent and elongated clast of pyroxene with bent exsolution lamellae indicated by yellow arrows. (C) Irregularly shaped clast in the matrix with flow lines, indicated by yellow arrows. It is present along a pyroxene clast that is near the edge of the meteorite. (D-F) Images of a thin melt vein found along a pyroxene clast indicated by the yellow arrows in E and F

4.2.1 Shock effects

Pyroxene clasts display regular to undulose extinction. Abundant pyroxene clasts contain bent and offset exsolution lamellae (Fig. 4.8B). Plagioclase clasts display a range from regular extinction to mosaicism. Molten components and thin melt films (<1 μm in width) are found along some lithic, mineral, and impact melt clasts (Figs. 4.8C-F). There are no melt pockets, veins, or high-pressure mineral polymorphs in the matrix of Sariçiçek.

4.3 NWA 10922

Matrix in NWA 10922 is composed of mineral clasts and submicron sized material. Mineral clasts include pyroxene, plagioclase, Fe-Ti-oxides, and chlorapatite. All the mineral clasts have a subangular to subrounded shape (Figs. 4.9). Pyroxene and plagioclase mineral clasts range in size from ~5 μm to 70 μm. Fe-Ti-oxide and chlorapatite grains are smaller and vary between ~22 μm and 50 μm in the longest dimension. Most of the matrix is composed of pyroxene and plagioclase, with Fe-Ti oxides disseminated throughout, and minor chlorapatite. Pyroxene mineral clasts include clinopyroxene (pigeonite and augite) and orthopyroxene. Some orthopyroxene clasts have thin exsolution lamellae of clinopyroxene. Clinopyroxene mineral clasts contain trails of inclusions composed of magnetite and silica glass (Figs. 4.9B). Augite clasts have exsolved diopside along the clast edges (Figs. 4.9B). Few plagioclase clasts have microfractures filled with a fine-grained aggregate of a Mg-Fe silicate phase (Fig. 4.9C), that was previously described in the monzonitic and breccia clasts in NWA 10922. Fe-Ti oxides have reaction rims (Fig. 4.9D). The submicron portion of the matrix is composed of the same minerals in a granoblastic texture (Fig. 4.10A-B). It was not possible to resolve the submicron matrix using the FESEM in this study, but McCubbin et al. (2016) reported interlocking texture and grain boundaries that commonly meet at 120° angles in TEM images of the matrix material in the range of 0.1 to 1 μm.

Two elongated and prismatic crystals in the matrix have irregular edges (Fig. 4.10C) Both clasts contain two sets of cleavage planes that intersect at ~ 110° and 70° (Fig. 4.10C). The Raman spectrum of these crystals has two peaks at 337 cm^{-1}, and 293 cm^{-1}, a doublet in the ~650 cm^{-1} region, and a peak peak at 1007 cm^{-1} (Fig. 4.10D). The Raman spectrum agrees very well with the Raman spectrum of orthopyroxene (Wang et al. 2001). The EPMA analysis for 6 points have totals in the range of 95.42 – 97.56, and the average composition in wt% includes 26.58 MgO, 15.15 FeO, 53.15 SiO_2, 0.74 Al_2O_3, 0.46 Cr_2O_3, 0.43 MnO, and 0.12 TiO_2.

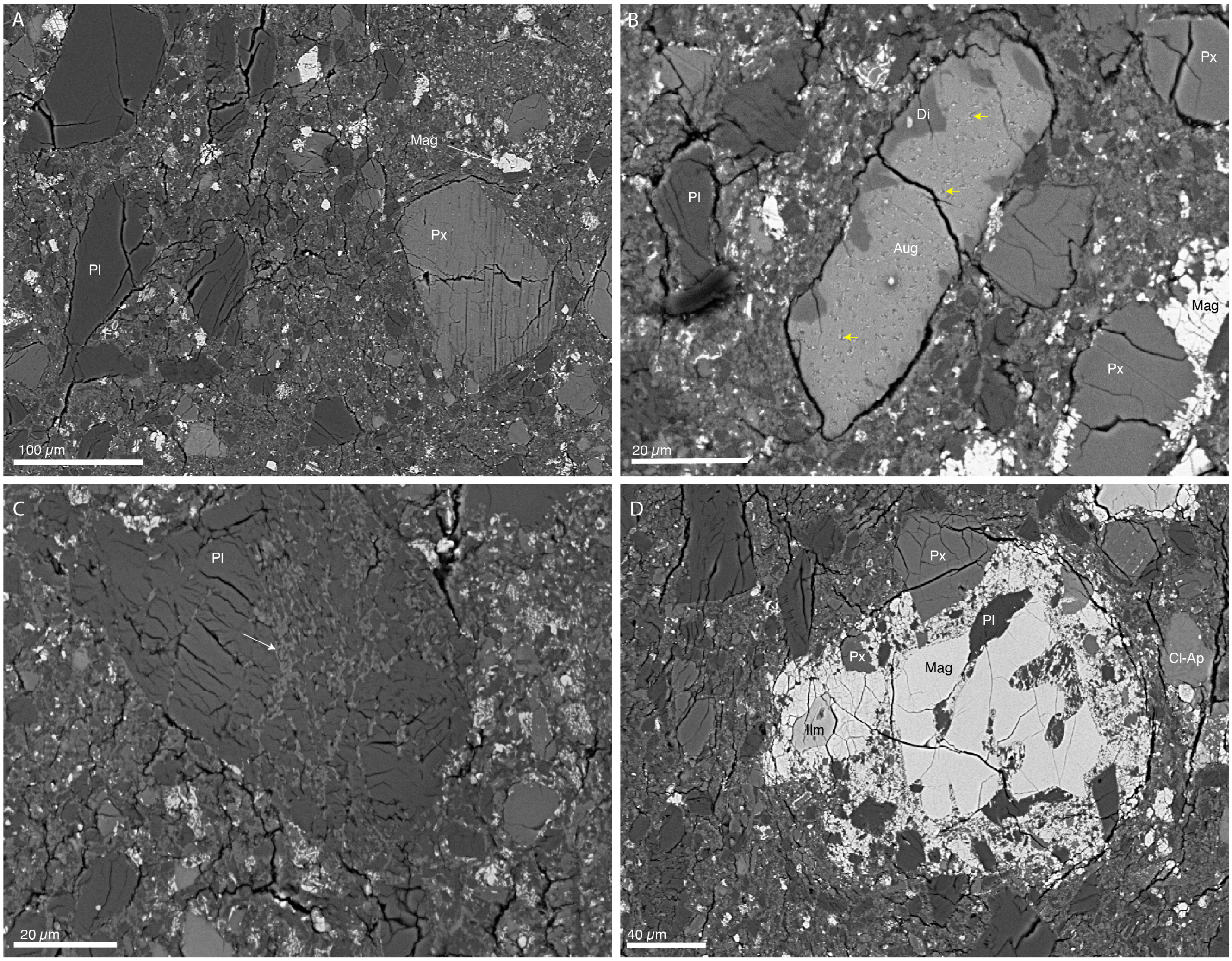

Figure 4.9: BSE images of mineral clasts in the matrix of NWA 10922. (A) Subangular mineral clasts surrounded by finer-grained matrix material. (B) An Fe-rich augite clast that contains exsolved diopside along its left edge. This clast also contains inclusions of magnetite and silica indicated by yellow arrows. (C) A plagioclase clast with microfractures filled with Mg-Fe silicate material. (D) A magnetite clast with a complex reaction rim that contains a symplectite of plagioclase and oxide minerals, and pyroxene mineral clasts.

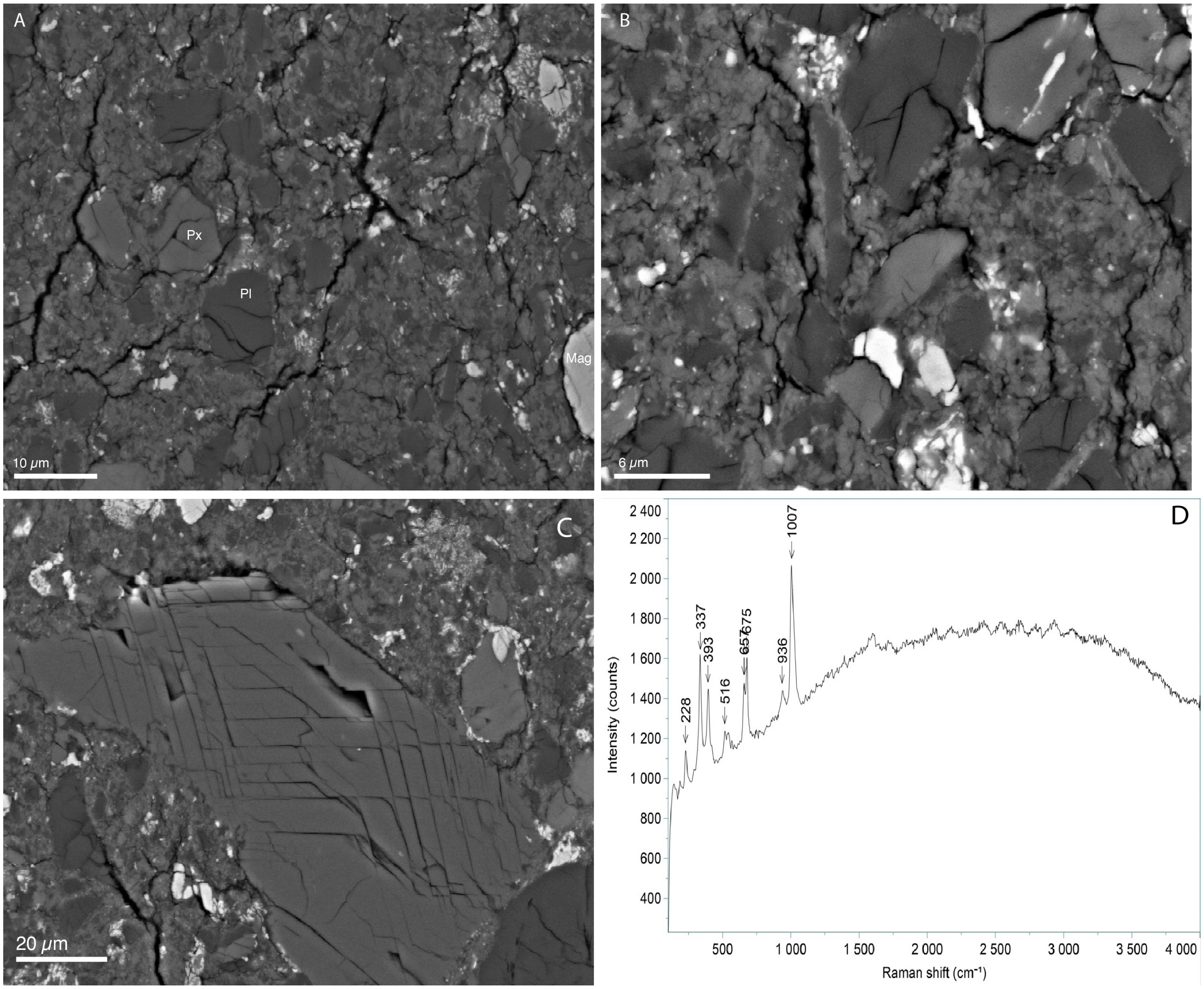

Figure 4.10: BSE images of the matrix material in NWA 10922 (A-B) Matrix in the size range of 1 µm to 5 µm. The material consists of pyroxene, plagioclase, chlorapatite, and oxide mineral grains, whose boundaries are not evident in A or B as they are submicron in size. (C) BSE image of a mineral clast with cleavage angles at ~70º and 110º (D) Raman spectrum of clast in C.

4.3.1 Shock effects

Shock effects are absent in the matrix of NWA 10922. No melt veins, pockets, or high-pressure minerals were observed. Fractures are present throughout the sample, and often occur along the interfaces of clasts and matrix. Clasts presented in the previous chapter have a sharp boundary with the matrix.

Chapter 5: Discussion – Formation and Evolutionary Histories of NWA 14340, Sariçiçek, and NWA 10922

5.1 Clast inventory of each meteorite compared to other similarly classified meteorites

5.1.1 NWA 14340

NWA 14340 contains a wide variety of lithologies that were parts of igneous rocks derived from magmas (lithic and mono-mineral clasts) to impact related (impact-melt clasts, glass spherules and beads). The clasts are dominated by anorthite, indicated by the modal mineralogy of lithic clasts, as is the case for feldspathic regolith breccias derived from the lunar highlands (Korotev et al. 2003, Snape et al. 2011, Gross et al. 2014, Cao et al. 2021). Lithic clasts with Mg-Fe silicate minerals include mainly norites, troctolites, and gabbros. Orthopyroxene and olivine in these clasts have varying Mg and Fe content, suggesting that the clasts in NWA 14340 range between Mg-suite and ferroan anorthosite suite. The lithic clasts also possess a variety of textures including poikilitic, granoblastic, and granular. Impact melt and glassy clasts, some with flow lines, are abundant in NWA 14340 and have various textures and mineralogy, although they are all rich in anorthite.

The clast inventory, range of compositions (Table 3.1) and textures in NWA 14340 agrees with the studied meteorites within the NWA 8046 clan (Lunning and Gross 2019, Fagan and Gross 2020, Zeng et al. 2020, Sheikh et al. 2022, Treiman and Semprich 2023), and with the meteorite's classification as a polymict regolith breccia. Dunite clasts were identified in two paired samples, NWA 14900 and NWA 11421 (Sheikh et al. 2022, Treiman and Semprich 2023); no dunite clasts have been identified in NWA 14340. The presence of dunite clasts in two paired samples is likely due to the heterogeneity in the clastic material present in these regolith breccias.

5.1.2 Sariçiçek

Sariçiçek contains a wide range of mineralogy and textures. Lithic clasts include mostly eucrite and some diogenite clasts, both equilibrated and unequilibrated, which agrees with its classification as a eucrite-rich howardite (Unsalan et al. 2019). It contains various impact melt clasts and brecciated clasts that are suggestive of previous impact events and representative of regolith material. Iron and chondritic exogenous clasts were identified (Fig. 3.7B and I) which also agrees with similar observation made by Unsalan et al. (2019). Overall, the clast inventory (Table 3.2) agrees with this rock being a howardite and is comparable to clasts found in other regolithic howardites (e.g., Ikeda and Takeda 1984, Pun et al. 1998, Sisodia et al. 2001, Lorenz et al. 2007, Beck et al. 2012, Janots et al. 2012, Mittlefehldt et al. 2013, Lunning et al. 2016, Gregory et al. 2017, Patzer and McSween Jr 2018, Unsalan et al. 2019).

Unsalan et al. (2019) recognized most lithic clasts within Sariçiçek as basalts with ophitic to subophitic textures, and clasts rich in plagioclase and silica. Observations of lithic clasts in this study agree with the observations made by Unsalan et al. (2019), and additionally contain basalt clasts with coarse-grained, vitrophyric, and brecciated textures. The sections of Sariçiçek that Unsalan et al. (2019) inspected had rare olivine. Olivine in the thin section studied here would be better characterized as a minor constituent than rare, as it is present in mono-minerallic clasts, within impact melt clasts, and in three out of the four large diogenite lithic clasts. Additionally, Sariçiçek is one of the few HED meteorites to contain a dunitic clast (Fig. 9F). Other howardites with dunite clasts include NWA 2968, NWA 5784, NWA 5968, NWA 6157, MIL 03443 (Bunch et al. 2006, 2010, Mittlefehldt 2008, Beck et al. 2011).

5.1.3 NWA 10922

The NWA 7034 suite of martian breccias has been studied by various authors that targeted characterizing the clasts in the samples (Humayun et al. 2013, Santos et al. 2015, Wittmann et al. 2015, Hewins et al. 2017), identifying traces of secondary alteration (Lorand et al. 2015, Liu et al. 2016, MacArthur et al. 2019), petrological interpretation of the breccia (McCubbin et al. 2016), and chronology and isotopic studies to date the entire rock, its constituents, and geological events in the breccia's history (Cartwright et al. 2014, Lindsay et al. 2016, Nyquist et al. 2016, Cassata et al. 2018, Hu et al. 2019, MacArthur et al. 2019). The mineral, lithic, breccia, impact-melt, and impact-melt spherules characterized in this study (Table 3.3) agree with previous inspections of NWA 7034 and its paired stones. An orthopyroxenite lithic clast (Fig. 3.11C) was identified in this study which has not been recorded in other paired stones. Santos et al. (2015) and Wittmann et al. (2015) identified Fe-Ti-P rich clasts that are observed to have 55 wt% feldspar, 22 wt% apatite, 20 wt% ilmenite, and 4 wt% magnetite, and overall lack pyroxene; no such clast was identified in NWA 10922.

McCubbin et al. (2016) conducted shape and size analysis of all the clasts in NWA 7034 and concluded that the constituents were deposited as pyroclastic fallout deposits. Identification of accretionary lapilli and dust rim around all clasts support this as the deposition mode of the clasts in NWA 7034 and its paired stones (Wittmann et al. 2015, MacArthur et al. 2019). In this study, irregularly shaped impact melt clasts with round edges likely cooled to a certain extent while airborne, as evidenced by the fine-grained matrix texture, in contrast with the coarser grained matrix texture of breccia clasts. Impact melt spherules have different mineralogies and sizes. The largest spherule (1.7 µm; Fig. 3.13J) has Fe-oxide veins that truncate at the spherule boundary. Similarly, McCubbin et al. (2016) found Fe-oxide veins in several breccia clasts that were suggestive of hydrothermal alteration prior to the breccia's lithification. In NWA 10922, the large spherule studied here shows a gradual transition to the matrix (Fig. 3.13J), which is suggestive of the spherule having been emplaced in-situ while it was still at least partially molten. However, Fe-oxide veins that truncate at the spherule boundary suggest that the spherule had crystallized and experienced some hydrothermal alteration prior to being lithified in NWA 10922, and the diffuse boundary with the bulk matrix is likely a result of the thermal annealing of the breccia after lithification. Such annealing is further supported by the devitrified texture of the rim of the spherule.

Plagioclase in a monzonitic clast, one breccia clast, and a clast within the matrix has been altered to a Mg-Fe silicate fine-grained aggregate along fractures. This alteration product is present only along fractures, which suggests that it resulted from aqueous alteration, where Mg-Fe-rich fluids circulated through these clasts. If the plagioclase experienced aqueous alteration, the Mg-Fe silicate aggregate material was likely a hydrated phase, such as an amphibole-group mineral or phyllosilicates suspected to occur on Mars in hydrothermally altered minerals (Osinski et al. 2013). However, the Raman spectrum of the Mg-Fe silicate aggregate material lacks the O-H peak in the 3500 cm^{-1} region (Fig. 3.12B), indicating subsequent mineral break down and dehydration. The presence of the Mg-Fe silicate aggregate in only a few clasts highlights the clasts' geological history before lithification in NWA 10922.

5.2 Shock conditions deduced from the breccias

5.2.1 NWA 14340

5.2.1.1 Bulk shock conditions

Felspar is sensitive to shock effects (Pickersgill et al. 2021). Since NWA 14340 is composed predominantly of the mineral feldspar, shock effects in feldspar throughout the rock can be used to infer the shock history of the rock, with shock effects in other minerals acting as complimentary shock indicators. Most of the shock effects identified in NWA 14340 can be divided into: 1. Shock effects that occur in effectively all the clasts inspected; and 2. Shock effects restricted to individual or a limited number of clasts.

Shock effects that occur within all the lithic clasts and mineral clasts were likely induced by the pressure the bulk rock experienced during a late-stage shock event in its history. All plagioclase within lithic clasts and mineral clasts in the matrix displays patchy undulose extinction (Fig. 3.4). The patchy undulose extinction has been observed in some of the Apollo regolith breccia and impact melt breccia samples (e.g., Kridelbaugh et al. 1973, Ryder 1980). Kridelbaugh et al. (1973) referred to this occurrence in plagioclase as mosaically recrystallized anorthite that could possibly be devitrified diaplectic glass. In NWA 14340, plagioclase in most mineral clasts and lithic clasts exhibiting patchy undulose extinction is relatively smooth in BSE imaging, while the accompanying pyroxene or olivine grains in the same lithic clasts are pervasively fractured (Fig. 3.5A). The same plagioclase is also birefringent, suggesting that is it not maskelynite (Fig. 3.4). If it had converted to maskelynite and then subsequently devitrified, the recrystallized phase should have the same crystal orientation as the host (Ostertag and Stöffler 1982). However, that is not the case as the “recrystallized” plagioclase has a distinct orientation from the remaining plagioclase in the crystal (Fig. 3.4). There are also no flow lines in plagioclase clasts (Fig. 3.4). So, the plagioclase did not experience melting. So, without experimental data on conditions necessary to produce patchy undulose extinction in plagioclase seen in NWA 14340, it cannot be used as a solid shock indicator, even though lunar highland breccias with this plagioclase texture were referred to as highly shocked samples (Kridelbaugh et al. 1973).

Plagioclase within lithic and mineral clasts contain PDFs (Fig. 3.4F and 3.6E) which suggests that the bulk rock pressure was 18-22 to 34 Gpa (Stöffler et al. 2018). Since most plagioclase clasts did not transform to maskelynite, this suggests that the bulk rock pressure was less than ~ 24 GPa, (Fritz et al. 2019). Pyroxene grains display undulose extinction to weak mosaicism. This deformation in pyroxene can occur over a large range of pressures, undulose extinction occurs between 5-10 to 20-30 Gpa and mosaicism between 20-30 to ~70 GPa (Stöffler et al. 2018). Olivine has higher shock tolerance than both plagioclase and pyroxene, and no considerable shock effects were observed in olivine throughout NWA 14340. Olivine begins exhibiting crystal strain at pressures > 20 GPa (Jeanloz 1980), which aids in constraining the peak equilibrium shock pressure experienced by the bulk rock in the range of 18 - ~20 GPa (Stöffler et al. 2018).

5.2.1.2 Localized shock conditions

The formation of tissintite is widespread in the matrix of NWA 14340, present within glassy regions with large vesicles and flow lines (Fig. 4.4A). This phase has crystallized from shock-induced melt as inferred by its fine-grained igneous textures (Fig. 4.4B, D, and F); such texture is not consistent with solid-state transformation. Tissintite clusters are also present in flow-shaped form and contain higher Mg and Fe contents than plagioclase (Fig. 4.4D), confirming that they grew from shock-induced melt that had chemical contributions from entrained olivine and pyroxene clasts. Tissintite is present along the edges of glassy regions and clasts (Fig. 4.4D-E), and within glassy regions where it appears to have nucleated on the rims of mineral clasts (Fig. 4.1B).

The occurrence of coesite is restricted to clasts that are variably composed of SiO_2 glass, quartz, and tridymite, and entrained within glassy matrix along with tissintite. Coesite also has a distinct occurrence (Fig. 4.3F) and does not exhibit the euhedral morphology that would be expected were it to have crystallized from melt (Fig. 19F; e.g., Pang et al. 2016, Chen et al. 2019). So coesite likely formed as a result of solid-state transformation of amorphous silica and quartz. Zhang et al. (2021) similarly observed tissintite clusters and coesite in glassy regions within nine lunar regolith breccia meteorites. Experimentally formed tissintite from amorphous plagioclase is stable at 6-8 GPa pressure and 1000-1350 °C temperature conditions (Rucks et al. 2018). Tissintite has been reported in eucrite, martian, and lunar meteorites to be stable in the range of ~10 GPa to >19 GPa (Walton et al. 2014, Ma et al. 2015, Pang et al. 2016, Chen et al. 2019, Zhang et al. 2021). Coesite is stable at pressures > 2.5 GPa; however, at pressures >7.5 GPa, silica quickly transforms to its other high-pressure polymorph, stishovite (Mansfeld et al. 2017). Following these shock constraints, Zhang et al. (2021) proposed shock pressures in the range of 4-8 GPa for glassy regions of nine-lunar meteorites in their study. The same pressure range in inferred for glassy regions in NWA 14340 based on similar high-pressure mineral assemblages and textures.

Zhang et al. (2021) also observed SiO_2-rich corundum towards the inner zones of glassy regions. No corundum was found in NWA 14340, but instead, garnet is present within and along a few tissintite clusters (Fig. 4.5A-B and E). Dendritic garnet is only associated with tissintite clusters and present within the same glass of plagioclase that has higher Mg and Fe (Fig. 4.5B and E). Garnet is likely a reaction product between Mg-rich olivine and plagioclase melt, as in some clusters it is associated with Mg-rich olivine grains embedded in the tissintite clusters (Fig. 4.5E). Garnet as the reaction product between plagioclase and forsteritic olivine has been documented in terrestrial metaperidotites and induced by anhydrous high pressure metamorphism (Miller 1974). Various Pressure-Temperature diagrams exist for dry reactions between forsteritic olivine and plagioclase (e.g., Kushiro and Yoder Jr 1966, De Ronde and Stünitz 2007), but none are in the high pressure range of 4-8 GPa. Garnet is also present within tissintite clusters where there are no olivine grains nearby (Fig. 4.5B), though the heterogeneously distributed contributions from olivine in the plagioclase glass could still lead to garnet nucleation. This is likely the case as garnet is not as widespread as tissintite and coesite in the glassy matrix. Thus, nucleation of garnet within certain tissintite clusters is dependent on the composition of glass as well as the shock pressure.

Texturally, garnet is always found either within the inner zone of tissintite clusters or along the edge of the tissintite cluster, towards the center of the glassy area (Fig. 4.5B and E). In both cases, the textural occurrence of garnet suggests that it grew after tissintite in hotter and relatively slow cooling zones. Hence, the pressure constraint for garnet would be lower than that of tissintite. This inference is also supported by coarser grains of tissintite in the inner zones and finer grains along the edges of tissintite clusters (Fig. 21B and E).

Garnet crystals identified in NWA 14340 are too small for proper EPMA and EDS analysis. Raman spectroscopy was the only applied technique that produced unequivocal evidence for the crystals to be identified as garnet (Fig. 4.5C). High-pressure garnet found in meteorites is majoritic, also called super-silicic garnet (e.g., Pang et al. 2016, Chen et al. 2019, Du et al. 2024). The majorite substitution involves coupled substitution of $(Mg,Fe,Ca)^{2+}$ and Si^{4+} into the octahedral sites in the garnet mineral structure (Collerson et al. 2010). Majorite bearing garnets are ideal for pressure estimates as their compositions are pressure dependent (Roermund et al. 2000). Lacking compositional data, I will compare the Raman spectrum of garnet in NWA 14340 with those in the literature. The Raman spectrum of garnet acquired here has major peaks at 368 cm^{-1}, 669 cm^{-1} , 902 cm^{-1}, 1006 cm^{-1} (Fig. 4.5C), which is consistent amongst various crystals and with the Raman band assignments of garnet (Mingsheng et al. 1994). The characteristic peak of garnet in its Raman spectrum occurs within ~870 cm^{-1} to ~ 930 cm^{-1}, with endmember majorite having a Raman shift at 929 cm^{-1} (Hofmeister et al. 2004). The characteristic peak in the Raman spectrum of NWA 14340 garnet at 902 cm^{-1} is downshifted compared to endmember majorite, confirming that the garnet found in NWA 14340 does not represent pure endmember majorite and is instead likely coonsists of a majorite component. 2% to 11-22% majorite bearing garnet found in shocked meteorite and terrestrial samples have characteristics peaks in their Raman spectra that range from 906 cm^{-1} to 910 cm^{-1} (Pang et al. 2016, Walton et al. 2016, Chen et al. 2019), which is comparative to the Raman spectra of garnet found in NWA 14340. Hence, it is likely that the garnet identified in NWA 14340 is also super-silicic, with the majoritic component estimated to be between ~ 2-6%, as this range has been observed in association with tissintite and coesite in other meteorites (Pang et al. 2016, Chen et al. 2019). So, evidence that suggests that the garnet is super-silic includes: 1. It is present in shock-induced glass and so has a likelihood of having grown in high-pressure conditions; and 2. Its Raman spectrum is comparable to the Raman spectra of super-silicic garnet identified in other shocked samples.

Texturally, this is the first identification of fine-grained and dendritic garnet present within tissintite clusters (Fig. 4.5B and E), and is the most comparable to garnet + glass in the middle of a mineralogically zoned melt vein in eucrite meteorite NWA 8003 (Pang et al. 2016). Garnets in both NWA 14340 and NWA 8003 were likely one of the last forming high-pressure minerals from the shock melt. Pang et al. (2016) suggested that garnet in the middle of the melt vein in NWA 8003 likely crystallized last, as it is concentrated in the hot and slowly cooled zone (inner zone of the melt vein) and likely formed at shock pressures less than ~8.5 GPa. In NWA 14340, garnet likely crystallized at pressures < 8 GPa, as 8 GPa is the higher limit deduced from occurrence of tissintite and coesite.

5.2.1.3 Shock histories of individual clasts

Some clasts show evidence of a shock history prior to being brecciated in NWA 14340. Three lithic clasts rich in plagioclase experienced a complicated shock history that likely involved plagioclase transforming to maskelynite and subsequent devitrification into fibrous crystals (Fig. 3.5D-F and I-K). There are abundant vesicles in the clasts, which have been shown to occur in plagioclase diaplectic glass as it devitrifies (Ostertag and Stöffler 1982). Conversion of anorthitic plagioclase to diaplectic glass occurs at pressures > 24 GPa (Fritz et al. 2019). These shock effects are restricted to these clasts, and not observed in other plagioclase mineral or lithic clasts with abundant plagioclase. Accordingly, these clasts did not experience localized shock effects in NWA 14340, as that would require melting of plagioclase along their contact with denser silicate minerals, where shock wave refraction and reflection can induce a shock pressure and temperature excursion (Sharp and DeCarli 2006).

Two individual clasts experienced complete melting of parts of the clasts (Fig. 3.6A-D). These clasts are both composed of ferro-magnesian silicates and anorthite, like a lot of the other norite, troctolite, and gabbro clasts in NWA 14340. Both clasts also have their melting products intact within the original clast, which is suggestive of in-situ melting. However, the troctolitic clast composed of anorthite, Mg-olivine, and Mg-orthopyroxene and melt, which is now recrystallized, has a sharp contact with the matrix (Fig. 3.6A-B). The melted region also does not have any of the mineral clasts mixed in from the adjacent matrix (Fig. 3.6B). So, this clast likely experienced melting prior to being lithified in NWA 14340. Therefore, this clast likely experienced at least one shock event before being lithified in NWA 14340 that caused the melting. The melting of plagioclase, pyroxene, and olivine and recrystallization in the troctolite clast is suggestive of an equilibration shock pressure of >~60-65 GPa (Stöffler et al. 2018), which is much higher than what was inferred to have been experienced subsequently by the bulk rock.

The second gabbroic clast that experienced complete melting of pyroxene and plagioclase (Fig. 3.6C-D), would have required shock pressures in a similar range (>60-65 GPa). However, the recrystallized portion contains anhedral clasts of olivine, that are not part of the original clast (Fig. 3.6D). This is indicative of mixing with the adjacent matrix and in-situ melting of the clast, likely due to localized heating within the breccia and/or porosity near the clast. The edge of this clast likely melted prior to the shock event that led to the crystallization of tissintite as the recrystallized portion of the clast does not contain tissintite. Instead, the melt cooled to a crystalline texture that mantles this clast. Additionally, tissintite shows a texture that is consistent with nucleation along the edge of the recrystallized portion (Fig. 4.4B), which also suggests that tissintite grew after the clast experienced melting. A summarized history of this clast is as follows: 1. Excavation from its protolith; 2. Mixing and lithification in NWA 14340, with melting likely occurring during lithification due to localized heating; 3. Crystallization of tissintite in the matrix, along the boundary of the clast's recrystallized portion with the matrix.

One of the lithic clasts has orthopyroxene and plagioclase that shows evidence of melting along their grain boundaries (Fig. 3.6E-F). Shock melting usually begins at grain boundary margins of two minerals with contrasting shock impedance (Sharp and DeCarli 2006). The differing shock impedance allows for shock waves to reflect and refract and allows for a localized shock pressure to deviate from what has been experienced by the bulk rock (Sharp and DeCarli 2006), which was almost certainly the case for this clast. Plagioclase melts at pressures > 45 GPa and incipient melting of pyroxene occurs at > 70 GPa (Stöffler et al. 2018). For both minerals to melt simultaneously, the localized shock excursion would have been greater than 45 GPa and likely below 70 GPa.

5.2.2 Sariçiçek

Unsalan et al. (2019) did not describe the shock stage of Sariçiçek, although they comment on lithic and mineral clasts having distinct shock effects that include irregular fractures, kinked pyroxene lamellae, and portions of the matrix being so fine-grained as to be opaque. In this study, I focused on shock effects within clasts and the matrix. Clasts have variable shock effects that range from undulose extinction to mosaicism in plagioclase and regular extinction to undulose extinction in pyroxene. Plagioclase mineral clasts in the matrix are fractured and display undulose extinction, whereas pyroxene is fractured and relatively unshocked, with some clasts displaying undulose extinction. This suggests a bulk rock pressure estimate in the range of 5 to 10-12 GPa and post shock temperatures < 50 ºC for Sariçiçek (Stöffler et al. 2018).

There are also shock effects restricted to individual lithic and mineral clasts in this meteorite that reveal individual clasts that have experienced differing shock conditions prior to incorporation in the breccia. The pyroxene mineral clast with a shock vein and pyroxene crystallites within pyroxene glass (Fig. 3.10A) indicate a localized shock excursion of ~> 70 GPa as pyroxene begins melting above this pressure (Stöffler et al. 2018). The shock vein truncates at the clast boundary, so this shock effect is a result of a prior impact event. A eucrite cumulate clast contains a silica grain that has transformed to diaplectic glass, as indicated by the outward radiating fractures (Fig. 3.9H-I). This transformation suggests the clast experienced shock pressures of 34-50 GPa, the range needed for silica to become diaplectic glass (Stöffler et al. 2018). The highly shocked breccia clast contains a melt pocket with no high-pressure polymorphs of pyroxene, olivine, plagioclase, or silica (Fig. 3.8). Entrained plagioclase and silica clasts transformed to diaplectic glass (Fig. 3.8B-C); these transformations require shock pressures of ~ 34-45 GPa (Stöffler et al. 2018). Sariçiçek's bulk rock has evidence for only low shock conditions, whereas its constituents have experienced much higher shock pressures.

Only two of the basalt clasts contain recrystallized plagioclase (Fig. 3.9D-G). One of the clasts contains sub-grain domains with distinct boundaries in the plagioclase grains (Fig. 3.9D,) in this case that have recrystallized without any evidence of melting (vesicles or flow lines). This clast is different from partial maskelynite formation or fine-grained recrystallization in NWA 14340, as it has coarser recrystallized grains that are twinned. Additionally, no shock effects were observed in the pyroxene within same clasts. Complete conversion of anorthic plagioclase to diaplectic glass occurs at 24-28 GPa pressures (Fritz et al. 2019). Melting and recrystallization of plagioclase occurs at higher pressures, > 45 Gpa (Stöffler et al. 2018). The plagioclase in this clast, unaffected by these shock effects, experienced pressures below 24 GPa. Additionally, recrystallization into sub grains within the original plagioclase crystal is likely produced from solid-state dynamic recrystallization and plastic deformation as a result of high temperature modification (Rosenberg and Stünitz 2003).

The second clast with recrystallized plagioclase (Fig. 3.9 E-G) has experienced melting along pyroxene and plagioclase boundary, has PDFs and has fine- grained recrystallized texture for a part of the plagioclase grain (Fig. 3.9 G). Since, plagioclase melts at pressures > 45 GPa and incipient melting of pyroxene occurs at > 70 GPa (Stöffler et al. 2018).

5.2.3 NWA 10922

In NWA 10922, high-pressure shock effects are absent in both the matrix and clasts. There is a reported occurrence of a shock-induced melt vein in an individual clast of NWA 7475, a stone paired with NWA 7034 (Wittmann et al. 2015). Leroux et al. (2016) identified mechanical twins in Ca-rich pyroxene throughout the meteorite, suggesting that the deformation was a result of a shock event experienced by the breccia after lithification.

NWA 7034 and its paired stones are composed of clasts that each have distinct geological histories. In NWA 10922, these histories include Fe-oxide veins in a spherule that truncate at the spherule boundary and plagioclase modification to Fe-Mg silicate assemblage in a few clasts. Additionally, the breccia clasts in NWA 10922 and the paired stones of NWA 7034 are unique because they show evidence of a prolonged pre-lithification history involving brecciation and lithification (McCubbin et al. 2016).

Processes such as aeolian, volcanic, or impact events can transport and amalgamate constituents with distinct geological histories. However, there is no evidence for clast rounding and size sorting, in support of aeolian transport and deposition of clasts in NWA 10922 or in the studied paired stones (e.g., McCubbin et al. 2016). Additionally, the components with distinct alteration histories were likely not deposited in a volcanic eruption. Therefore, impact cratering is likely the process that led to the lithification of clasts in NWA 7034 and its paired stones. The lack of shock effects in the clasts and matrix of NWA 10922 supports that the impact event leading to the breccia's lithification induced low shock pressure conditions.

5.3 Unraveling the formation mechanisms and binding agents of the breccias

Spray (2016) provided a comprehensive review of how planetary regolith binds together to form different types of regolith breccias via shock sintering in four stages (Fig. 1.1). The first two stages involve comminution and mixing of the regolith via impact events. All of the breccias analyzed in this study have fragmented clasts with diverse lithologies and texture. This suggests that the regolith on their distinct parent bodies experienced mechanical disruption and mixing caused by impact events. The latter two stages are what leads to the formation of regolith breccias (Fig. 1.1) and are described below for each studied breccia.

5.3.1 NWA 14340

The current matrix of NWA 14340 is fine-grained to glassy. The glass was likely produced by melting of the finer-grained regolith material (1-2 μm in size), that was primarily composed of plagioclase with some pyroxene and olivine. The melted material quenched to glass, with crystallization of tissintite throughout. So, the current glue that holds components of

NWA 14340 together is the interclast glass. The following observations suggest that the glassy matrix formed after the lithification of NWA 14340 during at least one shock event:

1. Fractures from clasts do not extend outward into the glassy matrix.
2. Tissintite present within glass in the matrix occurs along clast boundaries, suggesting it grew there. Although there are clasts that experienced grain boundary melting, tissintite, along with coesite and garnet, are restricted to the matrix only.
3. Vesicles in glassy regions would likely have deformed if subsequent shock events had compressed NWA 14340.
4. Shock effects in lithic and mineral clasts correspond to different shock pressures than the matrix. If the matrix had melted during the first impact event at ~18-20 GPa pressure conditions, the Ca-Al-silicate phase, donwilhelmsite, would likely have appeared as the product of shock-induced anorthitic melt at ~18 Gpa (Liu et al. 2012). Additionally, stishovite would be present as the high-pressure polymorph of tridymite (stable at pressure > 7.5 GPa; (Mansfeld et al. 2017). This suggests that NWA 14340 likely experienced two shock events: the initial shock event lithified NWA 14340 under ~18-20 GPa; the second shock event ejected it from the lunar surface, forming glassy regions with tissintite, coesite, and garnet in its matrix

There are two formation scenarios for NWA 14340: 1. Clasts were initially buried within a regolith layer, and then shock compacted, followed by matrix sintering. This shock event likely caused the patchy undulose extinction and PDFs observed in plagioclase clasts. This scenario requires at least one impact event during NWA 14340's lithification. 2. Clasts were ejected, deposited, and buried in an ejecta blanket, where they underwent sintering and lithification.

Subsequently, another impact event induced the patchy undulose extinction pattern and PDFs in plagioclase, necessitating at least two impact events in NWA 14340's lithification history.

The precursor matrix of NWA 14340 has been overprinted by shock-induced melting and subsequent quenching to glass. So, the matrix that formed after lithification cannot be observed directly. Similarly, lunar regolith breccias have often been reported with fine-grained to glassy and vesicular matrix (e.g., Bischoff 1996, Bischoff et al. 1998, Jolliff et al. 1998, Korotev et al. 2009, Nagaoka et al. 2013, Calzada-Diaz et al. 2017, Zhang et al. 2021), whereas some have welded (e.g., Koeberl et al. 1991), crystalline (Xia et al. 2021), or fine-grained clastic matrices (e.g., Demidova et al. 2003). Regolith breccia meteorites with crystalline matrices often have sub-ophitic textures, as the meteorite likely experienced slower cooling after high pressure shock events (e.g., Spray et al. 2007). This is likely not the case for the precursor matrix of NWA 14340, as there is no indication of a crystalline portion of the matrix with similar textures. The precursor material was likely fine-grained regolith material that was compacted together by the lithification shock event and subsequently sintered (Spray 2016).

5.3.2 Sariçiçek

5.3.2.1 Compaction mechanism

The matrix in Sariçiçek is clastic with seriate texture; melt or high-pressure mineral phases are absent. Sariçiçek is composed of distinct lithologies (Table 3.2), some of which show distinct shock effects that developed in clasts before they were incorporated in the breccia. The likely process that can explain lithification of such components in a rock is impact cratering. Compaction of the matrix in Sariçiçek occurred due to shock welding, as inferred from the following observations. Many mineral clasts in the size range of 10 – 50 μm have angular shapes

(Fig. 4.6A-D). These clasts are also fused or compressed together via solid-state bonds and likely some sintering, as opposed to melting between their contacts (Fig. 4.7). Mckay and Morrison (1971) refer to this as grain interpenetration that leads to tightly packed breccias. Mineral clasts in the matrix have all experienced shear and brittle deformation, and have experienced bending, folding, fracturing, and fragmenting (Fig. 4.7-4.8). Fractures, throughout the meteorite, penetrate across rather than around grain boundaries for all types of clasts, another indication of shock compressed breccias (Fig. 4.6-4.8; Chao et al. 1971).

Pressures needed to produce coherent rocks in artificial explosions from shock lithification are estimated to be in the range of 10 – 20 GPa (Short 1970). Lunar regolith can be shock-lithified at pressures ~ 17 GPa (Schaal and Horz 1980). Additionally, weakly lithified terrestrial samples at missile impact craters have been suggested to form at pressures well under 10 GPa, and likely around 5 GPa. Weakly shock-lithified meteorites from the moon and asteroids would have to survive another impact event that would lead to their excavation. Sariçiçek's peak bulk rock pressure is estimated to range from 5 to up to 10-12 GPa, which reflect shock effects from the impact event(s) that led to its lithification and the subsequent impact event that led to its excavation from the surface of 4 Vesta. It is likely that the shock event(s) that led to Sariçiçek's lithification applied lower pressures than its maximum pressure estimate range. Low pressures at ~ 5 GPa can produce a weakly lithified sample (Kieffer 1975). Sariçiçek was likely situated close to the surface of 4-Vesta, suggested by Unsalan et al. (2019) based on its high noble gas isotopes from solar wind implantation and siderophile elements from chondritic contamination. So, a mild shock event likely lofted the rock from 4 Vesta's surface, leaving an imprint of low (i.e., 5-12 GPa) shock effects in the breccia.

5.3.2.2 Post compaction thermal treatment

There is no evidence of any large-scale thermal treatment (sintering or annealing) on the breccia after its lithification on the microscale level. However, submicron sized material that is difficult to image clearly in FESEM could possibly have sintered as nanosized particles have lower sintering temperatures and undergo rapid grain growth compared to micron sized particles (Fang and Wang 2010, Spray 2016). Optimal temperatures for martian and lunar regolith stimulants are between 1100 °C and 1200 °C. Sariçiçek's post shock temperature is not comparatively high enough to cause thermal sintering or annealing, especially as the heat likely also dissipated into the surrounding material where the breccia was located. Sintering in breccias often results from sustained external heat sources like impact melt sheets or endogenic dykes (Spray 2016), and there is no evidence of Sariçiçek having deposited near an external heat source.

Mineral clasts as small as ~ 5 μm in the matrix are angular and have sharp edges (Fig 4.6C), also suggestive of a lack of melting or sintering along their edges, as sintered grains exhibit roundness, neck growths, and amalgamation (German 2014). Thin melt films are present along a few clasts (Fig. 4.8D-F), which are likely a result of localized shock pressure and temperature excursions, and occurred after the sample was lithified. If the sample was sintered or annealed at a constant temperature from an external heat source, high temperature modifications would have been widespread and homogeneous throughout the meteorite. Since Sariçiçek has no evidence of post impact sintering or annealing, this suggests that compaction via shock waves was sufficient to lithify Sariçiçek into a coherent rock.

5.3.3 NWA 10922

5.3.3.1 Compaction mechanism

The matrix of NWA 10922 is composed of mineral clasts that are subangular to subrounded in shape (Fig. 4.9A). There is minimal evidence for shock compaction in NWA 10922, consistent with the low shock conditions inferred from this study. Mineral clasts larger than ~50 μm are rarely in contact with one another (Fig. 4.9). The mineral clasts are also not fused together and do not impinge on one another, a feature that is observed in lunar breccias as evidence of shock compaction (Mckay and Morrison 1971). Fractures in NWA 10922 frequently occur around the clasts as opposed to across them (e.g., Fig. 4.9B), as they do in coherent rocks that have been shock lithified (Chao et al. 1971). Compaction in NWA 10922 likely occurred due to burial instead of shock as NWA 7034 and its paired stones were likely buried in a hot impact ejecta blanket during lithification (McCubbin et al. 2016, MacArthur et al. 2019).

5.3.3.2 Post-lithification increased temperature treatment

The matrix of NWA 10922 has been thermally annealed, resulting in a submicron sized recrystallized assemblage composed of plagioclase, pyroxene, phosphates, and Fe-oxides (4.10A-B). Based on the grain size of the annealed matrix, McCubbin et al. (2016) suggest thermal annealing either occurred at high temperature of 700-800 °C for a short duration or mild temperatures of 500-700 °C for a long duration. At higher temperatures or longer duration, grain growth would start to occur that would result in recrystallized grains amalgamating to form larger grains. Thermal annealing of the matrix is supported by the roundness of micron sized plagioclase and pyroxene grains and submicron material recrystallizing on these coarser rounded grains (Fig. 4.10B). The interconnected texture throughout the matrix suggests an external heat source, likely from the impact melt sheet that formed post-collision in the crater. Localized shock heating within the breccia is unlikely to have created such uniform annealed textures.

The two mineral clasts in the matrix that have extensive hatched cleavage planes with intersecting angles at ~ 110º and 70º (Fig. 4.10C), do not match with the expected cleavage plane intersection at ~90º for pyroxene or ~60º and 120º of amphibole. These crystals have a composition and Raman spectra that agrees well with orthopyroxene (Fig. 4.10D). Additionally, the Raman spectra is missing any OH peaks in the 3500 cm^{-1} regions expected for amphibole minerals (Fig. 4.10D). Oblique sections of the sample may cause cleavage plane angles to appear slightly offset from the characteristic 90º angle of pyroxene. Investigating this possible artifact would require the sample to be further prepared as a thin section and focusing through the cleavage plane under an optical microscope could reveal the true angle between cleavage planes. Alternatively, these clasts might represent precursor amphibole clasts that were transformed to orthopyroxene. Pyroxene in this context is acting as a pseudomorph. The external amphibole crystal habit and near cleavage pattern is retained in the transformation, which is why the observed cleavage planes do not match the typical orthopyroxene cleavage intersection angles. Amphibole $\rightarrow$ pyroxene pseudo polymorphic reactions have been observed in a laboratory experiment before as a result of thermal annealing (Freeman and Frazer 1968). The authors mention that such polymorphic reaction most probably occurs in minerals with close chemical and structural relationships and where minor atomic movements are necessary to achieve the final structure. The transformation is strongly dependent on temperature and occurs at temperatures > 700 ºC for crocidolite, part of the sodium amphibole supergroup. Pseudomorphic transformation of Mg-Fe-rich amphibole into pyroxene has not been documented in the literature. However, drawing from the temperature transformation of crocidolite, it can be inferred that the matrix of NWA 10922 underwent high-temperature annealing for a brief duration, consistent with one of the possible heating pathways proposed by McCubbin et al. (2016).

5.4 Unraveling the pre-excavation petrogenetic histories and evolution of the breccias

Each sample contains a distinct population of lithic, mineral, impact-melt, and breccia clasts. These components have their own petrogenetic histories; for example, lithic clasts have their own igneous crystallization history starting from melt and undergoing fractional crystallization to produce the parent rock of the lithic clast. This section will not focus on the formation and evolution of individual clasts, but rather on the formation of each breccia. The petrogenetic history of each breccia is divided into 3-5 stages that includes destructive, constructive or lithification, post-lithification modifications and excavation.

5.4.1 NWA 14340

NWA 14340's post-lithification modification prior to excavation is not identifiable due to the shock overprint and not included here.

1. **Clast excavation and comminution (Destructive):** Lithic clasts and impact melt clasts have a subangular shape and range in size from 0.7 – 2.3 mm and 0.4 – 2.0 mm respectively. The studied clasts are classified as fine fine to coarse fine components of the breccia based on their size range (Fig. 5.4.1.1; Spray 2016). The fine size of the clasts is achieved by repeated impact events, recorded in clasts' individual shock histories, that led to comminution and the sub-angular shape of the clasts before they were deposited in the same vicinity near the surface of the Moon. Thus, before these

components could be ‘glued’ together to form this breccia, they were individually fragmented and reduced in size to fine and coarse fine grains, as a result of large and small meteoroid impact events (Kieffer 1975).

2. **Lithification (Constructive)**: Clasts in NWA 14340 were lithified likely due to compaction and sintering caused by an impact event that induced equilibrium shock pressures in the range of ~18 – 20 GPa and post-shock temperature in the range of ~50 °C – 150 °C (Stöffler et al. 2018). The breccia likely formed in one event as the shock signature of plagioclase throughout mineral and lithic clasts is constant.
3. **Excavation**: NWA 14340 likely resided near or below the lunar surface post-lithification, until a subsequent impact event generated sufficient energy to dislodge the breccia from the lunar surface and eject it into space. This is likely the event that melted the matrix and the fast cooling of which led to its quenching. In-situ melting is indicated by the same composition of glass as the mineral assemblage found in the matrix, and the absence of reaction interfaces between melt and clasts. During decompression, high-pressure minerals nucleated within glassy areas recording conditions of 4- 8 GPa, and post-shock temperature > 1000 °C. Tissintite likely crystallized first, as transformation from quartz to coesite at >2.5 GPa is a sluggish process (Miyahara et al. 2014). Garnet crystallized last in hotter zones within glass.

Process	Material	Size range (mm)	Size name[a]	Components
Mainly aggregation	Breccias; lithic clasts (>1 cm size)	>256	Boulders	Bonded polyphase—polylithic aggregates Monolithic fragments
		64–256	Cobbles	
		10–64	Pebbles	
Mainly disaggregation	Regolith (<1 cm size)	4–10		Lithic clasts
		2–4	Granules	Mineral clasts
		1–2	Coarse fines	Glass spherules and fragments
		1–0.001	Fine fines (soil)	Meteoritic components Agglutinates
		<0.001	Nanophase, molecular, atomic, subatomic	Fe^0 Solar wind–implanted H, C, N, He, and other noble gases Solar flare– and galactic cosmic ray–implanted subatomic particles

Figure 5.4.1.1: Size scheme for clasts in regolith breccia adopted from Spray (2016).

5.4.2 Sariçiçek

1. **Clasts excavation and comminution (Destruction)**: Lithic clasts range in size from 0.4 – 1.8 mm, breccia clasts 0.7 – 2.1 mm, impact melt clasts 0.2 – 0.8 mm, exogenous clasts 0.2 mm, and mineral clasts < 0.1 – 1.7 mm. All clasts range from fine fine to coarse fine component of the regolith (Fig. 5.4.1.1; Spray 2016), and have angular shapes. The size distribution and shapes of clasts highlight their repeated fragmentation and comminution via impact events. This process resulted in a heterogenous mixture of clasts of varying mineralogies and textures that span across eucritic and diogenitic lithologies. The breccia clasts in Sariçiçek represent two generations of first destructive processes that fragment components and then constructive that lead to lithification of the components.
2. **<u>Lithification of breccia (Constructive):</u>** Sariçiçek was lithified by shock compaction. This process involved fusing or bonding of mineral clasts through solid state bonds rather than melting or sintering. Clasts present in Sariçiçek were likely buried in a local regolith layer, where one or many meteorite impacts generated shock waves, compressing the

clasts and the surrounding material. Sariçiçek could have formed in one stage or multiple stages. It could have occurred in a single stage with one impact event inducing weak shock lithification or in multiple stages with repeated low-velocity impacts continuously compressing and welding the material. 4 Vesta, situated in the asteroid belt, experiences a higher meteorite impact flux compared to the Moon and Mars (Housen and Wilkening 1982). This, and the low shock signature of Sariçiçek suggests possible lithification in multiple stages from impact events that induced low shock pressures.

3. **Post-Lithification modification**: The submicron regolith material in the matrix was likely thermally sintered. There is no evidence of medium or high-temperature modification in Sariçiçek. Therefore, the breccia likely did not reside significantly close to an external source of heat.
4. **Excavation**: The final stage in the petrogenetic history of the Sariçiçek meteorite involved its excavation from the surface of 4 Vesta. The impact event that lofted this meteorite from 4 Vesta did not involve sufficient pressure or temperature to significantly modify the meteorite. Alternatively, the excavating impact event could have added to the shock compaction of the meteorite and decreased its overall porosity.

5.4.3 NWA 10922

Among the three breccias, NWA 10922 is the most studied sample in the literature. Its petrogenetic history is primarily derived from existing research, supplemented by observations made in this study.

1. **Clasts excavation and comminution (Destructive):** Clasts identified in NWA 10922 include lithic, mineral, impact melt, breccia, and impact melt spherules. Lithic clasts

range in size from 0.1 – 0.3 mm, mineral clasts 0.3 – 2.4 mm, impact melt clasts 0.5 – 4.5 mm, breccia clasts 1.3 – 3.0 mm, and melt spherules 0.2 – 1.7 mm. There are a wide range of clast sizes present in this sample that vary from fine fine, coarse fines, granules, and pebble components of the regolith (Fig. 5.4.1.1; Spray 2016). The shapes of clasts differ from angular to subangular, except some impact melt clasts that have irregular or amoeboid shapes. Excavation of clasts from their parent rock and reduction in size likely occurred because of repeated impact events. Breccia clasts and impact melt clasts are some of the biggest clasts in the sample, which could suggest that lithification of these clasts is relatively new, and they were comminuted to a lesser extent than other clasts.

2. **Clast deposition (Constructive):** Components of NWA 10922 were excavated and mixed in an impact event that had low shock effects on the clasts. McCubbin et al. (2016) proposed clast deposition through atmospheric rainout following pyroclastic eruption(s) and/or impact events, based on their observation of unsorted clast sizes, angular clast shapes, and the presence of accretionary lapilli as noted by MacArthur et al. (2019).
3. **Post-deposition thermal annealing:** The deposited material was compacted and buried in a hot ejecta blanket where it was thermally annealed. This created a recrystallized matrix with interconnected grains that binds the deposited clasts together in this breccia.
4. **Post annealing hydrothermal alteration:** Pyrite-pyroxene intergrowths and Ni-rich pyrite mineralization occurred throughout the breccia (Lorand et al. 2015). Evidence of this includes the occurrence of pyrite related to fractures, euhedral to subhedral pyrite grains in the clasts and the matrix, and the Ni-rich composition of the pyrite (Lorand et al. 2015).

5. **Excavation:** Another impact event that had low shock effects on the breccia (mechanical twins observed by Leroux et al. (2016)) most likely ejected this meteorite from the surface of Mars.

5.5 Comparisons between the formation processes for the breccias

5.5.1 Clast Excavation and regolith mixing

Lithic and mineral clast sizes are generally similar across NWA 14340, Sariçiçek, and NWA 10922, with NWA 10922 exhibiting larger melt and breccia clasts (up to ~4 mm). Observations from each breccia sample support the dominance of impact cratering and gardening processes in mixing regolith and comminution of regolith grain sizes on the Moon, 4 Vesta, and Mars. This is supported for the Moon by Li and Mustard (2005) and Costello et al. (2018), for 4 Vesta by Schröder et al. (2013) and Stephan et al. (2014), and for Mars Christensen and Moore (1992) and Hartmann and Neukum (2001). Additionally, since Mars has a thin atmosphere, and had an active hydrological system, various chemical and physical processes additional to impact events can lead to regolith comminution and mixing (Christensen and Moore 1992, Baker 2006, Chevrier and Mathé 2007, Palumbo and Head 2018).

In NWA 14340, igneous and mineral clast lithologies vary in Mg and Fe content, with anorthitic plagioclase being the most abundant mineral phase. This suggests NWA 14340 likely originated from a region experiencing more vertical mixing of regolith with deeper layers, rather than lateral mixing over large distances as ejecta deposits. Sariçiçek's lithic clasts are predominantly eucritic with few diogenite clasts. It has been suggested that 4 Vesta has a layered structure, where howardites represent the surficial material, eucrites represent the crust, and diogenites represent the lower crust (Mittlefehldt 2015). Sariçiçek's enrichment in eucritic clasts suggests its precursor regolith experienced more lateral mixing rather than vertical mixing with deeper regolith layers and/or bedrock. Lateral mixing on the Moon is limited compared to 4 Vesta due to their differing gravity, 1.62 m/s^2 and 0.22 m/s^2, respectively (Mittlefehldt et al. 2013). This difference requires more energy to transport ejecta particles laterally on the Moon than on 4 Vesta. Furthermore, the average impact velocity of meteorites hitting the Moon's surface is 22 km/s, (Ito and Malhotra 2010) compared to 4.6 km/s for 4 Vesta (Rivkin and Bottke 1996). Despite 4 Vesta's higher impact frequency on average, due to its location in the asteroid belt, the Moon receives less material but at higher velocities. This leads to deeper impacts and regolith gardening on the Moon, while 4 Vesta experiences more gardening of its upper surface layer due to lower impact velocities at higher frequencies. This confirms that physical processes prevail as a form of weathering as opposed to chemical processes, in the regolith mixing and comminution stage on the Moon and 4 Vesta.

5.5.2 Lithification

Meteorite impact processes also prevailed in the lithification stage of NWA 14340, Sariçiçek, and NWA 10922. The formation mechanisms of NWA 14340 are unclear, but it likely involved at least one impact event in its lithification history as there is a uniform shock signature across all plagioclase clasts. The clasts in NWA 14340 were likely gathered within a layer of regolith and were glued together because of either high pressure induced by an impact event or post-impact temperature, or a combination of both.

Sariçiçek and NWA 10922 experienced mild shock events in their histories, yet their matrix textures are very different. Sariçiçek was shock-lithified with minimal thermal effects, while NWA 10922 underwent thermal annealing that recrystallized the matrix. The lithification histories of both meteorites are shown below in distinct stages.

Sariçiçek:

1. Clasts reside in a regolith layer
2. Impact event(s) weld the clasts together and with the surrounding finer-grained material
3. The matrix is pushed into crevices and forced into spaces between larger clasts

NWA 10922:

1. Clasts reside in a regolith layer
2. An impact event ejects them and deposits them in a hot ejecta blanket
3. The matrix recrystallizes around the larger clasts

For shock-lithification to create Sariçiçek, clasts needed to be buried away from the impactor's point of contact. Direct contact could cause melting or vaporization, while clasts too close to the surface might be excavated as ejecta instead of lithified. Therefore, Sariçiçek was likely buried in a regolith layer not directly under the impact point. Additionally, Sariçiçek escaped significant thermal effects during and after lithification because it was not part of a hot ejecta blanket or near an impact melt sheet. In contrast, NWA 10922's matrix thermally annealed and recrystallized because it was closer to the impact crater and possible melt sheet, as a source of the necessary heat. Based on this, the key factor defining whether lithification occurred under temperature or pressure regimes for Sariçiçek and NWA 10922 was the region of lithification relative to the impact crater.

5.5.3 Post Lithification modification

This stage involves modifications to the breccia after lithification but before excavation. While any changes during excavation count as post-lithification modifications, this stage is treated separately for simplicity. NWA 14340 and Sariçiçek show no evidence of post-lithification modifications. Neither the Moon nor 4 Vesta had an active hydrosphere or atmosphere in its geologic history, preventing wind or water from modifying surficial rocks.

Although these breccias show no post-lithification thermal metamorphism, metasomatism, or hydrothermal activity, surficial modifications are documented in other lunar regolith breccias and howardites. Meteorites from both bodies show secondary veinlets of olivine and Fe-enrichments in pyroxene (Barrat et al. 2011, Patzer and McSween 2012, Zeng et al. 2020, Rombeck et al. 2021, Shisseh et al. 2023), though the veins' origins are debated between fluid-assisted metasomatism and heating. Sulfidization in high-Fe pigeonite has been recorded in eucrite and howardite clasts (Zhang et al. 2013); some clasts in Sariçiçek have undergone sulfidization before incorporation into the breccia. Zhang et al. (2013) suggest sulfidization results from reactions between $FeSiO_3$ in pyroxene and S-rich vapors formed by volatilization due to impact heating on 4 Vesta's surface.

In contrast, NWA 10922 from Mars shows post-lithification modifications, evidenced by pyrite crystallization in fractures and pore spaces (Lorand et al. 2015). This occurred at high temperatures (400-500 °C) due to repeated pulses of S-rich hydrothermal fluids, a logical inference given Mars' impact history and evidence of near-surface water (Baker 2006, Ehlmann et al. 2011). Additionally, NWA 7034 contains significant extraterrestrial water (up to 6000 ppm), and interaction of impact-heated material with near-surface H_2O could generate and sustain hydrothermal systems on Mars, as inferred by similar processes on Earth (Osinski et al. 2013)

5.5.4 Excavation

Meteorites are excavated from their planetary bodies by impact events (Rubin 2015). NWA 14340 experienced pressures high enough to melt the matrix throughout the sample, which then quenched to glass with widespread occurrences of tissintite. Low to medium pressure conditions faced by regolith breccias from the moon are provided by shock conditions documented in NWA 14340. In contrast, Sariçiçek and NWA 10922 were likely ejected from 4 Vesta and Mars, respectively, under low shock conditions. The low shock conditions were sufficient to allow the meteorites to escape the gravitational pull of these planetary bodies. Both breccias suggest that low shock pressures can facilitate excavation from planetary surfaces, establishing a lower limit for the shock conditions endured by regolith breccias during excavation from 4 Vesta and Mars.

Chapter 6: Conclusion

This study conducted a detailed examination of the petrogenetic histories and evolution of three meteoritic breccias—NWA 14340 from the Moon, Sariçiçek from 4 Vesta, and NWA 10922 from Mars—using a combination of FESEM, EDS, and Raman spectroscopy techniques. These methods proved highly effective, especially when employed complementarily, in good imaging, qualitative mineral compositions, and unequivocal identification of mineral species. Additionally, EPMA provided reliable quantitative chemical analyses. Moving forward, if petrological investigations advance, more sophisticated techniques should be employed to explore the nanoscale materials and chemical properties of these meteorites.

The findings of this study emphasise the pivotal role of impact events in both the fragmentation and lithification processes that shape planetary regolith breccias. Impact-induced comminution led to the formation of subangular clasts, representing a destructive phase preceding lithification. The subsequent lithification of these clasts occurred under varied conditions, ranging from shock-induced compaction to thermal sintering, reflecting the diverse geological environments of the Moon, 4 Vesta, and Mars. Furthermore, this study highlights the significance of shock effects as key tracers of geological histories of these breccias. High-pressure minerals, tissintite, coesite, and garnet in the glassy matrix of NWA 14340 elucidate the pressure and temperature conditions during the meteorite's excavation. In contrast, Sariçiçek and NWA 10922 exhibit lower shock effects, highlighting their distinct evolutionary histories shaped by varied impact intensities.

It is important to recognize that impact cratering encompass a myriad of processes, whose manifestations can vary depending on factors such as impactor velocity, impactor composition, target material composition, the target's surficial environment, and the most important factor outlined in this study, the location of lithification relevant to an impact crater. The observed variations in lithification mechanisms, post-depositional modifications, and shock effects among the breccias elucidate the dynamic interplay between impact events and planetary geology. By deciphering the intricate petrogenetic histories of the breccias, this study contributes to a deeper understanding of planetary processes and the broader context of planetary body evolution. Moreover, this study underscores the importance of impact events as both agents of disruption and agents of consolidation in shaping the surfaces of rocky planetary bodies.

References

Agee, C.B., Wilson, N.V., McCubbin, F.M., Ziegler, K., Polyak, V.J., Sharp, Z.D., Asmerom, Y., Nunn, M.H., Shaheen, R., Thiemens, M.H., Steele, A., Fogel, M.L., Bowden, R., Glamoclija, M., Zhang, Z., and Elardo, S.M. 2013. Unique Meteorite from Early Amazonian Mars: Water-Rich Basaltic Breccia Northwest Africa 7034. Science, **339**: 780–785.

Baker, V.R. 2006. Water and the evolutionary geological history of Mars. BOLLETTINO-SOCIETA GEOLOGICA ITALIANA, **125**: 357. ROMA SOCIETA GEOLOGICA ITALIANA.

Barrat, J.-A., Yamaguchi, A., Bunch, T., Bohn, M., Bollinger, C., and Ceuleneer, G. 2011. Possible fluid–rock interactions on differentiated asteroids recorded in eucritic meteorites. Geochimica et Cosmochimica Acta, **75**: 3839–3852. Elsevier.

Beck, A.W., and McSween Jr., H.Y. 2010. Diogenites as polymict breccias composed of orthopyroxenite and harzburgite. Meteoritics and Planetary Science, **45**: 850–872.

Beck, A.W., Mittlefehldt, D.W., McSWEEN Jr, H.Y., RUMBLE III, D., LEE, C.A., and Bodnar, R.J. 2011. MIL 03443, a dunite from asteroid 4 Vesta: Evidence for its classification and cumulate origin. Meteoritics & Planetary Science, **46**: 1133–1151. Wiley Online Library.

Beck, A.W., Welten, K.C., McSWEEN Jr, H.Y., Viviano, C.E., and Caffee, M.W. 2012. Petrologic and textural diversity among the PCA 02 howardite group, one of the largest pieces of the Vestan surface. Meteoritics & Planetary Science, **47**: 947–969. Wiley Online Library.

Binzel, R.P., Gaffey, M.J., Thomas, P.C., Zellner, B.H., Storrs, A.D., and Wells, E.N. 1997. Geological mapping of Vesta from 1994 Hubble Space Telescope images. Icarus, **128**: 95–103.

Bischoff, A. 1996. Lunar meteorite Queen Alexandra Range 93069: A lunar highland regolith breccia with very low abundances of mafic components. Meteoritics & Planetary Science, **31**: 849–855. Wiley Online Library.

Bischoff, A., Scott, E.R.D., Metzler, K., and Goodrich, C.A. 2006. Nature and Origins of Meteoritic Breccias. *In* Meteorites and the Early Solar System II. Available from https://www.higp.hawaii.edu/~escott/MESS%20II%20breccias%20.pdf.

Bischoff, A., Weber, D., Clayton, R., Faestermann, T., Franchi, I., Herpers, U., Knie, K., Korschinek, G., Kubik, P., and Mayeda, T. 1998. Petrology, chemistry, and isotopic compositions of the lunar highland regolith breccia Dar al Gani 262. Meteoritics & Planetary Science, **33**: 1243–1257. Wiley Online Library.

Bouvier, A., Gattacceca, J., Grossman, J., and Metzler, K. 2017. The meteoritical bulletin, No. 105. Meteoritics & Planetary Science, **52**: 2411. Wiley.

Bowman, L.E., Papike, J.J., and Spilde, M.N. 1999. Diogenites as asteroidal cumulates: Insights from spinel chemistry. American Mineralogist, **84**: 1020–1026. Mineralogical Society of America.

Bunch, T., Irving, A., Wittke, J., Kuehner, S., Rumble, D., and Sipiera, P. 2010. Northwest Africa 5784, northwest Africa 5968 and northwest Africa 6157: More vestan dunites and olivine diogenites. Meteoritics and Planetary Science Supplement, **73**: 5315.

Bunch, T., Wittke, J., Rumble III, D., Irving, A., and Reed, B. 2006. Northwest Africa 2968: A Dunite from 4Vesta. Meteoritics and Planetary Science Supplement, **41**: 5252.

Calzada-Diaz, A., Joy, K., Crawford, I., and Nordheim, T. 2015. Constraining the source regions of lunar meteorites using orbital geochemical data. Meteoritics & Planetary Science, **50**: 214–228. Wiley Online Library.

Calzada-Diaz, A., Joy, K., Crawford, I., and Strekopytov, S. 2017. The petrology, geochemistry, and age of lunar regolith breccias Miller Range 090036 and 090070: Insights into the crustal history of the Moon. Meteoritics & Planetary Science, **52**: 3–23. Wiley Online Library.

Cao, H., Ling, Z., Chen, J., Fu, X., and Zou, Y. 2021. Petrography, mineralogy, and geochemistry of a new lunar magnesian feldspathic meteorite Northwest Africa 11460. Meteoritics & Planetary Sciene, **58**: 1857–1889. doi:10.1111/maps.13741.

Cartwright, J.A., Ott, U., Herrmann, S., and Agee, C.B. 2014. Modern atmospheric signatures in 4.4 Ga Martian meteorite NWA 7034. Earth and Planetary Science Letters, **400**: 77–87.

Cartwright, J.A., Ott, U., Mittlefehldt, D.W., Herrin, J.S., Herrmann, S., Mertzman, S.A., Mertzman, K.R., Peng, Z.X., and Quinn, J.E. 2013. The quest for regolithic howardites. Part 1: Two trends uncovered using noble gases. Geochimica et Cosmochimica Acta, **105**: 395–421. doi:10.1016/j.gca.2012.11.047.

Cassata, W.S., Cohen, B.E., Mark, D.F., Trappitsch, R., Crow, C.A., Wimpenny, J., Lee, M.R., and Smith, C.L. 2018. Chronology of martian breccia NWA 7034 and the formation of the martian crustal dichotomy. Science Advances, **4**.

Chao, E., Boreman, J., and Desborough, G. 1971. Unshocked and shocked Apollo 11 and 12 microbreccias: characteristics and some geologic implications. pp. 797–816.

Chen, D.-L., Zhang, A.-C., Pang, R.-L., Chen, J.-N., and Li, Y. 2019. Shock-induced phase transformation of anorthitic plagioclase in the eucrite meteorite Northwest Africa 2650. Meteoritics & Planetary Science, **54**: 1548–1562. John Wiley & Sons, Ltd. doi:10.1111/maps.13286.

Chevrier, V., and Mathé, P.-E. 2007. Mineralogy and evolution of the surface of Mars: a review. Planetary and Space Science, **55**: 289–314. Elsevier.

Christensen, P., and Moore, H.J. 1992. The Martian surface layer. *In* Mars. University of Arizona Press, Space Science Series. pp. 686–729.

Cohen, B.A. 2013. The Vestan cataclysm: Impact-melt clasts in howardites and the bombardment history of 4 Vesta. Meteoritics & Planetary Science, **48**: 771–785.

Collerson, K.D., Williams, Q., Kamber, B.S., Omori, S., Arai, H., and Ohtani, E. 2010. Majoritic garnet: A new approach to pressure estimation of shock events in meteorites and the encapsulation of sub-lithospheric inclusions in diamond. Geochimica et Cosmochimica Acta, **74**: 5939–5957. Elsevier.

Costello, E.S., Ghent, R.R., and Lucey, P.G. 2018. The mixing of lunar regolith: Vital updates to a canonical model. Icarus, **314**: 327–344. Elsevier.

De Ronde, A., and Stünitz, H. 2007. Deformation-enhanced reaction in experimentally deformed plagioclase-olivine aggregates. Contributions to Mineralogy and Petrology, **153**: 699–717. Springer.

Delaney, J.S., Prinz, M., and Takeda, H. 1984. The polymict eucrites. Journal of Geophysical Research: Solid Earth, **89**: C251–C288. Wiley Online Library.

Delaney, J.S., Takeda, H., Prinz, M., Nehru, C.E., and Harlow, G.E. 1983. THE NOMENCLATURE OF POLYMICT BASALTIC ACHONDRITES. Meteoritics, **18**: 103–111. John Wiley & Sons, Ltd. doi:10.1111/j.1945-5100.1983.tb00581.x.

Demidova, S., Nazarov, M., Anand, M., and Taylor, L. 2003. Lunar regolith breccia Dhofar 287B: A record of lunar volcanism. Meteoritics & Planetary Science, **38**: 501–514. Wiley Online Library.

Du, T., Zhang, A., Chen, J., and Wen, Y. 2024. Discovery of Lunar Super-Silicic Garnet and Its Implication for Anomalous Temperature Distribution in Shock Melt Veins. LPI Contributions, **3040**: 1424.

Ehlmann, B.L., Mustard, J.F., Murchie, S.L., Bibring, J.-P., Meunier, A., Fraeman, A.A., and Langevin, Y. 2011. Subsurface water and clay mineral formation during the early history of Mars. Nature, **479**: 53–60. Nature Publishing Group UK London.

Fagan, A., and Gross, J. 2020. Preliminary melt models of troctolite and anorthosite clasts within northwest Africa 11303. p. 2904.

Fang, Z., and Wang, H. 2010. Sintering of ultrafine and nanosized particles. *In* Sintering of advanced materials. Elsevier. pp. 434–473.

Freeman, A., and Frazer, F. 1968. Pseudo polymorphic transition: the amphibole→ pyroxene reaction. Nature, **220**: 67–68. Nature Publishing Group UK London.

Fritz, J., Assis Fernandes, V., Greshake, A., Holzwarth, A., and Böttger, U. 2019. On the formation of diaplectic glass: Shock and thermal experiments with plagioclase of different chemical compositions. Meteoritics & Planetary Science, **54**: 1533–1547. Wiley Online Library.

Fruland, R.M. 1983. Regolith breccia workbook. National Aeronautics and Space Administration, **19045**.

Gattacceca, J., McCubbin, F.M., Grossman, J., Bouvier, A., Chabot, N.L., d'Orazio, M., Goodrich, C., Greshake, A., Gross, J., and Komatsu, M. 2022. The meteoritical bulletin, No. 110. Meteoritics & Planetary Science, **57**: 2102–2105. Wiley Online Library.

German, R. 2014. Sintering: from empirical observations to scientific principles. Butterworth-Heinemann.

Goodwin, A., Garwood, R.J., and Tartese, R. 2022. A Review of the "Black Beauty" Martian Regolith Breccia and Its Martian Habitability Record. Astrobiology, **22**.

Gregory, T., Joy, K.H., Strekopytov, S., and Curran, N.M. 2017. Geochemistry and petrology of howardite Miller Range 11100: A lithologically diverse piece of the Vestan regolith. Meteoritics & Planetary Science, **52**: 206–224. Wiley Online Library.

Gross, J., Treiman, A.H., and Mercer, C.N. 2014. Lunar feldspathic meteorites: Constraints on the geology of the lunar highlands, and the origin of the lunar crust. Earth and Planetary Science Letters, **388**: 318–328. doi:10.1016/j.epsl.2013.12.006.

Hartmann, W.K., and Neukum, G. 2001. Cratering chronology and the evolution of Mars. Springer. pp. 165–194.

Hewins, R.H., Zanda, B., Humayun, M., Nemchin, A., Lorand, J.-P., Pont, S., Deldicque, D., Bellucci, J.J., Beck, P., Leroux, H., Marinova, M., Remusat, L., Göpel, C., Lewin, E., Grange, M., Kennedy, A., and Whitehouse, M.J. 2017. Regolith breccia Northwest Africa 7533: Mineralogy and petrology with implications for early Mars. Meteoritics & Planetary Science, **52**: 89–124.

Hoffmann, H. 2011. Regolith (Planetary). Encyclopedia of Astrobiology. Springer, Berlin, Heidelberg,.

Hofmeister, A., Giesting, P., Wopenka, B., Gwanmesia, G., and Jolliff, B. 2004. Vibrational spectroscopy of pyrope-majorite garnets: Structural implications. American Mineralogist, **89**: 132–146. Mineralogical Society of America.

Housen, K.R., and Wilkening, L.L. 1982. Regoliths on small bodies in the solar system. Annual Review of Earth and Planetary Sciences, **10**: 355–376.

Hu, S., Lin, Y., Zhang, J., Hao, J., Xing, W., Zhang, T., Yang, W., and Changela, H. 2019. Ancient geologic events on Mars revealed by zircons and apatites from the Martian regolith breccia NWA 7034. Meteoritics and Planetary Science, **54**: 850–879. doi:https://doi-org.login.ezproxy.library.ualberta.ca/10.1111/maps.13256.

Humayun, M., Nemchin, A., Zanda, B., Hewins, R.H., Grange, M., and Kennedy, A. 2013. Origin and age of the earliest Martian crust from meteorite NWA 7533. Nature, **503**: 513–516.

Hutchison, R. 2004. Meteorites: A petrologic, chemical and isotopic synthesis. Cambridge University Press.

Ikeda, Y., and Takeda, H. 1984. Petrography and mineral compositions of the Yamato-7308 howardite. Memoirs of National Institute of Polar Research. Special issue, **35**: 149–183.

Ito, T., and Malhotra, R. 2010. Asymmetric impacts of near-Earth asteroids on the Moon. A&A 519, **519**: A63.

Janots, E., Gnos, E., Hofmann, B., Greenwood, R., Franchi, I., Bermingham, K., and Netwing, V. 2012. Jiddat al Harasis 556: A howardite impact melt breccia with an H chondrite component. Meteoritics & Planetary Science, **47**: 1558–1574. Wiley Online Library.

Jeanloz, R. 1980. Shock effects in olivine and implications for Hugoniot data. Journal of Geophysical Research: Solid Earth, **85**: 3163–3176. Wiley Online Library.

Jolliff, B.L., Korotev, R.L., and Rockow, K.M. 1998. Geochemistry and petrology of lunar meteorite Queen Alexandra Range 94281, a mixed mare and highland regolith breccia, with special emphasis on very-low-titanium mafic components. Meteoritics & Planetary Science, **33**: 581–601. Wiley Online Library.

Joy, K.H., and Arai, T. 2013. Lunar meteorites: new insights into the geological history of the Moon. Astronomy & Geophysics, **54**: 4.28-4.32. doi:10.1093/astrogeo/att121.

Joy, K.H., Crawford, I.A., Russell, S.S., and Kearsley, A.T. 2010. Lunar meteorite regolith breccias: An in situ study of impact melt composition using LA-ICP-MS with implications for the composition of the lunar crust. Meteoritics & Planetary Science, **45**: 917–946. Wiley Online Library.

Kerridge, J.F., and Matthews, M.S. 1988. Meteorite Regolith Breccias. *In* Meteorites and the early solar system. United States. pp. 144–164.

Kieffer, S.W. 1975. From regolith to rock by shock. The Moon, **13**: 301–320.

Koeberl, C., Kurat, G., and Brandstätter, F. 1991. MAC88105—A regolith breccia from the lunar highlands: Mineralogical, petrological, and geochemical studies. The Macalpine Hills Lunar Meteorite Consortium, **55**: 3073–3087. doi:10.1016/0016-7037(91)90474-J.

Korotev, R.L. 2022. Lunar meteorite: Northwest Africa 8046 clan. Washington University St. Louis. Available from https://sites.wustl.edu/meteoritesite/items/lm_nwa_08046_clan/.

Korotev, R.L., Jolliff, B.L., Zeigler, R.A., Gillis, J.J., and Haskin, L.A. 2003. Feldspathic lunar meteorites and their implications for compositional remote sensing of the lunar surface and the composition of the lunar crust. Geochimica et Cosmochimica Acta, **67**: 4895–4923. Elsevier.

Korotev, R.L., Zeigler, R.A., Jolliff, B.L., Irvin, A.J., and Bunch, T.E. 2009. Compositional and lithological diversity among brecciated lunar meteorites of intermediate iron concentration. Meteoritics & Planetary Science, **44**: 1287–1322. Wiley Online Library.

Kridelbaugh, S., McKay, G., and Weill, D. 1973. Breccias from the Lunar Highlands: Preliminary Petrographic Report on Apollo 16 Samples 60017 and 63335. Science, **179**: 71–74. American Association for the Advancement of Science.

Kushiro, I., and Yoder Jr, H. 1966. Anorthite—forsterite and anorthite—enstatite reactions and their bearing on the basalt—eclogite transformation. Journal of Petrology, **7**: 337–362. Oxford University Press.

Langevin, Y., and Arnold, J.R. 1977. The evolution of the lunar regolith. Annual Review of Earth and Planetary Sciences, **5**: 449–489.

Le Maitre, R.W., Streckeisen, A., Zanettin, B., Le Bas, M., Bonin, B., and Bateman, P. 2005. Igneous rocks: a classification and glossary of terms: recommendations of the International Union of Geological Sciences Subcommission on the Systematics of Igneous Rocks. Cambridge University Press.

Leroux, H., Jacob, D., Marinova, M., Hewins, R.H., Zanda, B., Pont, S., Lorand, J.-P., and Humayun, M. 2016. Exsolution and shock microstrucures of igneous pyroxeene clasts in he Northwest Africa 7533 Martian meteorite. Meteoritics & Planetary Science, **51**: 932–945.

Li, L., and Mustard, J.F. 2005. On lateral mixing efficiency of lunar regolith. Journal of Geophysical Research: Planets, **110**. Wiley Online Library.

Lindsay, F.N., Delaney, J.S., Turrin, B.D., Herzog, G.F., Park, J., and Swisher, C.C. 2016. Ar Ages of Martian Meteorite NWA 7034. 47th Annual Lunar and Planetary Science Conference. p. 3013.

Liu, X., Ohfuji, H., Nishiyama, N., He, Q., Sanehira, T., and Irifune, T. 2012. High-Pbehavior of anorthite composition and some phase relations of the CaO-Al2O3-SiO2 system to the lower mantle of the Earth, and their geophysical implications. Journal of Geophysical Research: Solid Earth, **117**. Wiley Online Library.

Liu, Y., Fischer, W.W., Ma, C., Beckett, J.R., Tschauner, O., Guan, Y., Lingappa, U.F., Webb, S.M., Prakapenka, V.B., Lanza, N.L., and Agee, C.B. 2021. Manganese oxides in Martian meteorites Northwest Africa (NWA) 7034 and 7533. Icarus, **364**: 114471. doi:10.1016/j.icarus.2021.114471.

Liu, Y., Ma, C., Beckett, J.R., Chen, Y., and Guan, Y. 2016. Rare-earth-element minerals in martian breccia meteorites NWA 7034 and 7533: Implications for fluid–rock interaction in the martian crust. Earth and Planetary Science Letters, **451**: 251–262. doi:https://doi.org/10.1016/j.epsl.2016.06.041.

Lorand, J.-P., Hewins, R.H., Remusat, L., Zanda, B., Pont, S., Leroux, H., Marinova, M., Jacob, D., Humayun, M., Nemchin, A., Grange, M., Kennedy, A., and Göpel, C. 2015. Nickeliferous pyrite tracks pervasive hydrothermal alteration in Martian regolith breccia: A study in NWA 7533. Meteoritics & Planetary Science, **50**: 2099–2120.

Lorenz, K.A., Nazarov, M.A., Kurat, G., Brandstaetter, F., and Ntaflos, Th. 2007. Foreign meteoritic material of howardites and polymict eucrites. Petrology, **15**: 109–125. doi:10.1134/S0869591107020014.

Lunning, N., and Gross, J. 2019. Lunar feldspathic regolith breccia with magnesium-rich components: Northwest Africa 11303. p. 2407.

Lunning, N.G., Welten, K.C., McSween Jr, H.Y., Caffee, M.W., and Beck, A.W. 2016. Grosvenor Mountains 95 howardite pairing group: Insights into the surface regolith of asteroid 4 Vesta. Meteoritics & Planetary Science, **51**: 167–194. Wiley Online Library.

Ma, C., Tschauner, O., Beckett, J.R., Liu, Y., Rossman, G.R., Zhuravlev, K., Prakapenka, V., Dera, P., and Taylor, L.A. 2015. Tissintite, (Ca, Na, □)AlSi2O6, a highly-defective, shock-induced, high-pressure clinopyroxene in the Tissint martian meteorite. Earth and Planetary Science Letters, **422**: 194–205. doi:10.1016/j.epsl.2015.03.057.
MacArthur, J.L., Bridges, J.C., Hicks, L.J., Burgess, R., Joy, K.H., Branney, M.J., Hansford, G.M., Baker, S.H., Schwenzer, S.P., Gurman, S.J., Stephen, N.R., Steer, E.D., Piercy, J.D., and Ireland, T.R. 2019. Mineralogical constraints on the thermal history of martian regolith breccia Northwest Africa 8114. Geochimica et Cosmochimica Acta, **246**: 267–298.
Mansfeld, U., Langenhorst, F., Ebert, M., Kowitz, A., and Schmitt, R.T. 2017. Microscopic evidence of stishovite generated in low-pressure shock experiments on porous sandstone: Constraints on its genesis. Meteoritics & Planetary Science, **52**: 1449–1464. Wiley Online Library.
Mayne, R., McSween Jr, H.Y., McCoy, T.J., and Gale, A. 2009. Petrology of the unbrecciated eucrites. Geochimica et Cosmochimica Acta, **73**: 794–819. Elsevier.
Mccord, T.B., Adams, J.B., and Johnson, T.V. 1970. Asteroid Vesta: Spectral Reflectivity and Compositional Implications. Science, **168**: 1445–1447.
McCubbin, F.M., Boyce, J.W., Novák-Szabó, T., Santos, A.R., Tartèse, R., Muttik, N., Domokos, G., Vazquez, J., Keller, L.P., Moser, D.E., Jerolmack, D.J., Shearer, C.K., Steele, A., Elardo, S.M., Rahman, Z., Anand, M., Delhaye, T., and Agee, C.B. 2016. Geologic history of Martian regolith breccia Northwest Africa 7034: Evidence for hydrothermal activity and lithologic diversity in the Martian crust. Journal of Geophysical Research - Planets, **121**: 2120–2149.
McKay, D.S., Heiken, G., Basu, A., Blanford, G., Simon, S., Reedy, R., French, B.M., and Papike, J. 1991. The lunar regolith. Lunar sourcebook, **567**: 286–356.
Mckay, D.S., and Morrison, D.A. 1971. Lunar breccias. Journal of Geophysical Research, **76**: 5658–5669. Wiley Online Library.
Mercer, C.N., Treiman, A.H., and Joy, K.H. 2013. New lunar meteorite Northwest Africa 2996: A window into farside lithologies and petrogenesis. Meteoritics & Planetary Science, **48**: 289–315. Wiley Online Library.
Miller, C. 1974. Reaction rims between olivine and plagioclase in metaperidotites, Ötztal Alps, Austria. Contributions to mineralogy and petrology, **43**: 333–342. Springer.
Mingsheng, P., Mao, H., Dien, L., and Chao, E. 1994. Raman spectroscopy of garnet-group minerals. Chinese Journal of Geochemistry, **13**: 176–183. Springer.
Mittlefehldt, D.W. 1994. The genesis of diogenites and HED parent body petrogenesis. Geochimica et Cosmochimica Acta, **58**: 1537–1552. doi:10.1016/0016-7037(94)90555-X.
Mittlefehldt, D.W. 2008. Meteorite dunite breccia MIL 03443: A probable crustal cumulate closely related to diogenites from the HED parent asteroid.
Mittlefehldt, D.W. 2015. Asteroid (4) Vesta: I. The howardite-eucrite-diogenite (HED) clan of meteorites. Geochemistry, **75**: 155–183.
Mittlefehldt, D.W., Herrin, J.S., Quinn, J.E., Mertzman, S.A., Cartwright, J.A., Mertzman, K.R., and Peng, Z.X. 2013. Composition and petrology of HED polymict breccias: The regolith of (4) Vesta. Meteoritics & Planetary Science, **48**: 2105–2134.

Miyahara, M., Ohtani, E., Yamaguchi, A., Ozawa, S., Sakai, T., and Hirao, N. 2014. Discovery of coesite and stishovite in eucrite. Proceedings of the National Academy of Sciences, **111**: 10939–10942. National Acad Sciences.

Nagaoka, H., Karouji, Y., Arai, T., Ebihara, M., and Hasebe, N. 2013. Geochemistry and mineralogy of a feldspathic lunar meteorite (regolith breccia), Northwest Africa 2200. Polar science, **7**: 241–259. Elsevier.

Nyquist, L.E., Shih, C.-Y., McCubbin, F.M., Santos, A.R., Shearer, C.K., Peng, Z.X., Burger, P.V., and Agee, C.B. 2016. Rb-Sr and Sm-Nd isotopic and REE studies of igneous components in the bulk matrix domain of Martian breccia Northwest Africa 7034. Meteoritics & Planetary Science, **51**: 483–498.

Osinski, G.R., Grieve, R.A., Bleacher, J.E., Neish, C.D., Pilles, E.A., and Tornabene, L.L. 2018. Igneous rocks formed by hypervelocity impact. Journal of Volcanology and Geothermal Research, **353**: 25–54. Elsevier.

Osinski, G.R., Tornabene, L.L., Banerjee, N.R., Cockell, C.S., Flemming, R., Izawa, M.R., McCutcheon, J., Parnell, J., Preston, L.J., and Pickersgill, A.E. 2013. Impact-generated hydrothermal systems on Earth and Mars. Icarus, **224**: 347–363. Elsevier.

Ostertag, R., and Stöffler, D. 1982. Thermal annealing of experimentally shocked feldspar crystals. Journal of Geophysical Research: Solid Earth, **87**: A457–A463. Wiley Online Library.

Palumbo, A.M., and Head, J.W. 2018. Impact cratering as a cause of climate change, surface alteration, and resurfacing during the early history of Mars. Meteoritics & Planetary Science, **53**: 687–725. Wiley Online Library.

Pang, R.L., Zhang, A.C., Wang, S.Z., Wang, R.C., and Yurimoto, H. 2016. High-pressure minerals in eucrite suggest a small source crater on Vesta. Scientific Reports, **6**: 26063. doi:https://doi-org.login.ezproxy.library.ualberta.ca/10.1038/srep26063.

Patzer, A., and McSween, H.Y. 2012. Ordinary (mesostasis) and not-so-ordinary (symplectites) late-stage assemblages in howardites. Meteoritics & Planetary Science, **47**: 1475–1490. John Wiley & Sons, Ltd. doi:10.1111/j.1945-5100.2012.01408.x.

Patzer, A., and McSween Jr, H.Y. 2018. Ferroan olivine-bearing eucrite clasts found in howardites. Meteoritics & Planetary Science, **53**: 1131–1149. Wiley Online Library.

Pickersgill, A.E., Jaret, S.J., Pittarello, L., Fritz, J., and Harris, R.S. 2021. Shock effects in feldspars: An overview.

Pun, A., Keil, K., TAYLOR, G.J., and Wieler, R. 1998. The Kapoeta howardite: Implications for the regolith evolution of the howardite-eucrite-diogenite parent body. Meteoritics & Planetary Science, **33**: 835–851. Wiley Online Library.

Rivkin, A.S., and Bottke, W.F. 1996. Hypervelocity Impacts in the Asteroid Belt.

Roermund, V., Drury, Barnhoorn, and Ronde, D. 2000. Super-silicic garnet microstructures from an orogenic garnet peridotite, evidence for an ultra-deep (> 6 GPa) origin. Journal of metamorphic Geology, **18**: 135–147. Wiley Online Library.

Rombeck, S., Vollmer, C., Roszjar, J., Sarafian, A.R., and Klemme, S. 2021. How do secondary iron enrichments form within basaltic eucrites? An experimental approach. Meteoritics & Planetary Science, **56**: 911–928. Wiley Online Library.

Rosenberg, C.L., and Stünitz, H. 2003. Deformation and recrystallization of plagioclase along a temperature gradient: an example from the Bergell tonalite. Journal of Structural Geology, **25**: 389–408. Elsevier.

Rubin, A.E. 2015. Maskelynite in asteroidal, lunar and planetary basaltic meteorites: An indicator of shock pressure during impact ejection from their parent bodies. Icarus, **257**: 221–229. Elsevier.

Rucks, M.J., Whitaker, M.L., Glotch, T.D., Parise, J.B., Jaret, S.J., Catalano, T., and Dyar, M.D. 2018. Making tissintite: Mimicking meteorites in the multi-anvil. American Mineralogist, **103**: 1516–1519. Mineralogical Society of America.

Ryder, G. 1980. Catalog of Apollo 16 Rocks: 67015-69965. Lyndon B. Johnson Space Center.

Santos, A. R., Lewis, J.A., Agee, C.B., Humayin, M., McCubbin, F.M., and Shearer, C.K. 2017. Feldspar Variability in Northwest Africa 7034. Lunar and Planetary Science Conference.

Santos, A.R., Agee, C.B., McCubbin, F.M., Shearer, C.K., Burger, P.V., Tartèse, R., and Anand, M. 2015. Petrology of igneous clasts in Northwest Africa 7034: Implications for the petrologic diversity of the martian crust. Geochimica et Cosmochimica Acta, **157**: 56–85.

Schaal, R.B., and Horz, F. 1980. Experimental shock metamorphism of lunar soil. pp. 1679–1695.

Schneider, C.A., Rasband, W.S., and Eliceiri, K.W. 2012. NIH Image to ImageJ: 25 years of image analysis. Nature methods, **9**: 671–675. Nature Publishing Group.

Schröder, S., Mottola, S., Keller, H., Raymond, C., and Russell, C. 2013. Resolved photometry of Vesta reveals physical properties of crater regolith. Planetary and Space Science, **85**: 198–213. Elsevier.

Shang, S., Hui, H., Yang, Y., and Chen, T. 2022. Martian hydrothermal fluids recorded in the Sm-Nd isotopic systematics of apatite in regolith breccia meteorites. Earth and Planetary Science Letters, **581**.

Sharp, T.G., and DeCarli, P.S. 2006. Shock effects in meteorites. Meteorites and the early solar system II, **943**: 653–677. University of Arizona Press Tucson.

Sheikh, D., Ruzicka, A., Hutson, M., and Stream, M. 2022. Dunite Clast in Lunar Meteorite Northwest Africa (NWA) 14900: Mantle Derived? LPI Contributions, **2695**: 6077.

Shisseh, T., Chennaoui Aoudjehane, H., Barrat, J.A., Zanda, B., Hewins, R.H., Agee, C.B., Folco, L., Jacquet, E., and Pont, S. 2023. Fluid-assisted metasomatic processes on planetary bodies: Evidence from vestan lithologies. Geochimica et Cosmochimica Acta, **340**: 51–64. doi:10.1016/j.gca.2022.11.007.

Short, N.M. 1970. Evidence and implications of shock metamorphism in lunar samples. Science, **167**: 673–675. American Association for the Advancement of Science.

Simon, S., Papike, J., Gosselin, D., and Laul, J. 1985. Petrology and chemistry of Apollo 12 regolith breccias. Journal of Geophysical Research: Solid Earth, **90**: 75–86. Wiley Online Library.

Simon, S., Papike, J., Gosselin, D., and Laul, J. 1986. Petrology, chemistry and origin of Apollo 15 regolith breccias. Geochimica et Cosmochimica Acta, **50**: 2675–2691. Elsevier.

Simon, S., Papike, J., Shearer, C., and Laul, J. 1983. Petrology of the Apollo 11 highland component. Journal of Geophysical Research: Solid Earth, **88**: B103–B138. Wiley Online Library.

Sisodia, M., Shukla, A., Suthar, K., Mahajan, R., Murty, S., Shukla, P., Bhandari, N., and Natarajan, R. 2001. The Lohawat howardite: Mineralogy, chemistry and cosmogenic effects. Meteoritics & Planetary Science, **36**: 1457–1466. Wiley Online Library.

Snape, J.F., Joy, K.H., and Crawford, I.A. 2011. Characterization of multiple lithologies within the lunar feldspathic regolith breccia meteorite Northeast Africa 001. Meteoritics & Planetary Science, **46**: 1288–1312. Wiley Online Library.

Spray, J., Hudgins, J., and Walton, E.L. 2007. Mineralogy, petrology, and shock history of lunar meteorite Sayh al Uhaymir 300: A crystalline impact-melt breccia.
Spray, J.G. 2016. Lithification mechanisms for planetary regoliths: The glue that binds. Annual Review of Earth and Planetary Sciences, **44**: 139–174.
Spudis, P.D. 1984. Apollo 16 site geology and impact melts: Implications for the geologic history of the lunar highlands. Journal of Geophysical Research: Solid Earth, **89**: C95–C107. Wiley Online Library.
Stephan, K., Jaumann, R., De Sanctis, M., Tosi, F., Ammannito, E., Krohn, K., Zambon, F., Marchi, S., Ruesch, O., and Matz, K. 2014. Small fresh impact craters on asteroid 4 Vesta: A compositional and geological fingerprint. Journal of Geophysical Research: Planets, **119**: 771–797. Wiley Online Library.
Stöffler, D., Hamann, C., and Metzler, K. 2018. Shock metamorphism of planetary silicate rocks and sediments: Proposal for an updated classification system. Meteoritics & Planetary Science, **53**: 5–49. Wiley Online Library.
Tartèse, R., Anand, M., McCubbin, F.M., Santos, A.R., and Delhaye, T. 2014. Zircons in Northwest Africa 7034: Recorders of Crustal Evolution on Mars. Science. pp. 212–215.
Treiman, A.H., and Semprich, J. 2023. A dunite fragment in meteorite Northwest Africa (NWA) 11421: A piece of the Moon's mantle. American Mineralogist, **108**: 2182–2192. Mineralogical Society of America.
Unsalan, O., Jenniskens, P., Yin, Q.-Z., Kaygisiz, E., Albers, J., Clark, D.L., Granvik, M., Demirkol, I., Erdogan, I.Y., and Bengu, A.S. 2019. The Sariçiçek howardite fall in Turkey: Source crater of HED meteorites on Vesta and impact risk of Vestoids. Meteoritics & Planetary Science, **54**: 953–1008.
Walton, E.L., Sharp, T.G., Hu, J., and Filiberto, J. 2014. Heterogeneous mineral assemblages in Martian meteorite Tissint as a result of a recent small impact event on Mars. Geochimica et Cosmochimica Acta, **140**: 334–348. Elsevier.
Wang, A., Jolliff, B.L., Haskin, L.A., Kuebler, K.E., and Viskupic, K.M. 2001. Characterization and comparison of structural and compositional features of planetary quadrilateral pyroxenes by Raman spectroscopy. American Mineralogist, **86**: 790–806. doi:10.2138/am-2001-0703.
Warren, P.H., Kallemeyn, G.W., Huber, H., Ulff-Møller, F., and Choe, W. 2009. Siderophile and other geochemical constraints on mixing relationships among HED-meteoritic breccias. Geochimica et Cosmochimica Acta, **73**: 5918–5943. doi:10.1016/j.gca.2009.06.030.
Wittmann, A., Korotev, R.L., Jolliff, B.L., Irving, A.J., Moser, D.E., Barker, I., and Rumble III, D. 2015. Petrography and composition of Martian regolith breccia meteorite Northwest Africa 7475. Meteoritics & Planetary Sciene, **50**: 326–352.
Xia, Z., Miao, B., Zhang, C., Chen, H., Xie, L., Ranjith, P., Zhang, Y., and Si, B. 2021. Petrography and Shock Metamorphism of the Lunar Breccia Meteorite NWA 13120. Minerals, **11**: 899. MDPI.
Zeng, X., Li, S., Joy, K.H., Li, X., Liu, J., Li, Y., Li, R., and Wang, S. 2020. Occurrence and implications of secondary olivine veinlets in lunar highland breccia Northwest Africa 11273. Meteoritics & Planetary Science, **55**: 36–55. John Wiley & Sons, Ltd. doi:10.1111/maps.13421.
Zhang, A., Jiang, Q., Tomioka, N., Guo, Y., Chen, J., Li, Y., Sakamoto, N., and Yurimoto, H. 2021. Widespread Tissintite in Strongly Shock-Lithified Lunar Regolith Breccias. Geophysical research letters, **48**: e2020GL091554. Wiley Online Library.

Zhang, A.-C., Wang, R.-C., Hsu, W.-B., and Bartoschewitz, R. 2013. Record of S-rich vapors on asteroid 4 Vesta: Sulfurization in the Northwest Africa 2339 eucrite. Geochimica et Cosmochimica Acta, **109**: 1–13. doi:10.1016/j.gca.2013.01.036.

Zolensky, M.E., Weisberg, M.K., Buchanan, P.C., and Mittlefehldt, D.W. 1996. Mineralogy of carbonaceous chondrite clasts in HED achondrites and the Moon. Meteoritics & Planetary Science, **31**: 518–537. Wiley Online Library.